TECHNISCHE UNIVERSITÄT MÜNCHEN

Lehrstuhl für Technische Chemie II

Transport in nano-sized, mesoscopically structured ZSM-5 zeolites

Robin Kolvenbach

Vollständiger Abdruck der von der Fakultät für Chemie der Technischen Universität München zur Erlangung des akademischen Grades eines

Doktors der Naturwissenschaften (Dr. rer. nat.)

genehmigten Dissertation.

<table>
<tr><td>Vorsitzender:</td><td colspan="2">Univ. Prof. Dr. K.-O. Hinrichsen</td></tr>
<tr><td>Prüfer der Dissertation:</td><td></td><td></td></tr>
<tr><td></td><td>1.</td><td>Univ. Prof. Dr. J.A. Lercher</td></tr>
<tr><td></td><td>2.</td><td>Univ. Prof. Dr. K. Köhler</td></tr>
<tr><td></td><td>3.</td><td>Univ. Prof. Dr. R. Gläser, Universität Leipzig
(schriftliche Beurteilung)</td></tr>
<tr><td></td><td></td><td>Univ. Prof. Dr. U.K. Heiz (mündliche Prüfung)</td></tr>
</table>

Die Dissertation wurde am 14.02.2014 bei der Technischen Universität München eingereicht und durch die Fakultät für Chemie am 02.06.2014 angenommen.

Für Marianne, Dieter
und Stephanie

Acknowledgements

The success of this thesis is closely related to the help of many people to whom I want to express my deepest gratitude:

First of all I would like to thank Prof. Dr. Johannes A. Lercher for giving me the opportunity to work on this stimulating topic, excellent scientific discussions and the guidance throughout the thesis.

I am also grateful to Prof. Dr. Andreas Jentys for the excellent collaboration during the last 7 years. His support, guidance and trust throughout my study and Ph.D. thesis as well as numerous stimulating discussions are gratefully acknowledged.

I have to thank Prof. Dr. Sulaiman Al-Khattaf for the good cooperation throughout the project and his exceptionally new ideas.

Dr. Jaana Kanervo is gratefully acknowledged for excellent discussions, hours of programming and her highly motivating spirit to discover unchartered waters.

I would also like to thank my colleague Dr. John Ahn for the close and fruitful teamwork as well as the most convenient working atmosphere during the time of the thesis.

I thank Dr. Luis Francisco Gonzalez Pẽna for his enormous help in solving problems in the lap, productive cooperation and all the sweets.

I am also grateful to Dr. Oliver Gobin and Dr. Stefan Reitmeier for paving the way of my thesis with their outstanding work, sharing their knowledge and for enlightening scientific discussions in the beginning of my thesis. I am especially grateful to Dr. Gobin for teaching me basic numerics and programming.

I have to thank the team at the Max-Planck Institut für Kohlenforschung, namely Carolina Neudeck and Dr. Wolfgang Schmidt for elucidating discussions and exceptional new ideas. Moreover I am grateful to Axel Dreier for providing TEM images of outstanding quality.

The international research group "Diffusion in zeolites" under the supervision of Prof. Dr. Jörg Kärger is gratefully acknowledged for providing a forum of open discussions with the most distinguished experts in the field.

I am grateful to my colleagues Dr. Stefanie Simson, Jennifer Hein, Monica Pop and Stefan Schallmoser for their help in overcoming both scientific and non-scientific

challenges as well as for the most productive and convenient atmosphere in the bureau shared.

Xaver Hecht, Martin Neukamm and Andreas Marx are gratefully acknowledged for their crucial help with technical issues, which I faced day to day.

I am utmost grateful to the whole group of Prof. Lercher for the most supportive environment and the fruitful discussions. Moreover, I thank the students I have supervised during the last three years.

My brothers and sisters, Michaela Gerhards, Frank Gerhards, Roger Gerhards and Benjamin Köpke are gratefully acknowledged for their invaluable support.

I am deeply grateful to my parents Marianne Kolvenbach and Franz Dieter Gerhards for supporting me in any kind, not only during the past three years but my whole live.

Finally, I want to thank Stephanie Zeller for helping and supporting me to meet all challenges that I had to face during the thesis. I am especially grateful to her for always having an open ear and finding appropriate solutions. She is definitely the fundament for the success of my thesis.

Symbols

Latin symbols

A	amplitude in FR experiment	[-]
A_B	amplitude in a blank experiment	[-]
A_c	concentration amplitude	[-]
A_s	surface area	[m^2]
b_x	pre-exponential factor	[1/s]
B	amount of sorbate present in the sorbent	[mol]
$[B]$	matrix of inverted Maxwell-Stefan diffusivity	[s/m^2]
B_e	mean amount of sorbate present in the sorbent	[mol]
c	concentration	[mol/m^3]
c_i	concentration of component i	[mol/m^3]
c_0	initial concentration	[mol/m^3]
Δc	concentration change upon pressure jump	[mol/m^3]
c_e	mean concentration	[mol/m^3]
Δc_{eq}	concentration change at re-established equilibrium	[mol/m^3]
Δc_{ext}	concentration change at the external surface upon pressure jump	[mol/m^3]
$\Delta c_{ext,eq}$	concentration change at the external surface upon pressure jump after establishing an equilibrium	[mol/m^3]
Δc_{int}	concentration change at the internal sorption sites upon pressure jump	[mol/m^3]
$\Delta c_{int,eq}$	concentration change at the internal sorption sites upon pressure jump after establishing an equilibrium	[mol/m^3]
c_{BET}	constant related to the difference of the heat of adsorption and the evaporation enthalpy	[-]
c_{feed}	sorbate concentration in the feed	[mol/m^3]
$c_{permaeate}$	sorbate concentration in the permeate	[mol/m^3]
c_t	total concentration	[mol/m^3]
c_x	concentration of molecules in state x	[mol/m^3]
D	Fick diffusion coefficient	[m^2/s]

$\mathbb{D}$	Maxwell-Stefan diffusion coefficient	[m²/s]
$[D]$	matrix of Fick diffusivities	[m²/s]
D_0	pre-exponential factor	[m²/s]
$D_{0,app}$	pre-exponential factor	[m²/s]
D_{app}	apparent Fick diffusion coefficient	[m²/s]
D_e	effective Fick diffusion coefficient	[m²/s]
D_H	diffusion coefficient according to the hopping mechanism	[m²/s]
D_K	Knudsen diffusion coefficient	[m²/s]
D_i	Fick diffusion coefficient of species i	[m²/s]
$\widehat{D}_i$	Eigenvalue i of the matrix of Fick diffusivities	[m²/s]
$\mathbb{D}_{iV}$	single component Maxwell-Stefan diffusion coefficient of component i	[m²/s]
$\mathbb{D}_{ij}$	counter-sorption Maxwell Stefan diffusion coefficient	[m²/s]
$\mathcal{D}_{ij}$	elements of matrix $[B]^{-1}$	[m²/s]
$D_{K,eff}$	effective Knudsen diffusion coefficient	[m²/s]
d_p	pore diameter	[m]
$E_{A,ads}$	activation energy of adsorption	[J/mol]
$E_{A,des}$	activation energy of desorption	[J/mol]
$E_{A,D,app}$	activation energy of the apparent diffusion coefficient	[J/mol]
$F(x)$	diffusive flux	[mol/(m² s)]
F_i	diffusive flux of species i	[mol/(m² s)]
$\Delta G_{ads}{}^0$	free Gibbs energy of adsorption at standard conditions	[J/mol]
$\Delta H_{ads}{}^0$	heat of adsorption at standard conditions	[J/mol]
$[I]$	identity matrix	[-]
ΔI_x	intensity change of band x upon pressure jump	[-]
k_{ads}	rate constant of adsorption	[1/s]
k_B	Boltzmann constant	[J/K]
k_{pe}	rate constant of pore entrance	[1/s]
$k_{Std.}$	adsorbed amount of a nitrogen monolayer on the reference (at p/p₀=0.4) divided by its surface area	[cm]
K	adsorption equilibrium constant	[-]
K_{FR}	constant defined by Eq. 2.4.7	[-]

K_L	Langmuir constant	[1/Pa]
l	diffusional path length	[m]
$\bar{l}$	mean diffusional path length	[m]
M	molar mass	[mol/kg]
$m(t)$	total sorbate amount on sample	[mol/kg]
m_∞	total sorbate amount on sample at the end of the experiment	[mol/kg]
$m_{cat,tot}$	overall sample mass	[kg]
m_{wafer}	mass of an IR wafer	[kg]
$\dot{n}$	molecular flux	[mol/s]
n_i^s	surface concentration of species i	[mol/m^2]
N_i	molar flux of species i	[mol/(m^2 s)]
n_t^s	total surface concentration	[mol/m^2]
P	pressure amplitude	[-]
p_0	standard pressure (10^5 Pa)	[Pa]
p_e	mean partial pressure	[Pa]
p_i	partial pressure of component i	[Pa]
p_x	pressure of component x	[Pa]
Q	volumetric flow rate	[m^3/s]
r	radial coordinate	[m]
r_{ini}	initial rate	[mol/(m^3 s)]
r_w	radius of an IR wafer	[m]
r_x	formation rate of component x	[mol/(m^3 s)]
R	gas constant	[J/(mol K)]
R_m	average particle radius of fraction m	[m]
R_p	particle radius	[m]
$\Delta S_{ads}{}^0$	entropy of adsorption at standard conditions	[J/(mol K)]
S_{ext}	external surface area	[cm^2/g]
SF	separation factor	[-]
S_{meso}	mesoporous surface area	[cm^2/g]
t	time	[s]
t_p	time span of a fast time resolved infrared spectroscopy experiment (60 s)	[s]
T	temperature	[K]

T_0	experimental temperature	[K]
TF	thermodynamic force	[-]
u	average speed of molecular movement	[m/s]
$v(p)$	adsorbed volume	[cm^3 STP/g]
V	volume	[m^3]
V_{ad}	overall adsorbed volume	[m^3]
V_{FR}	volume of the FR system	[m^3]
$V_{FR,eq}$	mean volume of the FR system	[m^3]
V_q	fluid phase volume	[m^3]
V_m	adsorbed volume within a monolayer	[m^3]
$V_{max,meso}$	mesopore volume	[cm^3 STP/g]
$V_{max,micro}$	micropore volume	[cm^3 STP/g]
x	space coordinate	[m]
x_i	molar ratio of component i	[-]
y	space coordinate	[m]
z	space coordinate	[m]

Greek symbols

α	sticking coefficient	[-]
α_s	α_s-plot	[-]
γ_i	activity coefficient of component i	[-]
Γ	thermodynamic correction factor	[-]
$[\Gamma]$	matrix of thermodynamic correction factors	[-]
δ^{in}	characteristic in-of-phase function	[-]
δ^{out}	characteristic out-of-phase function	[-]
δ_{ij}	Kronecker's delta	[-]
ε_p	particle porosity	[-]
$\varepsilon_{SiO_2,x}$	molar extinction coefficient of a specific band corresponding to a molecule adsorbed on silica	[cm/µmol]
$\varepsilon_{ZSM-5,x}$	molar extinction coefficient of a specific band corresponding to a molecule adsorbed on ZSM-5	[cm/µmol]
θ	surface coverage	[-]

θ_t	total surface coverage	[-]
θ_V	fraction of unoccupied sites	[-]
θ_x	surface coverage of molecules in state x	[-]
λ	mean free path	[m]
μ_i	chemical potential of component i	[J/mol]
ρ	density	[kg/m^3]
σ	collision cross section	[m^2]
σ_g	standard deviation in a Gaussian type particle size distribution	[m]
τ_{ad}	time constant of adsorption	[s]
τ_{de}	time constant of desorption	[s]
τ_F	tortuosity of the pore network	[-]
τ_j	mean time between two sequenced jumps	[s]
φ	phase obtained in an FR experiment	[-]
ϕ	phase lag of the vapor pressure	[-]
χ	phase lag of the internal concentration	[-]
φ_B	phase obtained in an blank experiment	[-]
ω	angular frequency	[1/s]

Abbreviations

BET	Brunauer-Emmett-Teller
CAD	computer-aided design
CMA	covariance matrix adaptation
CLD	chemical liquid deposition
FR	frequency response
IUPAC	International Union of Pure and Applied Chemistry
IR	infrared spectroscopy
IZA	International Zeolite Association
MCM	Mobil Composition of Matter
NMR	nuclear magnetic resonance
PFG-NMR	pulsed field gradient nuclear magnetic resonance
QENS	quasi elastic neutron scattering
SBA	University of California-Santa Barbara Mesoporous Material
SBU	secondary building unit
SF	separation factor
TEOS	tetraethyl-orthosilicate
UHV	ultra-high vacuum
ZLC	zero-length column
ZSM-5	Zeolite Socony Mobile-5

Abstract

The sorption in nano-sized, mesoscopically structured ZSM-5 occurs via a weakly bound physisorbed state at the external surface, which concentration is the crucial parameter for the selective sorption enhancement. The general mechanism doesn't change upon addition of a second molecule, but a strong retardation of the bulkier co-sorbate occurs. However, retaining the transport properties in formed particles is difficult due to an additional transport resistance within the newly formed meso- and macropores.

Die Sorption in mesoskopisch strukturierten ZSM-5 Nanokristalliten wird durch die Konzentration des physisorbierten Intermediats an der externen Oberfläche determiniert und kann selektiv beschleunigt werden. Durch Hinzufügen eines zweiten Sorbats ändert sich der generelle Mechanismus nicht, jedoch wird das sterisch anspruchsvollere Sorbat selektiv verlangsamt. Das Erhalten der Transporteigenschaften in geformten Partikeln ist schwierig, da zusätzliche Transportwiderstände in den Meso- und Makroporen des Formkörpers entstehen.

Table of Contents

Chapter 1

General Introduction

The exact knowledge of transport processes in porous media is crucial for the design of new, shape selective catalysts, which are applied in the petrochemical industry. The scope of this thesis is to understand transport properties of nano-sized, hierarchical ZSM-5 on different length scales.

After giving a broad introduction to materials and applied methods in Chapter 2, the transport at pore and interpore length scale will be discussed in the individual chapters. Chapter 2 includes a detailed description of zeolite structures with a focus on mesoscopically structured materials and a summary about the theory of sorption equilibria and diffusion kinetics. Moreover, several techniques for the investigation of transport properties including the underlying mathematical formalism are presented.

In Chapter 3, the effect of surface modification on the transport of light hydrocarbons in ZSM-5 is elucidated on sub-particle (microscale) level by fast-time resolved IR spectroscopy. It is shown experimentally that the sorption in ZSM-5 zeolites proceeds via a previously postulated pre-adsorbed state. Moreover, it can be demonstrated that the concentration of molecules inside this physisorbed surface state is determining the overall sorption rate in nano-sized materials. Post-synthetic silylation enhances the uptake rate by increasing the sticking probability via introducing a stepwise entropy loss (funneling effect) and via establishing a higher concentration of molecules adsorbed at the boundary of the microporous material. On the other hand, the modification blocks a certain amount of pore entrances, which decreases the statistical probability of the pore entrance step.

The knowledge gained on the sorption kinetics of aliphatics determined by fast-time resolved IR spectroscopy is transferred from single components to bimolecular

mixtures in Chapter 4. It examines equimolar mixtures of linear C4-C6 aliphatics with benzene. An extension of the mathematical description based on the Maxwell-Stefan formalism is presented. Detailed kinetic analysis reveals a decrease in adsorption and pore entrance rate of light hydrocarbon molecules by about 10-30%, caused by both a reduction of rate constants and of external surface coverage upon addition of benzene. On the other hand, the apparent diffusion coefficient of benzene decreases by up to 80% in comparison to the single component. The effect can be assigned to a certain blockage of the sites near the pore mouth (window blockage).

   Chapter 5 deals with transport of aromatic molecules on the length scale of formed particles (macroscale). In here, the transport properties of powdered particles, pressed pellets and grown membranes are compared by using the pressure modulation frequency response and Wicke-Kallenbach technique. It can be shown that the governing transport mechanism is shifted upon compacting individual particles into larger moieties towards the newly formed interparticle mesopores. Thus, retaining selectivity created on particle level is difficult and requires careful extrusion. A totally different situation is observed in grown, purely microporous membranes. In here, the transport is determined by microporous diffusion. However, p-xylene permeates faster through the membrane than benzene although the diffusion coefficients determined in single particles predict the opposite. In accordance with the Maxwell-Stefan formalism it can be concluded that the higher surface coverage of p-xylene overcompensates the lower diffusion coefficient.

   In summary, the thesis gives an overview on the influence of post synthetic modifications on the transport of aromatic and aliphatic molecules on all length scales. Moreover, it examines the interdependences of the intracrystalline diffusion, pore entrance step and interparticle diffusion identifying the critical parameters for each of the mechanisms.

Chapter 2

State of the Art

2.1.   *Materials*

2.1.1 Zeolites

Zeolites are a class of microporous (natural or synthetic) tectosilicates, which are utilized intensively in the petrochemical industry due to their unique physical and chemical properties. Those are mechanical, thermal and chemical stability, large surface area, high acid strength and shape selectivity. Typical zeolite catalyzed processes [1] are methanol to gasoline [2], fluid catalytic cracking [3], isomerization [4-10] and alkylation [11-17] as well as the selective reduction of NO_x by ammonia in flue gasses [18]. Moreover, it is possible to prepare zeolite membranes which are effectively used in gas separation [19].

The existence of zeolites was firstly reported by the mineralogist A.F. Cronstedt in 1756, who observed bubbles while heating up the mineral Stibite. This behavior is the origin of the name zeolite, arising from the Greek words zeon (to boil) and lithos (stone) [20]. Since that time the chemistry related to zeolites has been grown tremendously. Nowadays, 206 unique zeolite structures are identified among them 40 which are naturally occurring [21]. All are itemized by a three letter code defined by the IUPAC (International Union of Pure and Applied Chemistry) [22] and the IZA (International Zeolite Association) [21].

The primary building units of zeolites are SiO_4 tetrahedrons, which are linked through the oxygen atoms and built up the crystalline lattice via the so called secondary building units which can be separated in 20 unique polyhedrons (s. Figure 1) [23].
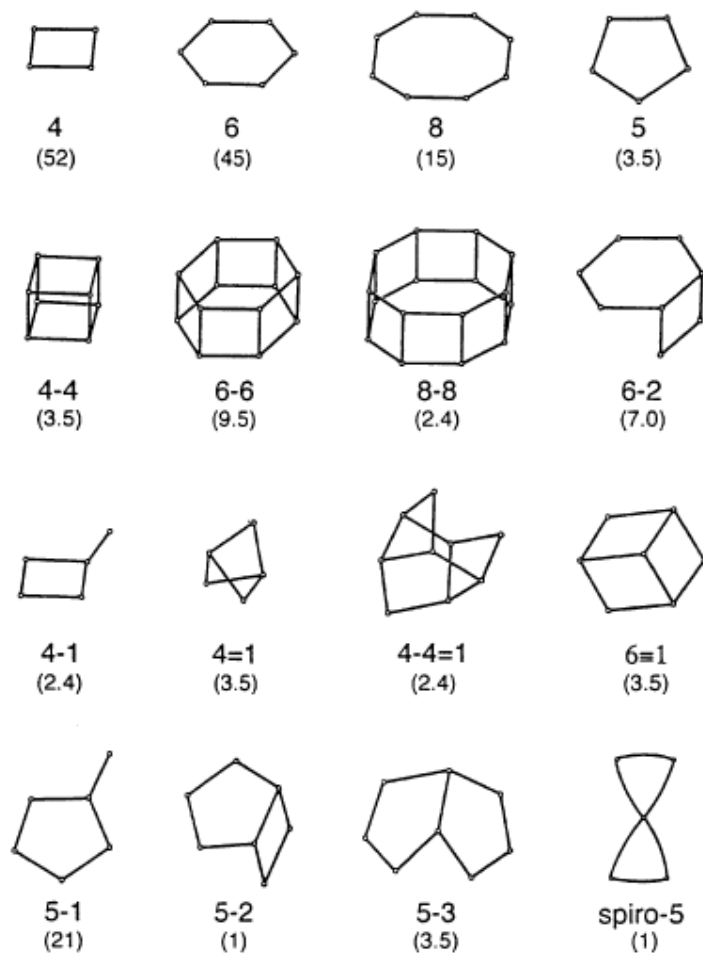
Figure 1: Secondary Building Units (SBU) present in zeolitic materials adapted from Baerlocher et al. [23]

The combination of primary and secondary building units opens up into a large number of complex and structural diverse three dimensional frameworks with pore-systems, cages and super-cages [23].The theoretical amount of zeolite networks exceeds the number of observed structure by at least two orders of magnitude but is not infinite [24], while 213 of them were successfully synthesized [25]. Due to the crystalline structure of zeolites the pore size distribution is very sharp and typically in the range of the kinetic diameters of aromatic and aliphatic molecules. This makes zeolites ideal materials for selective adsorption and shape selective catalysis. A comparison between different adsorber/catalyst materials is presented in Figure 2 [26].

Lewis or Brønsted acids can be introduced into the zeolite lattice by isomorphous exchange of Si^{4+} with Al^{3+} generating a net charge of -1 for each substitution. The

negative charge is compensated by inorganic or organic cations which can be alkali, earth alkali cations, quaternary ammonium ion or protons [27]. If the negative charge is neutralized by a proton a Brønsted acid site is formed which strength depends on the acid site density within the zeolite framework. By this means, the acid strength is inversely proportional to its density. On the other hand a Lewis acid site is formed if an alkali or earth alkali ion compensates the negative charge.
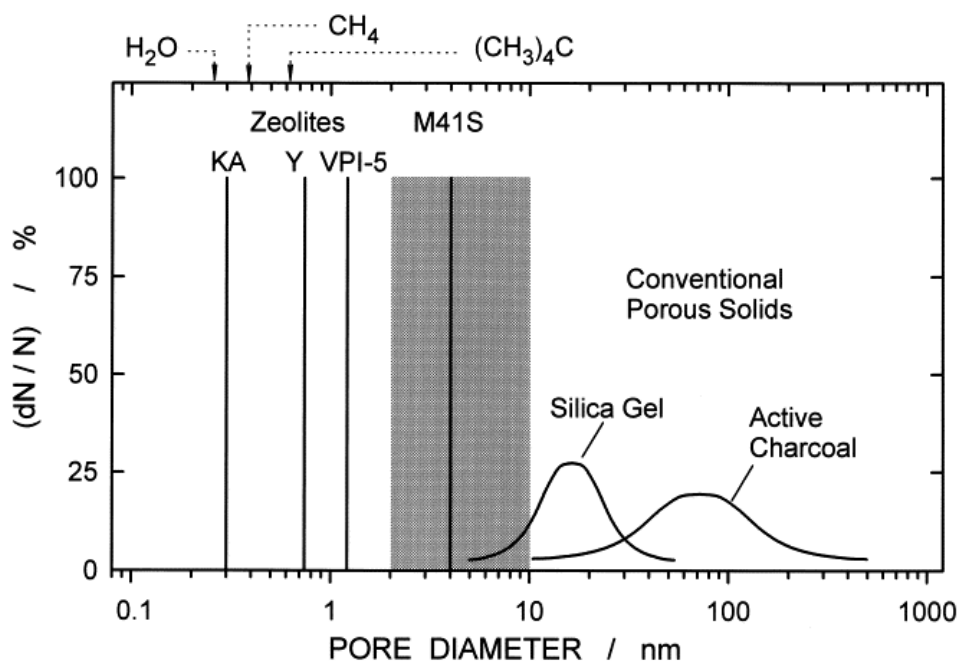

Figure 2: Pore size distribution of zeolites compared to other common, high surface area adsorbents adapted from Weitkamp et al. [26]

In general zeolites are represented by the elemental formula $M_{x/m}[(AlO_2)_x(SiO_2)_y](H_2O)_w$ where m is the charge of the neutralizing cation and w the number of water atoms present. Accordingly, the Si/Al ratio can be defined as y/x. The minimum of this ratio is 1 according to the Löwenstein rule, which states that direct Al-O-Al linkages are forbidden in zeolitic frameworks [28].

One of the most important applications for zeolites is shape selective catalysis and adsorption. The ability to increase the selectivity within a reaction towards one product over the thermodynamically given product distribution or adsorb a reactant selectively out of a mixture can be accounted to three different effects schematically represented in Figure 3.
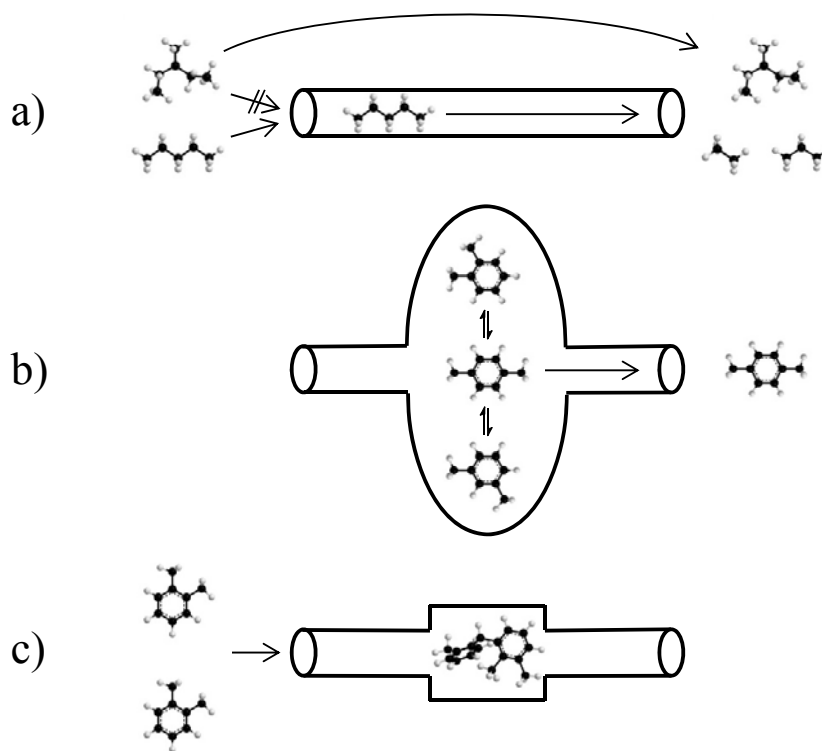
Figure 3: Schematic representations types shape selectivity induced by reactant exclusion (a), product diffusion (b) and a restricted transition state (c).

Those are the reactant exclusion (a), the product diffusion control (b) and the shape selectivity caused by steric restrictions of the transition state (c). In here the principle of reactant exclusion is utilized for selective adsorption [9, 29-31] and dewaxing [32], the product diffusion control for toluene methylation [15, 16] and xylene isomerization [8, 9, 26], in which also the selectivity from steric constraints is applied to prevent transalkylation of the xylene molecules. However, the idea has the general drawback of fast catalyst deactivation due to transport limitations resulting from the intrinsic need for a confined space. A way out of the problem of fast deactivation are mesoporous materials, such as MCM-41 [33] or SBA-15 [34] which have the disadvantage of not being shape selective. Recently developed mesoscopically structured materials combine the high transport rates of mesoporous materials with the shape selectivities of zeolites [35, 36]. This class of catalysts is consisting of microporous domains with large transport cavities in between. Both mesoporous and hierarchical materials are reviewed in the next section.

2.1.2 Mesoporous and hierarchical materials

Materials containing exclusively mesopores are an efficient way to overcome the largest drawback of zeolites, the fast deactivation due to transport limitations. Moreover, mesoporous materials allow the reaction of bulky reactants, which are not suitable for zeolitic catalysts. The first type of mesoporous materials were synthesized in 1992 by researchers of the mobile oil company who developed a procedure using liquid crystal templating resulting in a group of new mesoporous molecular sieves (M41 S) [33]. Such materials have typically thin (0.6-1.2 nm) [37], amorphously structured walls, large surface area and tunable pore sizes [38]. Incorporation of heteroatoms by grafting techniques allow the introduction of different types of active sites into the material [39-41], which makes it suitable for a large variety of catalytic processes [38, 42-44]. However, its low hydrothermal stability due to the thin and amorphous wall structure is a large drawback for industrial applications [45, 46].

In order to increase the hydrothermal stability SBA-15 of a mesoporous silica with thicker walls was developed [34]. SBA-15 contains in contrast to MCM-41 a second porosity within the silica walls, which results from the structure of the template (Pluronic P123) used in synthesis. The intrawall pores are interconnecting the primary mesopore system and consist of either micro- or small mesopores. Equal to MCM-41 also SBA-15 is extensively used for various catalytic applications [47].

Figure 4: Structure of hierarchically structured zeolites represented by the road network of large cities. In zeolites containing mostly micropores a slow transport rate equal is observed equal to the crowded streets of Damascus, whereas mesopores (represented by large roads) interconnecting the micropores (small streets) significantly enhancing the transport similar to the road network of Barcelona (b) and Paris (c) [53].

Due to the intrawall pore system SBA-15 can be denoted hierarchical material. Hierarchical materials are defined as material with structured domains on more than one length scale [48], which can be either artificial or natural. Hierarchical zeolites

have a second (mesoporous) structural domain besides the microporous pore system [35]. The second pore structure can either be introduced during synthesis by solid, supramolecular and indirect templating [35, 49] or by post synthesis methods, i.e. desilication [50], dealumination [51] or steaming [52]. Depending on the starting material different mesostructures are obtained. Overall the different structures of hierarchical zeolites are comparable to road networks of large cities (Figure 4) as illustrated by Perez-Ramirez [51].

Introduction of mesoporosity into the primary crystals of zeolites was shown to be an efficient way to overcome transport limitations [54, 55]. Thus, it is applied in catalysis to either increase the reaction rate in transport limited reaction or increase the stability of a material due to less coke formation [54, 56-61]. However, shortening the diffusion length has the drawback of reducing the shape selective properties. This needs to be overcome in order to make such modifications suitable for all kinds of catalytic processes. One of the main objectives of this thesis is to understand the transport in hierarchical materials on all length scales in order to be able to rationally design new highly active and selective catalysts for the toluene alkylation reaction.

2.2. *Sorption equilibria*

The understanding of sorption equilibria is crucial for the characterization of porous catalysts. A large variety of information, such as surface area, pore volume and pore structure as well as the heat of adsorption of reactants on active sites are obtainable. Structural properties are extracted from nitrogen physisorption experiments whereas information about heats of adsorption are obtained from the sorption of the reactant itself. In this chapter the relevant methods for the analysis of sorption experiments are described, which are generally applicable to all kinds of porous and non-porous media.

   As the transport in microporous solids is most sensitive to pore-sizes and -shapes an exact knowledge of those is essential for the understanding and selective manipulation of transport processes. Moreover, characterization of active sites within catalysts is important to understand reaction mechanisms and to identify the crucial parameters of intrinsic kinetics. Therefore, sorption kinetics and equilibria as well as the role of active sites need to be understood, in order to rationally design new zeolite catalysts.

2.2.1 Langmuir type adsorption

The first consistent and still widely applied adsorption theory was postulated by Langmuir in 1916 [62] by studying adsorption of various gases on metal surfaces. He observed that the sorbed amount increased strongly at lower pressures and then tended to level out at higher pressures. He reasoned that the final stage is a surface monolayer with fully covered adsorption sites. Besides that, the Langmuir model includes the following assumptions [63]:

(1) A finite number of identical adsorption sites is present within the sample, each capable to adsorb one molecule.
(2) The probability that a molecule sticks to the surface is independent of the surface coverage but depends only on the sticking coefficient.
(3) The desorption probability is also independent of the surface occupancy.

In equilibrium the rate of ad- and desorption is equal:

$$p_A * (1 - \theta) * b_1 * \exp\left(-\frac{E_{A,ads}}{RT}\right) = \theta * b_2 * \exp\left(-\frac{E_{A,des}}{RT}\right) \qquad (2.2.1)$$

where θ is the surface coverage, b_1 and b_2 are pre-exponential factors, p_A is the pressure and $E_{A,ads}$ and $E_{A,des}$ are the activation energies for the ad- and desorption, respectively. As physisorption is a non-activated process, the activation energy of adsorption is zero. On the other hand the energy that a molecule needs to overcome during desorption equals the heat of adsorption. From Eq. 2.2.1 the pressure dependent surface coverage at constant temperature also known as Langmuir isotherm can be derived (Eq. 2.2.2):

$$\theta = \frac{K_L p_A}{1 + K_L p_A} \tag{2.2.2}$$

where

$$K_L = \frac{k_{ads}}{k_{des}} = \frac{b_1}{b_2} * \exp\left(\frac{E_{A,des}}{RT}\right) = \frac{b_1}{b_2} * \exp(\frac{-\Delta H_{ads}{}^0}{RT}) \tag{2.2.3}$$

In here, K_L defines Langmuir constant and $\Delta H_{ads}{}^0$ is the heat of adsorption. A description of the pre-exponential factor b_1 can be obtained from kinetic gas theory, in which the adsorption rate can be expressed by the product of the rate of molecules colliding with the surface per unit time and area multiplied by the sticking coefficient:

$$r_{Ads} = \frac{p_A \alpha}{\sqrt{2\pi MRT}} * (1 - \theta) \tag{2.2.4}$$

By comparing Eq. 2.2.1 and 2.2.4 b_1 can be obtained as:

$$b_1 = \frac{\alpha}{\sqrt{2\pi MRT}} \tag{2.2.5}$$

and added into Eq. (2.2.3):

$$K_L = \frac{\alpha}{b_2\sqrt{2\pi MRT}} * \exp(\frac{-\Delta H_{ads}{}^0}{RT}) \tag{2.2.6}$$

For situations with more than one sorbate, Eq. (2.2.2) needs to be refined in order to take the competitive adsorption into account. However also in this case the rate of adsorption and desorption must be equal under equilibrium conditions. For a dual component system the steady state rate equations may be written as [63]:

$$p_A * (1 - \theta_A - \theta_B) * b_1 * \exp\left(-\frac{E_{A,ads,A}}{RT}\right) = \theta_A * b_2 * \exp\left(-\frac{E_{A,des,A}}{RT}\right) \tag{2.2.7}$$

$$p_B * (1 - \theta_A - \theta_B) * b_3 * \exp\left(-\frac{E_{A,ads,B}}{RT}\right) = \theta_B * b_4 * \exp\left(-\frac{E_{A,des,B}}{RT}\right) \tag{2.2.8}$$

The expression for θ_A and θ_B can be derived from the two equations (Eq. 2.27 and 2.2.8):

$$\theta_A = \frac{K_{L,A} p_A}{1 + K_{L,A} p_A + K_{L,B} p_B} \tag{2.2.10}$$

$$\theta_B = \frac{K_B p_B}{1 + K_{L,A} p_A + K_{L,B} p_B} \tag{2.2.11}$$

as well as for the general case of n-sorbates:

$$\theta_i = \frac{K_{L,i} p_i}{1 + \sum_{j=1}^{n} K_{L,j} p_j} \tag{2.2.12}$$

Where $K_{L,i}$ is the Langmuir constant for a general multicomponent component isotherm and p_i the corresponding partial pressure of component i within the mixture of sorbates. The Langmuir constant relates to the thermodynamic equilibrium constant K via the standard state of the sorbate in the gas phase:

$$K = p_0 K_L \tag{2.2.13}$$

The situation gets more complex, if the sorption takes place on two or more energetically different sorption sites. A typical example for such a behavior is the adsorption of n-hexane in ZSM-5, which can either adsorb in the intersections connecting the straight and zig-zag channels or inside the channel interiors [64]. In here, the sorption sites in intersections are energetically favorable and are occupied first. For this kind of adsorption behavior the dual site Langmuir (DSL) [64-67] approach is used (Eq. 2.2.14):

$$\theta_A = \frac{K_{L,1} p_A \frac{n_1^S}{n_t^S}}{1 + K_{L,1} p_A} + \frac{K_{L,2} p_A \frac{n_2^S}{n_t^S}}{1 + K_{L,2} p_A} \tag{2.2.14}$$

If a second type of molecules (B) is present within the system, Eq. (2.2.14) needs to be adjusted according to the sorption behavior of the counter-sorbate. In the easiest case, the Gibbs free energy of adsorption of molecule B is identical for both sites. In this case, the dual component expression is given by Eq. (2.2.15):

$$\theta_A = \frac{K_{L,A,1} p_A \frac{n_1^S}{n_t^S}}{1 + K_{L,A,1} p_A + K_{L,B} p_B} + \frac{K_{L,A,2} p_A \frac{n_2^S}{n_t^S}}{1 + K_{L,A,2} p_A + K_{L,B} p_B} \tag{2.2.15}$$

And the corresponding surface coverage of molecule B is described Eq. (2.2.16):

$$\theta_B = \frac{K_{L,B} p_B \frac{n_1^S}{n_t^S}}{1 + K_{L,A,1} p_A + K_{L,B} p_B} + \frac{K_{L,B} p_B \frac{n_2^S}{n_t^S}}{1 + K_{L,A,2} p_A + K_{L,B} p_B} \tag{2.2.16}$$

In all cases the equilibrium constant K is a measure for the sorbate sorbent interaction strength. By this means, a large K_L corresponds to a strong interaction, which in turn leads a steep isotherm. The Langmuir isotherms for three different equilibrium constants are compared in Figure 5.

From the thermodynamic point of view, K is related to the Gibbs free energy as well as to the adsorption enthalpy and entropy by:

$$K = \exp\left(-\frac{\Delta G_{ads}{}^0}{RT}\right) = \exp\left(-\frac{\Delta H_{ads}{}^0}{RT}\right)\exp\left(\frac{\Delta S_{ads}{}^0}{R}\right) \tag{2.2.17}$$

with

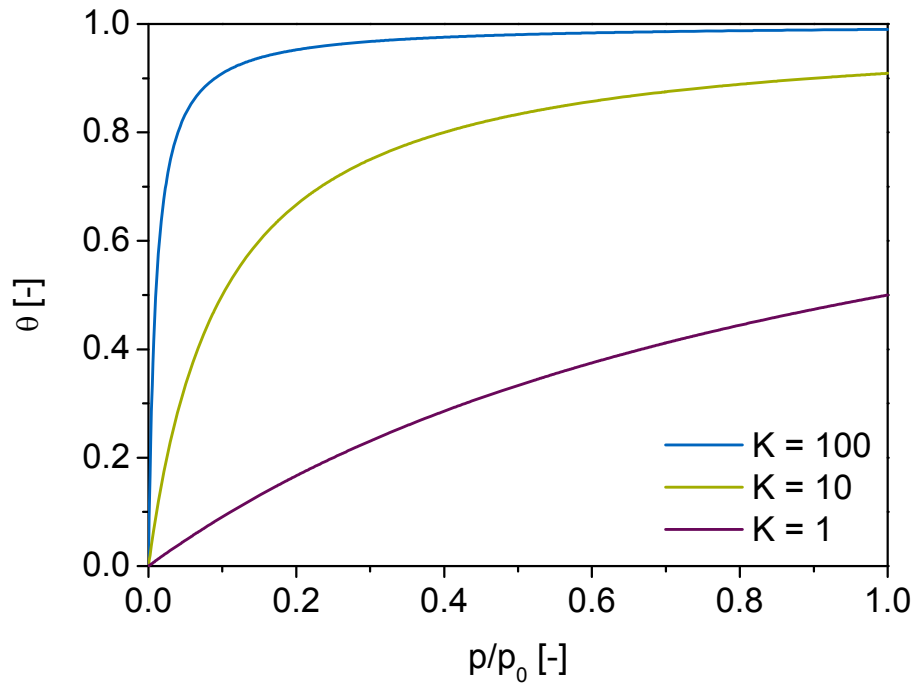$$\Delta G_{ads}{}^0 = \Delta H_{ads}{}^0 - T\Delta S_{ads}{}^0 < 0 \tag{2.2.18}$$

Figure 5: Typical Langmuir isotherms for equilibrium constants K=100, 10 and 1

Eq. (2.2.17) allows the determination of the entropy of adsorption if the equilibrium constant and the heat of adsorption are known. The equilibrium constant can be obtained applying Eq. (2.2.2) in a parameter fit of the experimentally determined adsorption isotherm. The isosteric heat of adsorption can be determined from the temperature dependency of the equilibrium constant using the van't Hoff equation [68]:

$$\left(\frac{\partial lnK}{\partial T}\right)_\theta = \frac{\Delta H_{ads}{}^0}{RT^2} \tag{2.2.19}$$

2.2.2 Multilayer adsorption

For sorbates with a low heat of adsorption such as nitrogen on siliceous matter the assumption of a monolayer formation is not valid. A widely applied concept for the

description of multilayer adsorption was introduced by Brunauer, Emmett and Teller [69]. The description is based on the following assumptions:

(1) Gas molecules adsorb into an infinite amount of layers.
(2) Each layer has the same heat of adsorption
(3) Each layer can be treated with the theory of Langmuir adsorption.

Corresponding to these postulates the surface coverage can be described as:

$$\theta_{BET} = \frac{V_{ad}}{V_m} = \frac{1}{1-c_{BET}} * \frac{c_{BET}*(\frac{p}{p_0})}{1+(c_{BET}-1)*(\frac{p}{p_0})} \qquad (2.2.20)$$

where V_{ad} is the overall adsorbed volume, V_m is the sorbate volume in one monolayer, p is the pressure, p_0 is the vapor pressure above a monolayer and c_{BET} is a constant related to the difference of the heat of adsorption and the evaporation enthalpy [68]. Eq. 2.2.20 can be rearranged to the classical linearized BET equation (2.2.21):

$$\frac{\frac{p}{p_0}}{V_{Ad}*(1-\frac{p}{p_0})} = \frac{1}{c_{BET}*V_m} + \frac{(c_{BET}-1)*(\frac{p}{p_0})}{c_{BET}*V_m} \qquad (2.2.21)$$

From the slope and the intercept of the straight line obtained by plotting $\frac{\frac{p}{p_0}}{V_{Ad}*(1-\frac{p}{p_0})}$ against $(\frac{p}{p_0})$, typically in the range from $0.05 - 0.3 \frac{p}{p_0}$, the volume present within a monolayer, the c_{BET} value and the surface are can be determined. For a meaningful BET analysis a positive c_{BET} value is crucial. It is worth noting, that the BET analysis is in a strict sense limited to macro- and mesoporous materials. By this means, the adsorption should not be accompanied by micropore filling, which may falsify the results [70]. Therefore, the analysis of microporous materials needs to be done with care and results by no means a physically relevant surface area but an apparent surface area able to characterize the material relative to other microporous materials.

Besides the two shapes of adsorption isotherms discussed in detail, Langmuir and BET others appear within adsorption experiments depending on the sorbent structure and the forces during the adsorption, which were classified by the IUPAC in 1985 [70]. The classification consists of six different types of isotherms presented in Figure 6. Type I isotherms represent the typical case of adsorption in microporous solids with a relatively small external surface area, in which the adsorbed amount is governed by the micropore volume rather than by the internal surface area [70].
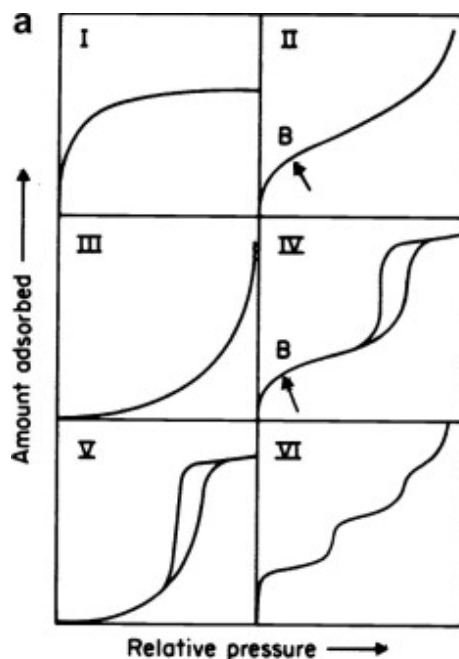
Figure 6: IUPAC definition of standard adsorption isotherms [70]

Isotherms of type II are observed in non-porous or macroporous solids. It is characterized by a reversible, unlimited monolayer-multilayer formation and is the ideal case of the BET model. In here, B is assigned to be the stage at which a monolayer is present and multilayer formation starts. Type III isotherms are somewhat similar to type II isotherms by showing reversible and unlimited multilayer formation. However, the multilayer formation proceeds without establishment of a previous monolayer formation and thus, point B is not observed. This type of isotherm is typical for sorbate-sorbent systems with strong sorbate-sorbate interactions [70].

The nitrogen physisorption isotherms observed hierarchical micro- mesoporous materials are of type IV. Its form is similar to the type II isotherm but it contains a hysteris loop caused by capillary condensation within the mesopores. Thus, the sharp increase in the beginning can be attributed to monolayer formation within the micropores, mesopores and at the external surface which is followed by multilayer formation within the mesopores. Typically, the mesopore volume determines the maximum amount of adsorbate as the unlimited multilayer formation at the external surface of the sample is negligible [70].

Type V isotherms occur within mesoporous materials with a weak adsorbate-adsorbent interaction and are very uncommon. The specific feature of type VI isotherms is the stepwise multilayer formation occurring on a uniform non-porous surface. In here, the sharpness of the steps depends on the specific sorbate-sorbent system and on the temperature [70].

Additionally to the type of isotherm, the form of the hysteresis provides information about the type of mesopores present. The IUPAC defines four different hysteresis loop shapes presented in Figure 7 , which were analyzed in detail by Rouquerol et al. [71]. The characteristic feature of type H1 hysteresis loops is a very steep, nearly parallel adsorption-desorption branch and its fairly small size. It is typical for materials with unconnected mesopores which consists of a small uniform pore size distribution such as MCM-41.
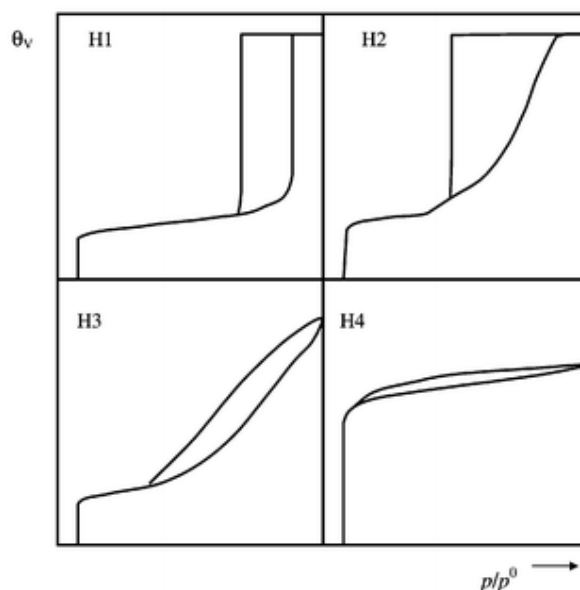
Figure 7: IUPAC definition of shapes of hysteresis loops [70]

The H2 loop is broad and consists of a long plateau followed by a sharp desorption branch. It is can be assigned to a complex interconnected mesopore structure and is typical for many porous oxide gels and hierarchical zeolites. In the case of slit shaped pores, hysteresis loops of type H3 and H4 are observed. In contrast to H1 and H2 the adsorption isotherm does not exhibit a plateau at high p/p_0 but shows a constant decrease.

2.2.3 Analysis of nitrogen physisorption isotherms

Additionally to the BET surface area and qualitative description of the isotherm's shape, a quantitative characterization of the sample in terms of overall micro- and mesopore-volume, external surface area and pore size distribution becomes feasible by analysis of nitrogen physisorption isotherms. In here, two methods are widely applied for the determination of pore volumes, which are the t-plot [72] and the α_s analysis [73]. The principle of both methods is the comparison of the measured with a reference isotherm. For this purpose a calculated reference isotherm on a non-porous solid is used for the t-plot method whereas it is experimentally determined for the α_s analysis. The main advantage of the α_s method is that the reference data can be chosen according to the examined system. Thus, the α_s method is considered to be more accurate [71] because similar chemical composition of the reference and the sample and identical experimental conditions enhance the quality of the results. For zeolites and other nanoporous silicas, a macroporous silica is used as reference [74]. A typical α_s plot for a hierarchical material is presented in Figure 8.

Linearity occurs when the sample acts equally to the reference, thus, the amount of adsorbed nitrogen increases similarly to a non-porous material. In hierarchical materials, two linear regions are present, the first one after complete filling of the micropores and the second one after saturation of the mesopores. Those can be described by Eq. (2.2.22) and (2.2.23), respectively [73]:

$$v(p) = v_{max,micro} + k_{Std}S_{ext+meso}\alpha_s \qquad (2.2.22)$$

$$v(p) = v_{max,meso} + k_{Std}S_{ext}\alpha_s \qquad (2.2.23)$$

where $v_{max,micro}$ and $v_{max,meso}$ are the amount of nitrogen at complete pore filling within the micro- and the mesopores, S_{ext} is the external surface area, $S_{ext+meso}$ is the sum of the external and the mesopore surface area and k_{Std} is the amount of a nitrogen monolayer on the reference (at $\frac{p}{p_0}$=0.4) divided by its surface area. According to Eq. (2.2.22) and (2.2.23) the micro- and mesopore volumes are accessible from the intercept of the linear regions whereas the slope contains the mesopore and external surface area.

Besides the determination of surface areas and pore volumes, pore size distributions are directly accessible from nitrogen physisorption experiments. The classical way was developed by Barrett, Joyner and Halenda (BJH-method) [76] and is by far the most common way of accessing pore sizes and volumes. Recently, methods based on

non-linear density functional theory (NLDFT) were developed, which are applicable to a large variety of pore geometries including hierarchical materials [77, 78]. Due to a higher accuracy only the latter are applied in the presented work.
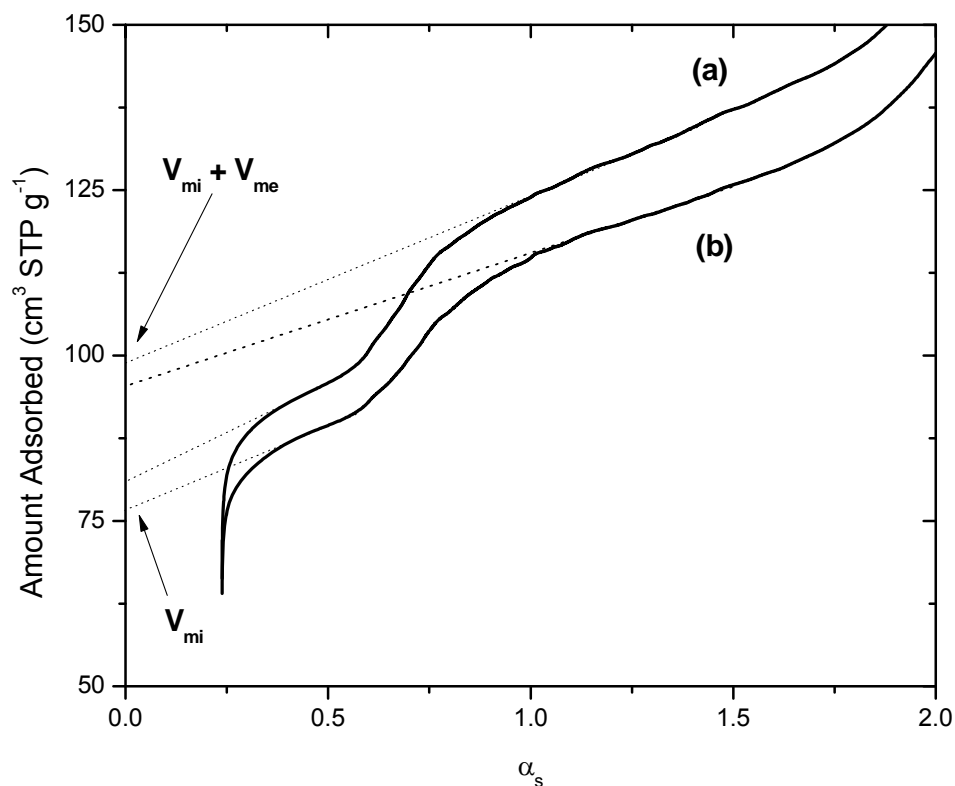

Figure 8: Exemplary α_s-plots of two hierarchical zeolites [75] consisting of a micro- and a mesoporous domain.

   In conclusion, physisorption experiments provide information about surface area as well as pore-size and -volume distributions. Thus, a detailed analysis of physisorption isotherms is crucial for the description of pore systems in hierarchical zeolites, which is the basis for the understanding of the transport processes.

2.3 Transport in hierarchical zeolites

For the rational design of new, hierarchically structured zeolite catalysts e.g. for the toluene methylation reaction, an in-depth knowledge of transport properties on all length scales is crucial. This includes the understanding of the influence of molecule-molecule interactions on the transport parameters. Thus, a combination of different experimental as well as computational techniques is necessary to fully describe the mass transport in microporous samples.

Over the last decades a large variety of methods were developed to examine the diffusivity in all kinds of materials. They can be separated according to the length scale examined into microscopic, mesoscopic and macroscopic methods [79]. Microscopic techniques investigate transport below the size of the individual crystal or particle. The obtainable measure is the self-diffusivity of the sorbate in the given environment, e.g. the force field of the zeolitic micropore. The most common methods to study self-diffusivities are pulsed field gradient-NMR (PFG-NMR) [80-82] and quasi elastic neutron scattering (QENS) [83], but also other methods like tracer zero length column (ZLC) [84] are suitable. Besides that, theoretical calculations e.g. molecular dynamic (MD) simulations [85, 86] are able to determine diffusivities in microporous channels quantitatively.

Information about transport properties at particle level are obtained from mesoscopic methods, which are by far most common. The obtained transport diffusivity is not limited to the diffusion within the zeolite crystal, but also includes the processes at the crystal boundary, such as surface resistance [87]. The applicable methods are of microscopic [88-91] and spectroscopic [75, 92] nature but also gravimetric uptake rate measurements [93] and frequency response techniques [94-98] are being used.

Macroscopic methods observe the overall transport from the bulk of the fluid phase to the sorption site at the porous material. For industrial applications the micro- and mesoscopic diffusivities are only of interest if they have an impact on the macroscopic transport rate. In other words, macroscopic effects such as diffusion within the mesopores formed during extrusion of the catalyst are able to influence/retard the intrinsic transport properties [99]. Thus, the understanding of transport within formed particles is of high importance for the design of next

generation catalytic materials. Moreover, the development of nanoporous membranes for gas separation depends critically on the understanding of macro-level transport.

In general, all mesoscopic methods are able to measure transport on macroscopic scale. Additionally measurement of permeation through pressed particles or microporous membranes, e.g. in Wicke-Kallenbach [100] type instruments are suitable.

Studies on sorbate mixtures can be carried out by all microscopic, mesoscopic and macroscopic techniques discussed previously [64, 83, 99, 101-111]. However, all of the studies published, which examined transport on particle level, are restricted to intracrystalline diffusion and, moreover, explicitly exclude surface barriers. On the other hand macroscopic investigations by permeation measurements in micro- and mesoporous membranes including the corresponding models are widely applied [101, 112-117].

The following section gives a short introduction into fundamentals of diffusion and the underlying diffusion mechanisms in different environments (micropores, mesopores, and mixtures). An overview about the mentioned experimental techniques with a focus on those applied within the present work is given in section 2.4.

2.3.1 Mathematical formalism

The most common mathematical formalism for the description of diffusional mass transport was developed by Fick in 1855. The theory is based on the hypothesis that the transfer rate F through a unit area of a plane is proportional to the concentration gradient $\delta c / \delta z$ normal to the plane, with the diffusion coefficient D as proportionality constant. Under the assumption of isotropic media, Fick's first law is espressed by [118]:

$$F = -D * \frac{\delta c}{\delta z}$$
(2.3.1)

From equation 2.3.1 the differential equation describing the time dependence of the concentration can be derived considering the volume element shown in Figure 9. Due to conservation of mass the increase in concentration over time equals the difference in number of molecules entering and leaving a volume element divided by the volume between z and $z + dz$:

$$\frac{\delta c}{\delta t} = \frac{y * z * [F(z) - F(z+dz)]}{y * z * dz}$$
(2.3.2)

With

$$F(z + dz) = F(z) + \frac{\delta F}{dz} dz \tag{2.3.3}$$

Eq. 2.3.2 reduces to:

$$\frac{\delta c}{\delta t} = -\frac{\delta F}{dz} \tag{2.3.4}$$

By inserting Eq. 2.3.1 into 2.3.4 Fick's second law describing the time dependent diffusion is obtained:

$$\frac{\delta c}{\delta t} = D * \frac{\delta^2 c}{\delta z^2} \tag{2.3.5}$$

The partial differential equation presented in Eq. 2.3.5 is the basis for the mathematical description of most of the methods herein and are solved according to the individual boundary conditions. The solutions will be discussed together with the particular techniques.
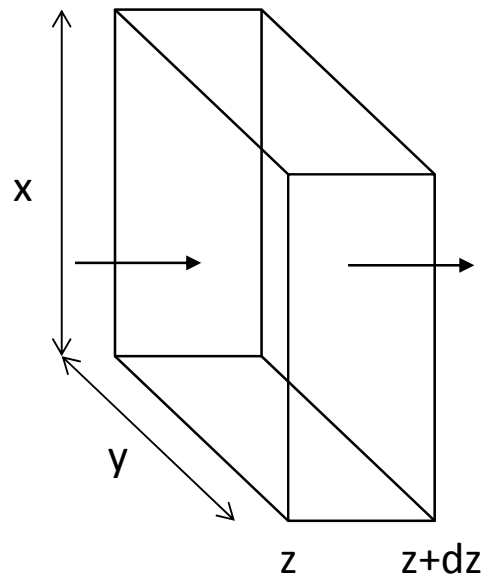
Figure 9: Volume element for the derivation of Fick's and Maxwell-Stefan transport equations.

However, in a strict sense Fick's law is only valid in binary mixtures or for diffusion of dilute species in multicomponent mixtures [119]. Moreover, the absence of electrostatic and centrifugal forces is required. A more general theory was given by James Clerk Maxwell and Josef Stefan, the Maxwell-Stefan formalism. It is based on the assumption of an equilibrium between the molecular friction and the thermodynamic force (TF) of the diffusing molecules [120]. Any deviation from the equilibrium induces diffusive mass transport.
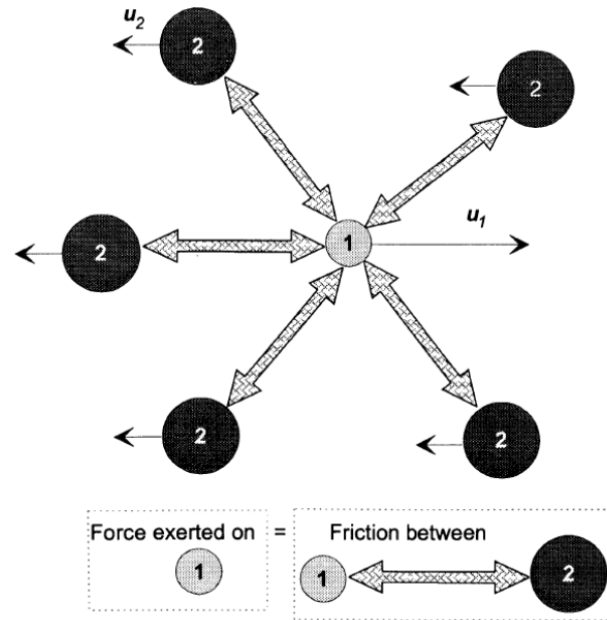
Figure 10: Pictorial representation of the forces and interparticle friction between species 1 and 2 relative to each other during the motion of the molecules. Adapted from Ref. [121].

In order to derive the transport equations for the simplest case, z-directional diffusion in a binary system and defined volume element (Figure 9, x=y=1 m) is considered, where the diffusion length is dz. If the partial pressure of component i changes along the diffusion distance dz by $-dp_i$ the force acting per m³ is:

$$TF = \frac{-dp_i}{dz} \tag{2.3.6}$$

As the concentration of component i is c_i the force acting per mole is given by:

$$TF = \frac{1}{c_i}\frac{-dp_i}{dz} \tag{2.3.7}$$

Under the assumption of an ideal gas behavior c_i can be expressed by Eq. (2.3.8):

$$c_i = \frac{p_i}{RT} \tag{2.3.8}$$

This can be inserted into Eq. 2.3.7 resulting another expression for the molar based thermodynamic driving force:

$$TF = \frac{RT}{p_i}\frac{-dp_i}{dz} = -RT\frac{-d\ln(p_i)}{dz} = \frac{-d\mu_i}{dz} \tag{2.3.9}$$

which is equal to the chemical potential gradient at constant temperature and pressure. This is balanced by the friction between the moving species, which is proportional to the velocity difference $(u_1 - u_2)$, the concentration of the counter diffusing species

expressed by its molar ratio, x_2 and a drag coefficient $\frac{(RT)}{\mathbb{D}}$. The resulting force balance is presented in Eq. 2.3.10:

$$\frac{-d\mu_1}{dz} = \frac{RT}{\mathbb{D}}(u_1 - u_2)x_2 \tag{2.3.10}$$

For a transport of species 1 in z direction ($u_1 > 0$), $\frac{-d\mu_i}{dz}$ has to be positive and can be understood as the true driving force of diffusional transport [119]. Please note here, that the physical meaning of the Maxwell-Stefan diffusion coefficient ($\mathbb{D}$) is that of an inverse drag coefficient. Eq. 2.3.10 can be simplified by multiplying both sites with x_1 and dividing by RT:

$$\frac{x_1}{RT}\frac{-d\mu_1}{dz} = \frac{x_1 x_2 u_1 - x_1 x_2 u_2}{\mathbb{D}} \tag{2.3.11}$$

Using the general expression for the molar flux with respect to a fixed reference frame:

$$N_i = c_t x_i u_i \tag{2.3.12}$$

Eq. 2.3.11 yields after vector generalization:

$$-\frac{x_1}{RT}\nabla_{T,p}\mu_1 = \frac{x_2 N_1 - x_1 N_2}{c_t \mathbb{D}} \tag{2.3.13}$$

In order to account for non-ideal behavior the chemical potential is replaced by the component activity coefficient, γ_i. Thus, the left side of Eq. 2.3.13 changes to:

$$-\frac{x_1}{RT}\nabla_{T,p}\mu_1 = -\left(1 + x_1\frac{\partial \ln(\gamma_1)}{\delta x_1}\right)\nabla x_1 = -\Gamma\nabla x_1 \tag{2.3.14}$$

where Γ is the thermodynamic correction factor. Inserting Eq. (2.3.14) into (2.3.10) and using the relation:

$$x_2 = (1 - x_1) \tag{2.3.15}$$

results the final expression for the diffusive flux:

$$N_1 - x_1 N_t = F_1 = -c_t \mathbb{D}\Gamma\nabla x_1 \tag{2.3.16}$$

Under the boundary conditions of (i) binary mixture and (ii) diffusion occurs only in z direction Eq. 2.3.16 can be simplified to:

$$F_1 = -\mathbb{D}\Gamma\frac{\delta c_1}{\delta z} \tag{2.3.17}$$

A comparison between the flux given by Fick's law (Eq. 2.3.5) and Maxwell-Stefan approach (Eq. 2.3.17) reveals the following relationship the two types of diffusion coefficients:

$$D = \mathbb{D}\Gamma \tag{2.3.18}$$

The general equations based on the Fick and the Maxwell-Stefan formalism presented in Eqs. 2.3.5 and 2.3.13, respectively, are the basis for the mathematical description of all of the methods presented within this thesis and are solved according to the individual boundary conditions. The solutions will be discussed in the sections of the particular techniques.

2.3.2 Diffusion mechanisms

Diffusional mass transport takes place via different mechanisms depending on the mean free path of the molecules and the environmental confinements. In porous materials a rough separation according to the pore size is feasible and is presented in Figure 11. Besides the change in diffusional regime also the diffusion coefficient drops drastically with increasing sterical constraints [122]. The following section discusses the most common diffusion mechanism. Especially those occurring in hierarchical zeolites will be highlighted.

2.3.3 Molecular diffusion

Molecular diffusion occurs, if the mean free path of the diffusing molecule is much smaller than the pore size, thus $dp \gg \lambda$ where [68]:

$$\lambda = \frac{k_B T}{\sqrt{2} \sigma p} \tag{2.3.19}$$

In here k_B is the Bolzmann constant, T is the temperature, σ is the collision cross section and p is the pressure. This type of diffusional regime occurs ether in the bulk phase of a fluid or within macropores. Due to the absence of other constraints the diffusion rate is restricted by the temperature and the collision frequency between the molecules. An expression for the diffusion coefficient can be found with the help of kinetic gas theory [68]:

$$D = \frac{\lambda * u}{3} = \frac{\lambda}{3} * \sqrt{\frac{8RT}{\pi M}} \tag{2.3.20}$$

where R is the ideal gas constant, u is the average speed of molecular movement and M is the molecular weight of the diffusing substance. In conclusion, the molecules in the regime of molecular diffusion move randomly in all three dimensions, equally to Brownian molecular movement.
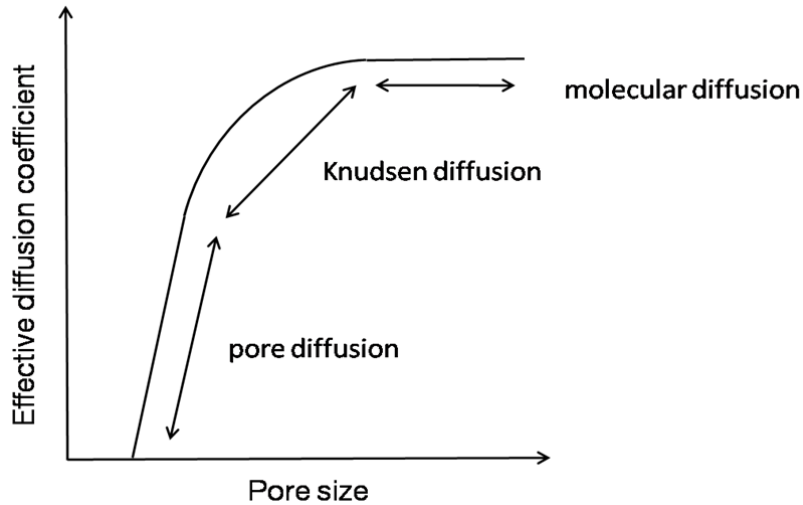
Figure 11: Dependency of the effective diffusion coefficient and the diffusional regime on the pore size of the porous material

2.3.4 Knudsen diffusion

The regime of Knudsen diffusion is characterized by higher frequency of molecule-pore wall than molecule-molecule collisions. Thus, the mean free path of the molecule described by Eq. 2.3.6 is large compared to the pore size. The critical parameters for the diffusional mode are the pressure and the pore size. The critical pore diameters dependent on the sorbate partial pressure are summarized in Table 1. It is obvious that in the relevant pressure region of about 10-50 Pa Knudsen diffusion occurs in mesopores smaller than 10 nm.

Table 1: Critical pore diameters for the occurrence of Knudsen diffusion dependent on the sorbate partial pressure [123]

d_p [nm]	<1000	<100	<10	<2
p [10^5 Pa]	0.1	1	10	50

Under the given boundary conditions the diffusive flow within the Knudsen regime can be described according to Fick's first law:

$$F = -D_K * \frac{\delta c}{\delta x}$$ (2.3.21)

where D_K is the Knudsen diffusion coefficient. This coefficient can be derived in a cylindrical pore from kinetic gas theory (Eq. 2.3.20) by replacing the mean free path with the pore diameter [124]:

$$D_K = \frac{d_p}{3} * \sqrt{\frac{8RT}{\pi M}} \tag{2.3.22}$$

The pore geometry in real systems hardly matches the form of cylindrical pores but may be described as a network of interconnected mesopores with a certain tortuosity. Thus, an effective Knudsen diffusion coefficient $(D_{K,eff})$ taking the porosity (ε_p) and tortuosity (τ_F) of the pore network into account are defined by:

$$D_{K,eff} = \frac{\varepsilon_p}{\tau_F} * \frac{d_p}{3} * \sqrt{\frac{8RT}{\pi M}} \tag{2.3.23}$$

By combining Eqs. 2.3.21 and 2.3.23 a representation for the effective diffusive flow in the Knudsen regime can be derived:

$$F = -\frac{\varepsilon_p}{\tau_F} * \frac{d_p}{3} * \sqrt{\frac{8RT}{\pi M}} * \frac{\delta c}{\delta x} \tag{2.3.24}$$

2.3.5 Surface diffusion

In pores smaller than 2 nm, molecules do not leave the force-field of the zeolitic crystal while moving through the pore system. The corresponding diffusion mechanism is widely known as surface, pore, configurational, intracrystalline or micropore diffusion. However, all this terms describe the same type of underlying transport mechanism, which is the so called hopping mechanism [125]. In here the motion of the molecules takes place via hopping between two energy minima within the zeolitic framework often referred as adsorption sites.

The diffusive flux can be defined according to Fick's first law:

$$F = -D_H * \frac{\delta c}{\delta x} \tag{2.3.25}$$

where D_H is the diffusion coefficient for the hopping mechanism. For the simple case of diffusion on the plain surface the diffusion coefficient can be described by [126]:

$$D_H = D_0 * \exp(-\frac{e\Delta H_{Ads}}{RT}) \tag{2.3.26}$$

In here D_0 is the pre-exponential factor, e is an experimental factor and ΔH_{Ads} is the heat of adsorption. From Eq. 2.3.12 it is obvious that the diffusion coefficient is inversely proportional to the heat of adsorption. All other parameters e.g. channel size and geometry are expressed by the pre-exponential factor D_0 and the experimental factor e.

Due to the high complexity of nanoporous networks the complete understanding of diffusion in micropores was not achieved so far. Thus, the diffusion coefficient cannot

be calculated by a simple equation but needs to be determined ether by molecular dynamic (MD) simulations [127] or with experimental methods [75, 80, 93, 100].

2.3.6 Single file diffusion

Another type of diffusion, especially important for understanding of gas separation by microporous membranes is the single file diffusion. If the kinetic diameter of the sorbates is similar or equal to the pore size, molecules are not able to pass each other anymore in unimolecular channel system. [128-130] In this case, the mean displacement of a molecule within the zeolite pore (self-diffusion) changes with the square root of time (Eq. 2.3.27) which is in contrast to Einstein's equation (Eq. 2.3.28) valid for ordinary diffusion [129]:

$$\langle r^2(t) \rangle = 2F\sqrt{t} \qquad (2.3.27)$$

$$\langle r^2(t) \rangle = 2Dt \qquad (2.3.28)$$

where F and D are given by Eq. 2.3.29 and 2.3.30, respectively:

$$F = l^2 \frac{1-\theta}{\theta} \frac{1}{\sqrt{2\pi\tau_j}} \qquad (2.3.29)$$

$$D = \frac{l^2}{2\tau_j} \qquad (2.3.30)$$

In here, l is jump length between two sorption sites, θ is the surface coverage and τ_j is the mean time between succeeding jumps.

2.4 Experimental determination of transport properties

This section gives a detailed description of the experimental methods used in this thesis, including all mathematical derivations necessary for the interpretation of the experimental data. Diffusion in the macroscale is studied by the Wicke-Kallenbach technique [100], mesoscale transport is examined time resolved IR uptake experiments as well as pressure modulation frequency response techniques. [94, 95, 97]. The mechanistic aspects of the pore entrance step, both in single and dual component mixtures are elucidated on a microscopic level by fast time resolved IR spectroscopy. [75, 92]. However, a lot more methods were developed through over the last decades, which were discussed in several excellent reviews in the literature [131-133].

2.4.1 Wicke Kallenbach technique

The Wicke Kallenbach technique [100] is a widely applied method for the determination of transient and steady state permeation through mesoporous pellets or microporous membranes. A sketch highlighting the measurement principle is given in Figure 12.
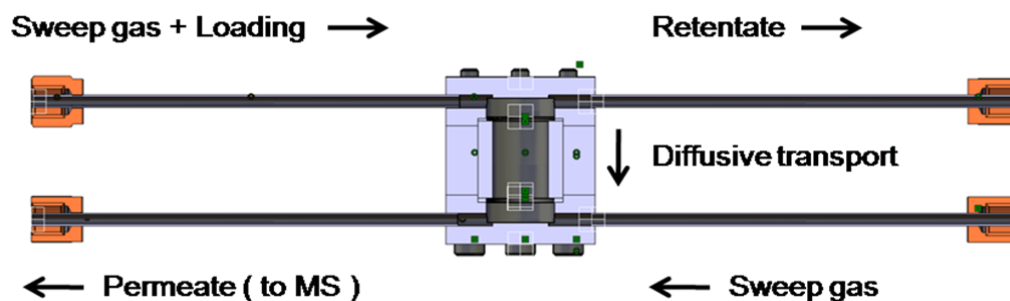
Figure 12: Experimental setup in a typical Wicke Kallenbach experiment.

The measurement cell is constructed to hold the sample in a 90° angle relative to two countercurrent gas flows and separate those. One of them is either a loaded carrier gas stream or contains the pure sorbate or sorbate mixtures. The other one consists of pure sweep gas. If the pores within the sample are large enough for the sorbate to pass, it diffuses along the concentration gradient (Eq. 2.4.1) through the sample. It is obvious that the molecular flow rate is directly related to the diffusivity. Please note, that the pressure need to be identical on both sites of the sample in order to avoid pressure driven transport.

The transport can be described by the Fick's first law (Eq. 2.3.1). At steady state conditions and with the assumption of a constant diffusion coefficient (valid at low coverages) the concentration gradient through over the sample can be linearized and an expression for the transfer rate is derived:

$$\dot{n} = -D\frac{A_S}{\Delta z}(c_{permeate} - c_{feed}) \qquad (2.4.1)$$

where A_S is the surface area in contact with the loaded gas flow and Δz is the thickness of the wafer. The parameters $c_{permeate}$ and c_{feed} are the permeate and the feed concentrations, respectively. With the transfer rate being the product of the volumetric flow rate and the permeate concentration (Eq. 2.4.2) the diffusion coefficient can be calculated by Eq. 2.4.3:

$$\dot{n} = Qc_{permeate} \qquad (2.4.2)$$

$$D = \frac{Qc_{permeate}}{(c_{feed} - c_{permeate})} * \frac{\Delta z}{A_S} \qquad (2.4.3)$$

Besides the diffusion coefficient also the separation factor (SF) is directly accessible, which is most important for membrane applications. It describes the separation selectivity of a material and is calculated from the experimental data by Eq. 2.4.4:

$$SF = \frac{c_{permeate,1}}{c_{feed,1}} \bigg/ \frac{c_{permeate,2}}{c_{feed,2}} \qquad (2.4.4)$$

Experimental setup

A detailed CAD model of the experimental cell is presented in Figure 13. It consists of a top (a) and a base (f) full metal plate with tubings for the gas in- and outlet. The sample is placed in a stainless steel sample holder (d), which is surrounded by an aluminum ring (c) holding the screws. The connection between the sample holder and the top/base plate is sealed with graphite (b,e). The gas flows are connected according to Figure 12 and the temperature within the cell is controlled via an Eurotherm 2404 PID controller.

The volumetric flow rates are controlled by Bronkhorst EL-flow select mass flow controllers. Loading of the carrier gas with liquid sorbates is performed via self-constructed saturators shown in Figure 14. In here, the carrier gas in flowing through the liquid sorbate placed in a ½" tubing (a). In order to guarantee a constant loading equal to the partial pressure of the sorbate, the loaded stream passes a second, empty ½" tubing (b), in which a potential sorbate excess is condensed. Moreover, this tube prevents flushing of the system with sorbate in case of an overpressure at the inlet or

vacuum at the outlet of the saturator. Three way valves (c,d) allow to bypass (e) the saturator, e.g. for activation of the sample. The saturators are placed into a cooling bath operated at 15°C to avoid sorbate condensation inside the system. The permeate stream is analyzed with a Hiden Analytical mass spectrometer (WR13302) in MID mode with a time resolution of 22.5 s. The overall setup is presented in Figure 15.
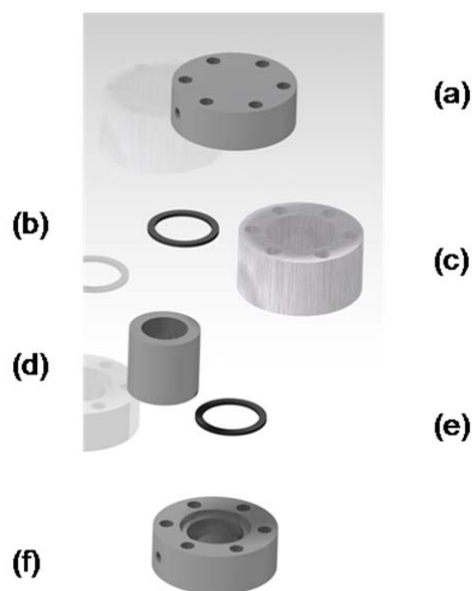
Figure 13: CAD Model of the Wicke Kallenbach cell containing two end plates (a,f), two graphite sealings (b,e), an outer aluminum ring (c) and the inner stainless steel ring holding the sample (d).
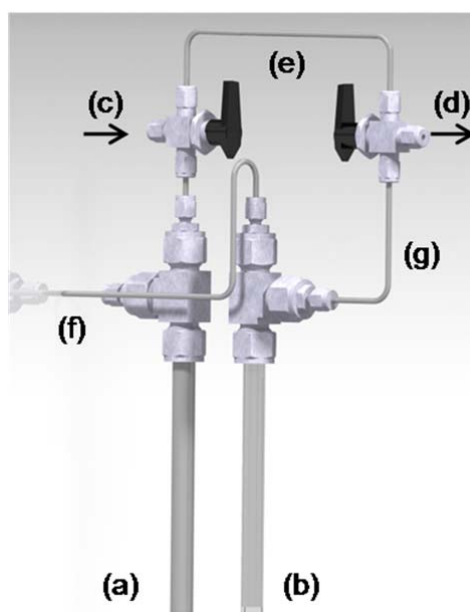
Figure 14: CAD model of a self-constructed saturator used for loading the carrier gas with liquid hydrocarbons placed in a ½" metal tubing (a). A second, empty tubing (b) guarantees constant loading. Two three way valves (c,d) allow bypassing the saturator (e).
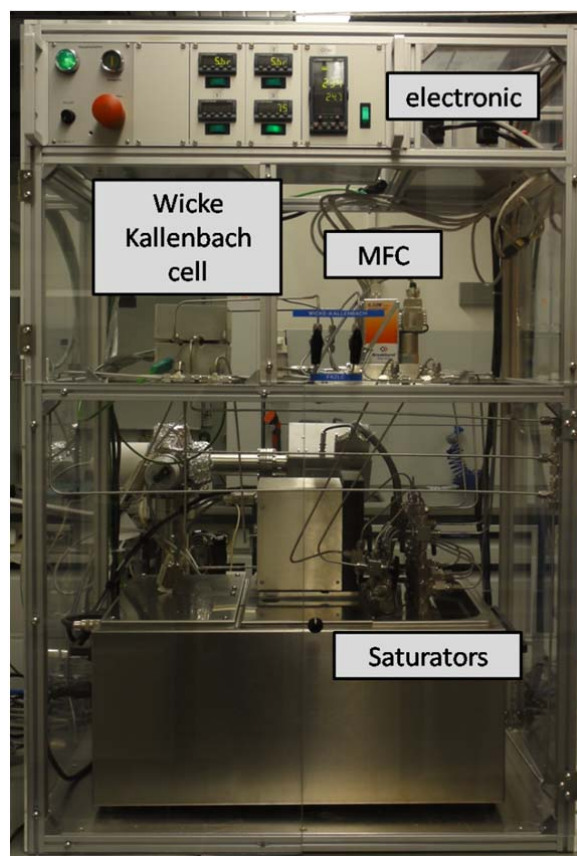
Figure 15: Setup for permeation experiments containing a Wicke Kallenbach cell, mass flow controllers, saturators and the electronics for controlling the temperature and the flow rates.

Sample preparation and experimental conditions

The powdered samples are pressed with 20 kN for 2 minutes into the stainless steel sample holder (Figure 13 (d)) using a custom made pressing tool shown in Figure 16. The crystalline membranes are placed between two steel rings sealed with graphite. Afterwards, the sample is mounted into the Wicke Kallenbach cell, flushed with 50 ml/min Helium for 0.5 h and activated at 823K for 1h with an incremental heating rate of 10K/min.

The experiments are carried out with a constant flow rate of 50 ml/min. To avoid pressure gradients the flow rates on both sites of the samples are identical. Loading with liquid sorbate is performed with a volumetric flow rate of 2 ml/min for benzene and 18 ml/min for p-xylene which results in a ratio of 1.33/1 benzene/p-xylene in the feed. The overall sorbate partial pressure is kept at about 500-1000 Pa.

In order to determine temperature dependences, measurements at 343, 373 and 403K as well as at 313, 343 and 403K are conducted for pressed pellets and crystalline membranes, respectively.
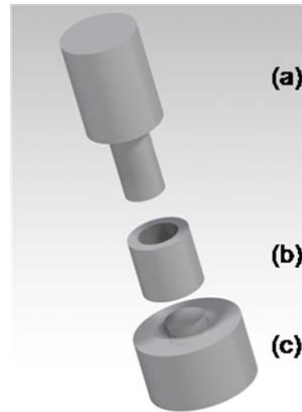
Figure 16: CAD model of the pressing tool used to compact powdered sample into the sample holder (b) of the Wicke Kallenbach permeation cell containing of a plunger (a) and the stamp pad (c). The whole instrument is made of stainless steel.

2.4.2 Pressure modulation frequency response

Pressure modulation frequency response is a method to analyze transport processes on the mesoscale level. Thus, all transport steps occurring within an isolated particle are investigated. The basic principle of this method is to determine the equilibration behavior of sorbate-sorbent system upon small perturbations of the sorption equilibrium represented in Figure 17. Hence, the processes determining the kinetics of re-equilibration are investigated, in which the transport is the rate determining step for the aromatic-ZSM-5 system. The method is able to differentiate between parallel transport processes as they occur as additive functions in the frequency domain. This is a unique feature and makes the method extremely feasible for investigations of complex transport networks [97].
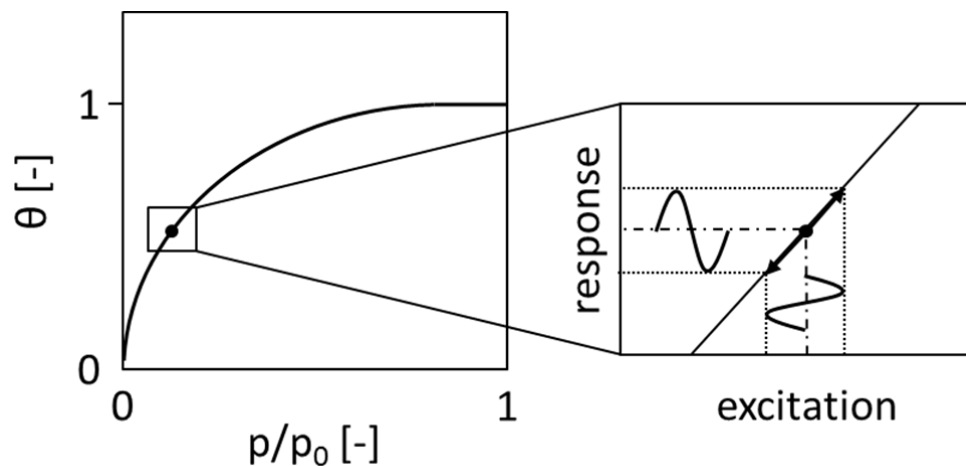
Figure 17: Sketch illustrating the system response to a pressure excitation in a typical pressure modulation frequency response experiment.

In a typical experiment the pressure response to a periodic volume perturbation is measured as a function of the excitation frequency. Thereby, the amplitude of the perturbation has to be kept as small as possible to eliminate the non-linearity arising from the adsorption isotherm as well as heat effects. A compromise between a sufficiently good signal to noise ratio and preferably small amplitude is a perturbation by $\Delta V = \pm 1\%$. Prior to the measurement the sample is equilibrated with the sorbate at a defined pressure, which is another crucial parameter of the experiment. The pressure has to be chosen as low as possible in order to guarantee coverages within the linear part of the adsorption isotherm.

The first step of the data analysis is a Fourier transformation resulting the phase and the amplitude. Thereby, a phase shift and a change in amplitude are observed in comparison to the empty system (blank). A feasible mathematical description was developed by Yasuda et al. [97] by solving the mass balance for a batch adsorber. Thus, two characteristic functions, the so called in and out of phase functions are derived:

$$\frac{A_B}{A} * \cos(\varphi - \varphi_B) - 1 = \sum_1^n K_{FR,n}\, \delta_n^{in} \tag{2.4.5}$$

$$\frac{A_B}{A} * \sin(\varphi - \varphi_B) - 1 = \sum_1^n K_{FR,n}\, \delta_n^{out} \tag{2.4.6}$$

$$K_{FR} = \frac{RT}{V_{FR}} * \left(\frac{d\theta}{d\left(\frac{p}{p_0}\right)}\right) \tag{2.4.7}$$

Where A is the pressure amplitude of the experiment, A_B is the corresponding pressure amplitude in a blank experiment, φ is the phase of the experiment, φ_B is the phase of the blank measurement and δ is the characteristic function. Herein, n is the number of parallel transport processes. Furthermore K_{FR} is a parameter proportional the slope of the adsorption isotherm, the temperature (T), the volume of the system (V_{FR}) and the gas constant (R).

Blank experiments are needed to account for non-idealities of the system itself. The characteristic functions (δ) are solutions of the Fick's second law using appropriate boundary conditions. The simplest model system is an infinite plain sheet. The corresponding mass balance is:

$$\frac{\partial}{\partial t}\left(\frac{p(t)V_{FR}(t)}{RT_0}\right) + \frac{\partial B}{\partial t} = 0 \tag{2.4.8}$$

where p is the pressure in the system, T_0 is the experimental temperature and B is the amount of gas present in the sheet. Assuming the volume is changed sinusoidal we can define the time dependent volume by Eq. 2.4.9:

$$V_{FR}(t) = V_{FR,eq} * (1 - A * \exp(i\omega t)) \tag{2.4.9}$$

herein $V_{FR,eq}$ is the equilibrium volume, ω is the frequency of perturbation and t is the time. Correspondingly, the vapor pressure of the diffusing substance and the concentration in the pores can be described by Eq. 2.4.10 and 2.4.11, respectively:

$$p(t) = p_e * \left[1 + P * exp(i * (\omega t + \phi)) \right] \tag{2.4.10}$$

$$c = c_e * [1 + A_c * \exp(i * (\omega t + \phi - \chi)] \tag{2.4.11}$$

where p_e is the partial pressure of the diffusion component in the gas phase at equilibrium condition, c_e is the equilibrium concentration inside the particle, P ($\Delta p/$ 2) and A_c are the amplitudes, ϕ and χ are the phase lags of the vapor pressure and the internal concentration, respectively. Both, amplitudes and phase lags depend on the excitation frequency ω.

The diffusion inside the pores is described by Fick's second law (Eq. 2.3.5). In here, the assumption of a concentration independent diffusion coefficient is fulfilled due to the small change of surface concentration during the experiment. In this work we consider the case of one dimensional diffusion in sheet with plane boundaries at $x = 0$ and $x = l$. The boundary conditions define the concentration at the external surface to be proportional to the sinusoidal changing vapor pressure in the gas phase [134]:

$$c = c_e \qquad t < 0; \ 0 \leq x \leq l \tag{2.4.12}$$

$$c = \sin(\omega t + \varphi) \qquad t > 0; x = 0, l \tag{2.4.13}$$

Under these boundary conditions the amount of gas present in the sheet can be expressed by Eq. 2.4.15:

$$B = B_e + A * \exp(i * (\omega t + \phi + \psi)) \tag{2.4.15}$$

where B_e is equilibrium amount of gas present within the sheet. The amplitude A and the phase lag ψ are given by Eq. 2.4.16 and 2.4.17, respectively.

$$A = \frac{\sqrt{2} * K_H * p * (sin^2(2\eta_1) + sinh^2(2\eta_1))^{1/2}}{2\eta_1 * (\cos(2\eta_1) + \cosh(2\eta_1))} \tag{2.4.16}$$

$$\psi = tan^{-1} \left[\frac{(\sin(\eta_1) - \sinh(\eta_1))}{(\sin(\eta_1) + \sinh(\eta_1))} \right] \tag{2.4.17}$$

In here, η_1 is described by Eq. 2.4.18:

$$\eta_1 = \left(\frac{\omega l^2}{2D}\right)^{1/2} \tag{2.4.18}$$

where l is the diffusional path length. Substituting Eqs. 2.4.15-2.4.18 into the material balance leads to Eqs. 2.4.5 and 2.4.6 where the characteristic in and out of phase functions are defined by:

$$\delta_{in} = \delta_{1c} = \frac{1}{\eta_1} * \left[\frac{(\sinh(\eta_1) + \sin(\eta_1))}{(\cosh(\eta_1) + \cos(\eta_1))} \right] \qquad (2.4.19)$$

$$\delta_{out} = \delta_{1s} = \frac{1}{\eta_1} * \left[\frac{(\sinh(\eta_1) - \sin(\eta_1))}{(\cosh(\eta_1) + \cos(\eta_1))} \right] \qquad (2.4.20)$$

This model implies uniformly sized particles, which is hardly fulfilled in a real system. Thus the model needs to be refined using a Gaussian type particle size distribution. The modified characteristic function is expressed by [135]:

$$\bar{\delta}(\bar{l}) = \frac{1}{\sigma_G \sqrt{2\pi}} * \int_0^\infty \delta * \exp\left(-\frac{(l - \bar{l})^2}{2\sigma_G^2} \right) dl \qquad (2.4.21)$$

Herein $\bar{\delta}(\bar{l})$ and $\bar{l}$ are describing the mean values of the characteristic function and the thickness of the sheet, respectively.
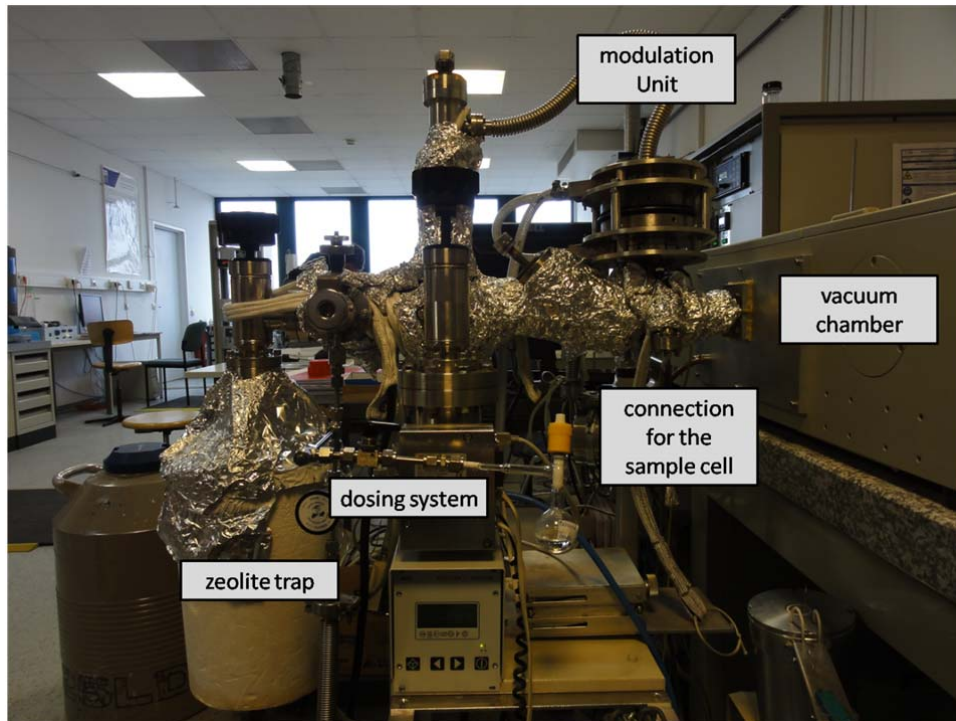
Figure 18: Setup for pressure modulation frequency response experiments

Experimental setup

An image of the experimental setup is presented in Figure 18. The sample is placed into a glass tube heated with a tailor made portable oven and connected to an UHV system. The UHV system is equipped with a turbo-molecular pump, (TMH 071-003, Pfeiffer Vacuum), a zeolite trap acting as a pre-pump, a separately pumped dosing system, and, most important, a pressure modulation unit.

The liquid or gaseous sorbates (aromatics, aliphatics) are connected to the dosing system via ¼" tube fitting. Additionally, a scroll pump (oil free) is connected in order to remove impurities from either the dosing line or the sorbate. The dosing line is connected to the UHV system via a full metal regulating valve UDV 040 (Pfeiffer Vacuum), which allows adjusting the sorbate partial pressure with a high accuracy.

The periodic volume perturbation is induced via a magnetically driven plate sealed with flexible UHV bellows. The metal plate is placed horizontally between the two electromagnets, which move the plate with a defined frequency (10^{-3}-2.5 Hz) controlled via a custom made HPVee program. The temperature of the magnets is maintained at 313 K using a cryostat. The pressure response is recorded via a Baratron pressure transducer (MKS 16A11TCC).

Sample preparation and experimental conditions

30 mg of powdered sample are dispersed on several layers of quartz wool to avoid bed depth effects. The sample is activated at 723K for 1 h with an incremental heating rate of 10 K/min in vacuum ($p < 10^{-4}$ Pa) to remove adsorbed water.

The sorbate is added with a partial pressure of 30 Pa until the adsorption equilibrium is fully established. During the experiment the volume of the setup is varied periodically with a square wave volume perturbation in a frequency range of 2.5 to 10^{-3} Hz and an amplitude of $\Delta V = \pm 1\%$.

The pressure response is Fourier transformed obtaining the amplitude and the phase lag. The resulting characteristic functions are fitted according to Eqs. 2.4.5, 2.4.6, 2.4.19, 2.4.20 and 2.4.21 by a nonlinear parameter fitting using a CMA evolutional strategy in MATLAB [136].

2.4.3 Fast time resolved infrared spectroscopy

Fast time resolved infrared spectroscopy was originally developed to investigate transport on the mesoscale [75, 137-139], similar to gravimetrical measurement of the uptake rates [93]. However, due to a time resolution of 600 ms the technique is not limited to slow transport processes as it is the case in the gravimetrical determination of uptake processes. A sketch illustrating the measurement procedure is presented in Figure 19.
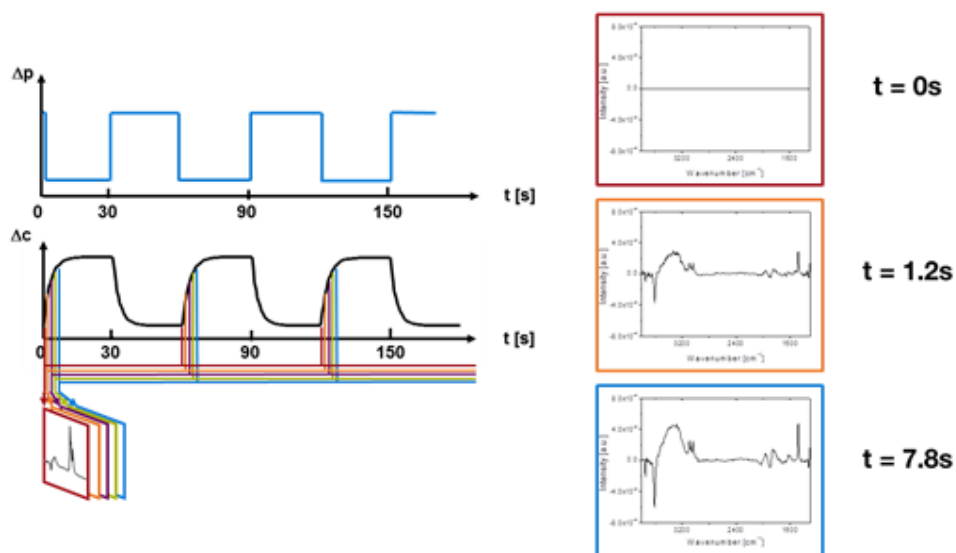
Figure 19: Sketch illustrating the experimental procedure of the fast time resolved infrared spectroscopy. A time resolution of 600 ms is obtained.
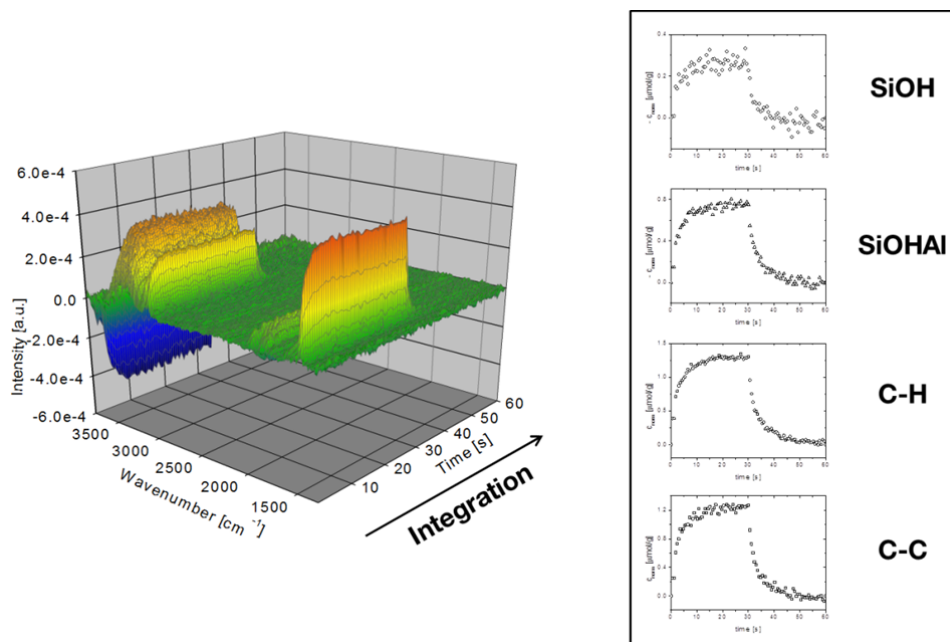
Figure 20: Sketch illustrating the extraction of individual concentration profiles from the experimentally obtained raw data

In order to achieve such a good time resolution the experiment is conducted in an infrared spectrometer operated in rapid scan mode and repeated several thousand times to obtain a reasonably good signal to noise ratio. Thus, the volume is perturbated using the same unit as described in the previous section which is able to

vary the system volume (and by this the pressure) by ±3-4%. A pressure increase leads to adsorption of sorbate molecules, whereas a decrease forces its desorption. The concentration profiles are obtained from integrating the characteristic bands of either the sorbate (CC and CH) or the sorbent (BAS and SiOH) as shown in Figure 20.

Originally, the transport processes were analyzed by extracting the initial sorption rates on either the terminal or bridging hydroxyl groups. Thus, the individual sorption kinetics were obtained from fitting the concentration profiles according to a first order kinetic expressed by Eqs. 2.4.22-2.4.24 [75, 138, 139]:

Adsorption: $\quad \Delta c(t) = \Delta c_{eq} * \left(1 - \exp\left(-\frac{t}{\tau_{ad}}\right)\right) \forall\ 0 < t < t_p/2$ (2.4.22)

Desorption: $\quad \Delta c(t) = \Delta c_{eq} * \left(\exp\left(-\frac{t-t_p/2}{\tau_{de}}\right)\right) \forall\ t_p/2 < t < t_p$ (2.4.23)

Initial rate: $\quad r_{ini} = \frac{d\Delta c(t)}{dt} = \frac{1}{\tau_{ad}} * \Delta c_{eq} * \exp\left(-\frac{t}{\tau_{ad}}\right) = \frac{\Delta c_{eq}}{\tau_{ad}} for\ t < \tau_{ad}$

(2.4.24)

In here, $\Delta c(t)$ represents the concentration profile, Δc_{eq} is the equilibrium concentration change upon pressure perturbation, t_p is the time interval of one adsorption/desorption cycle (typically 60 s), r_{ini} is the initial sorption rate and τ_{ad} and τ_{ad} are the time constants of diffusion for the ad- and desorption, respectively.

In this thesis, a new approach of directly accessing the internal and external concentration profiles is presented. This becomes possible by utilizing the difference in molar extinction coefficients at the external surface and within the zeolitic channel system. The intensity change in each spectrum collected in the series of time resolved spectra during the pressure modulation can be described for the CH-stretching or bending vibration by Eqs. 2.4.25 and 2.4.26:

$$\Delta I(t)_{CH-stretch} = \left(\varepsilon_{SiO_2, CH-stretch} * \Delta c(t)_{ext} + \varepsilon_{ZSM-5, CH-stretch} * \Delta c(t)_{int}\right) *$$
$$\frac{m_{wafer}}{\pi r_w{}^2} \text{ (2.4.25)}$$

$$\Delta I(t)_{CH-bend} = (\varepsilon_{SiO_2, CH-bend} * \Delta c(t)_{ext} + \varepsilon_{ZSM-5, CH-Bend} * \Delta c(t)_{int}) * \frac{m_{wafer}}{\pi r_w{}^2}$$

(2.4.26)

With $\Delta I(t)_{CH-stretch}$ and $\Delta I(t)_{CH-bend}$ being the change in intensities of the IR-bands obtained from integration the IR-spectrum at the corresponding wavenumbers, ε is the respective extinction coefficient, m_{wafer} is the weight of the IR wafer, r_w is the radius of the IR wafer, $\Delta c(t)_{int}$ is the concentration change of the sorbate within

the zeolite channel system and $\Delta c(t)_{ext}$ is the concentration change of the molecules adsorbed at the external surface of the zeolite particle. Eqs. 2.4.25 and 2.4.26 can be solved analytically resulting $\Delta c(t)_{int}$ and $\Delta c(t)_{ext}$ given by Eqs. 2.4.27 and 2.4.28:

$$\Delta c(t)_{ext} = \frac{\left(\Delta I_{CH-bend} - \Delta I_{CH-stretch} * \frac{\varepsilon_{ZSM-5,CH-Bend}}{\varepsilon_{ZSM-5,CH-Stretch}}\right) * \frac{\pi r_w^2}{m_{wafer}}}{\varepsilon_{SiO_2,CH-Bend} - \frac{\varepsilon_{ZSM-5,CH-Bend} * \varepsilon_{SiO_2,CH-Stretch}}{\varepsilon_{ZSM-5,CH-Stretch}}} \tag{2.4.27}$$

$$\Delta c(t)_{int} = \frac{\left(\Delta I_{CH-bend} * \frac{\pi r_w^2}{m_{wafer}} - \varepsilon_{SiO_2,CH-Bend} * \Delta c_{ext}\right)}{\varepsilon_{ZSM-5,CH-Bend}} \tag{2.4.28}$$

The profiles of $\Delta c(t)_{int}$ and $\Delta c(t)_{ext}$ can be obtained applying Eqs. 2.4.27 and 2.4.28 to each data point within a series of time resolved IR spectra collected during a periodic pressure modulation. Moreover, this technique is applicable to both, in single components and co-adsorption experiment.

Single components

The concentration profiles $\Delta c(t)_{int}$ and $\Delta c(t)_{ext}$ are modeled by a set of equations describing the uptake onto the external surface (including a pre-adsorbed state), the pore entrance step and the diffusion inside the micropores which allows extracting all individual rates and rate constants within the transport network. The uptake onto the external surface and the pore entrance step are described by first order kinetic processes:

$$\Delta c_{ext}(t) = (1 - exp(-k_{ads} * t)) * \Delta c_{ext,eq} \tag{2.4.29}$$

$$\Delta c_{ext}(t) = a * exp(-k_{pe} * t) \tag{2.4.30}$$

Where k_{ads} is the rate constant of the adsorption at the external surface, k_{pe} is the rate constant of transport from the external surface into the micropore and a is an additional factor describing the amount of molecules being in the pre-adsorbed state. By merging Eqs. 2.4.29 and 2.4.30 the concentration change on the external surface can be obtained:

$$\Delta c_{ext}(t) = \left[(1 - exp(-k_{ads} * t)) * \Delta c_{ext,eq}\right]$$
$$+ \left[a * \Delta c_{ext,eq} * exp(-k_{pe} * t) * (1 - exp(-k_{ads} * t))\right] \tag{2.4.31}$$

The concentration change within the zeolitic micropores is modeled by the uptake kinetics of a sorbate into a microporous solid at isothermal conditions as described by Crank [118] for small concentration changes (constant D) by:

$$\Delta c(t)_{int} = \left(1 - \sum_1^n \frac{6}{\pi^2 n^2} * exp\left(-\frac{n^2 \pi^2 D_{app} t}{L^2}\right)\right) * \Delta c_{int,eq} \tag{2.4.32}$$

Both concentration profiles as well as their sums for either the CH-stretching or bending vibrations were fitted using Eqs. 2.4.31 and 2.4.32. The Arrhenius law was used in order to keep the amount of parameters as low as possible. By this means the activation energy of diffusion and the corresponding pre-exponential factor (Eq. 2.4.33) were used as variables:

$$D_{app} = D_{0,app} * exp\left(\frac{E_{A,D_{app}}}{RT}\right) \tag{2.4.33}$$

Multi components

The description of the transport process during the co-adsorption of two or more sorbates is more complex as also the molecular interactions inside the zeolitic micropores must be taken into account. The model used within this study is based on the Stefan-Maxwell formalism. For the sake of completeness the complete solution for the given problem is presented, although it is based on earlier work [107, 119]. However, some additions and changes were made. The approach proposes that transport inside the zeolitic micropore takes place exclusively via surface diffusion. Hence, the vacant site is treated as the (n+1)th component in the mixture. Correspondingly, the general solution for the diffusion of a multicomponent mixture in a microporous system is given by:

$$-\frac{\theta_i}{RT}\nabla\mu_i = \sum_{\substack{j=1 \\ j\neq i}}^{n+1} \frac{\theta_j N_i - \theta_i N_j}{n_t^S \mathbb{D}_{ij}} \tag{2.4.34}$$

The surface coverage of component i can be defined by:

$$\theta_i = \frac{n_i^S}{n_t^S} \tag{2.4.35}$$

where n_i^S is the adsorbed amount of component i and n_t^S is the sum of diffusing components including the vacant sites. The overall sorption site coverage (θ_t) can be obtained from the sum of sorbate surface occupation or from the amount of vacant sites(θ_V):

$$\theta_t = \sum_{i=1}^{n} \theta_i = 1 - \theta_V \tag{2.4.36}$$

Moreover, the total molar flux and the velocity of the (n+1)th species is zero:

$$N_t = \sum_{j=1}^{n+1} N_j = \sum_{j=1}^{n} N_j = 0 \tag{2.4.37}$$

and Eq. 2.4.34 eases to:

$$-\frac{\theta_i}{RT}\nabla\mu_i = \sum_{\substack{j=1 \\ j\neq i}}^{n} \frac{\theta_j N_i - \theta_i N_j}{n_t^S \mathbb{D}_{ij}} + \frac{\theta_{n+1} N_i}{n_t^S \mathbb{D}_{i,n+1}} \tag{2.4.38}$$

With the definition of the single component Maxwell-Stefan diffusion coefficient:

$$\mathbb{D}_{iV} = \frac{\mathbb{D}_{i,n+1}}{\theta_{n+1}} \tag{2.4.39}$$

Eq. 2.4.38 yields:

$$-\frac{\theta_i}{RT}\nabla\mu_i = \sum_{\substack{j=1 \\ j\neq i}}^{n}\frac{\theta_j N_i - \theta_i N_j}{n_t^s \mathbb{D}_{ij}} + \frac{N_i}{n_t^s \mathbb{D}_{iV}} \tag{2.4.40}$$

Under the assumption of an equilibrium between the surface and the bulk fluid phase the chemical potential μ_i can be expressed via the chemical potential in a standard state μ_i^0 and fluid phase fugacity of species i (f_i):

$$\mu_i = \mu_i^0 + RTln(f_i) \tag{2.4.41}$$

The fluid phase fugacity itself is given by the partial pressure (p_i) and the fugacity coefficient (φ_i):

$$f_i = p_i\varphi_i \tag{2.4.42}$$

For moderate system pressures the fugacity coefficient approaches unity and the fluid phase fugacity is equal to the partial pressure. A suitable expression for the left side of Eq. 2.4.34 can be found applying Eqs. 2.4.41 and 2.4.42:

$$\frac{\theta_i}{RT}\nabla\mu_i = \frac{\theta_i}{RT}\sum_{j=1}^{n}\frac{\delta\mu_i}{\delta\theta_j}\nabla\theta_j \tag{2.4.43}$$

With:

$$\frac{\delta\mu_i}{\delta\ln(f_i)} = \frac{\delta\mu_i}{\delta\ln(p_i)} = RT \tag{2.4.44}$$

the final expression is obtained:

$$\frac{\theta_i}{RT}\sum_{j=1}^{n}\frac{\delta\mu_i}{\delta\theta_j}\nabla\theta_j = \theta_i\frac{\delta\ln(p_i)}{\delta\mu_i}\sum_{j=1}^{n}\frac{\delta\mu_i}{\delta\theta_j}\nabla\theta_j = \theta_i\sum_{j=1}^{n}\frac{\delta\ln(p_i)}{\delta\theta_j}\nabla\theta_j = \sum_{i=1}^{n}\Gamma_{ij}\nabla\theta_j \tag{2.4.45}$$

where Γ_{ij} is the thermodynamic correction factor and is defined by:

$$\Gamma_{ij} = \theta_i\frac{\delta\ln(p_i)}{\delta\theta_j} \tag{2.4.46}$$

As the examined systems (aromatics and aliphatics adsorbed in zeolites) show Langmuir type adsorption isotherms the surface coverage θ_i can be expressed in terms of p_i:

$$\theta_i = \frac{K_i p_i}{1+\sum_{j=1}^{n}K_j p_j} \tag{2.4.47}$$

and

$$K_i p_i = \frac{\theta_i}{\theta_V} \tag{2.4.48}$$

The matrix elements of $[\Gamma]$ are:

$$\Gamma_{ij} = \delta_{ij} + \frac{\theta_i}{\theta_V} \tag{2.4.49}$$

Eq. 2.4.40 can be expressed in terms of an n-dimensional matrix expression by using Eqs. 2.4.46-2.4.49:

$$n_t^s [\Gamma](\nabla\theta) = [B](N) \tag{2.4.50}$$

with matrix elements of [B] are defined by:

$$B_{ii} = \frac{1}{\mathbb{D}_{iV}} + \sum_{\substack{J=1 \\ j \neq i}}^{n} \frac{\theta_j}{\mathbb{D}_{ij}} \tag{2.4.51}$$

$$B_{ij} = -\frac{\theta_j}{\mathbb{D}_{ij}} \tag{2.4.52}$$

Thus, the vector of the molar fluxes is:

$$(N) = -n_t^s [B]^{-1}[\Gamma](\nabla\theta) \tag{2.4.53}$$

where the matrix of Fick diffusivities [D] is defined by:

$$[D] = [B]^{-1}[\Gamma] \tag{2.4.54}$$

A general solution for the effective Fick diffusivity in binary mixtures including molecule-molecule interactions is shown in Eqs. 2.4.55-2.4.57 [140-142]:

$$D_i = -\frac{N_i}{n_t^s \nabla\theta_i} \tag{2.4.55}$$

$$D_1 = \frac{\mathbb{D}_{1V}}{1-\theta_1-\theta_2}[(1-\theta_2)|\nabla\theta_1| + \theta_1|\nabla\theta_2|] \tag{2.4.56}$$

$$D_2 = \frac{\mathbb{D}_{2V}}{1-\theta_1-\theta_2}[(1-\theta_1)|\nabla\theta_2| + \theta_2|\nabla\theta_1|] \tag{2.4.57}$$

For the description of uptake profiles determined by fast time resolved infrared spectroscopy Eq. 2.4.58 needs to be solved:

$$\frac{\delta\theta_i}{\delta t} = \nabla(D_i\nabla\theta_i) \qquad i = 1,2 \tag{2.4.58}$$

The corresponding solution is the multicomponent equivalent Eq. 2.4.34:

$$(\theta(t) - \theta_0) = \left[[I] - \sum_{n=1}^{\infty} \frac{6}{n^2\pi^2} \exp(\frac{-n^2\pi^2 [D]t}{L^2}) \right] * [\theta_{sat} - \theta_0] \tag{2.4.59}$$

The elements of matrix $[B]^{-1}$ are given by:

$$\mathcal{D}_{11} = \frac{\mathbb{D}_{1V}*[\theta_1\mathbb{D}_{2V}+(1-\theta_1)\mathbb{D}_{12}]}{\theta_1\mathbb{D}_{2V}+\theta_2\mathbb{D}_{1V}+\theta_V\mathbb{D}_{12}} \tag{2.4.60}$$

$$\mathcal{D}_{12} = \frac{\theta_1\mathbb{D}_{2V}(\mathbb{D}_{1V}-\mathbb{D}_{12})}{\theta_1\mathbb{D}_{2V}+\theta_2\mathbb{D}_{1V}+\theta_V\mathbb{D}_{12}} \tag{2.4.61}$$

$$\mathcal{D}_{21} = \frac{\theta_2\mathbb{D}_{1V}(\mathbb{D}_{2V}-\mathbb{D}_{12})}{\theta_1\mathbb{D}_{2V}+\theta_2\mathbb{D}_{1V}+\theta_V\mathbb{D}_{12}} \tag{2.4.62}$$

$$\mathcal{D}_{22} = \frac{\mathbb{D}_{2V}*[\theta_2\mathbb{D}_{1V}+(1-\theta_2)\mathbb{D}_{12}]}{\theta_1\mathbb{D}_{2V}+\theta_2\mathbb{D}_{1V}+\theta_V\mathbb{D}_{12}} \tag{2.4.63}$$

In here, the single component Maxwell-Stefan diffusivities ($\mathbb{D}_{1V}, \mathbb{D}_{2V}$) are calculated from the corresponding single component Fick diffusivities:

$$\mathbb{D}_{iV} = \frac{D_i}{1-\theta_i} \tag{2.4.64}$$

The countersorption diffusivity $\mathbb{D}_{12}$ is calculated according to the Vignes relation [143]:

$$\mathbb{D}_{12} = \mathbb{D}_{21} = \mathbb{D}_{1V}^{\frac{\theta_1}{\theta_1+\theta_2}} * \mathbb{D}_{2V}^{\frac{\theta_2}{\theta_1+\theta_2}} \tag{2.4.65}$$

The elements of the matrix of thermodynamic correction factors [Γ] are:

$$\Gamma_{11} = 1 + \frac{\theta_1}{1-\theta_1-\theta_2} \tag{2.4.66}$$

$$\Gamma_{12} = \frac{\theta_1}{1-\theta_1-\theta_2} \tag{2.4.67}$$

$$\Gamma_{21} = \frac{\theta_2}{1-\theta_1-\theta_2} \tag{2.4.68}$$

$$\Gamma_{22} = 1 + \frac{\theta_2}{1-\theta_1-\theta_2} \tag{2.4.69}$$

The matrix of Fick diffusivities $[D]$ is obtained from Eq. 2.4.54. The resulting elements are:

$$D_{11} = \mathcal{D}_{11}\Gamma_{11} + \mathcal{D}_{12}\Gamma_{21} \tag{2.4.70}$$

$$D_{12} = \mathcal{D}_{11}\Gamma_{12} + \mathcal{D}_{12}\Gamma_{22} \tag{2.4.71}$$

$$D_{21} = \mathcal{D}_{21}\Gamma_{11} + \mathcal{D}_{22}\Gamma_{21} \tag{2.4.72}$$

$$D_{22} = \mathcal{D}_{21}\Gamma_{12} + \mathcal{D}_{22}\Gamma_{22} \tag{2.4.73}$$

For the solution of Eq. 2.4.59 the eigenvalues of the matrix of the Fick diffusivities are required:

$$\widehat{D}_{1,2} = \frac{D_{11}+D_{22}}{2} \pm \frac{D_{11}-D_{22}}{2}\left[\frac{1+4D_{12}D_{21}}{(D_{11}-D_{22})^2}\right]^{1/2} \tag{2.4.74}$$

$$\hat{f}_i = 1 - \frac{6}{\pi^2}\sum_{w=1}^{\infty}\frac{1}{w^2}\exp\left[-\frac{w^2\pi^2\widehat{D}_i t}{L^2}\right] \tag{2.4.75}$$

Taking Eq. 2.4.75 into account an analytical solution for Eq. 2.4.58 for the special case of the co-adsorption of two components is found:

$$[F] = \frac{\hat{f}_1}{\widehat{D}_1-\widehat{D}_2} * \left([D] - \widehat{D}_2[I]\right) + \frac{\hat{f}_2}{\widehat{D}_2-\widehat{D}_1} * \left([D] - \widehat{D}_1[I]\right) \tag{2.4.76}$$

$$\begin{pmatrix}\theta_1 - \theta_{1,0} \\ \theta_2 - \theta_{2,0}\end{pmatrix} = [F] * \begin{pmatrix}\theta_{1,sat} - \theta_{1,0} \\ \theta_{2,sat} - \theta_{2,0}\end{pmatrix} \tag{2.4.77}$$

The initial coverages of the diffusing molecules are determined from a competitive dual site Langmuir formalism (Eq. 2.2.15 and 2.2.16) [64]. The description of the mass transfer at the external surface (Δc_{ext}) follows Eq. 2.4.31 as the coverage at the outer surface is in the order of $\theta_{ext}=10^{-4}$ under the given conditions.

Experimental setup

The experimental system is an IR cell connected to a high vacuum system equipped with a gas dosing system and a pressure modulation unit identical the setup described 2.4.2. Thus a detailed description of the UHV system can be found in section 2.4.2. The IR cell itself consists of a gold ring sample holder whose temperature is regulated via a Eurotherm 2416 PID controller.

Sample preparation and experimental conditions

The zeolite samples are inserted as self-supporting wafers into the vacuum IR cell and subsequently activated below 10^{-5} Pa at 823 K for 1 h (heating rate of 10 K min^{-1}). Sorbate gas, i.e., n-butane, n-pentane or n-hexane, is added with partial pressure of 10 Pa at 343, 373 and 403 K. The sorbate partial pressure changes are followed by an in-line MKS Baratron (MKS 616A11) pressure transducer. A series of 100 IR spectra with time resolution of 600 ms is recorded during 400 modulation cycles.

   In order to obtain an acceptable signal to noise ratio, 400 adsorption-desorption cycles with a hundred spectra each cycle are recorded and the interferograms are co-added. Thus, each spectrum consists of 4000 co-added interferograms. Within a series of spectra, the last spectrum is subtracted to obtain intensity changes relative to the initial value. The concentration of the diffusing molecules within the sample is obtained from integration of the characteristic CH stretching and bending vibrations for light hydrocarbons as well as from the CH- and CC-stretching vibrational band of benzene molecules. The CH-stretching vibrations can be found between 3121-3006 cm^{-1} for benzene, 3045-2745 cm^{-1} for n-butane, 3020-2745 cm^{-1} for n-pentane and 3020-2740 cm^{-1} for n-hexane. The CC-vibrational band of benzene is located between 1530-1430 cm^{-1}. The CH-bending vibrations of the light hydrocarbons are present at similar wavenumbers, specifically at 1530-1406 cm^{-1}. Analyzing both the integral of CH-stretching and bending vibrational bands together allows transferring them into internal and external sorbate concentrations profiles separately according to Eqs. 2.4.27 and 2.4.28. This is not possible for benzene as the difference in extinction coefficient between the external surface and the micropores is too small. Hence, the benzene concentration is obtained from the integral of the CH- and CC-vibrations under the assumption of a constant extinction coefficient [75, 138].

   The individual intensity profiles of light hydrocarbons and benzene from the IR-band between 1530-1406 cm^{-1} are obtained by deconvolution with two defined peak

maxima. The peak maximum of the corresponding benzene band is located at 1479 cm^{-1} whereas those of n-butane, n-pentane and n-hexane are located at 1463 cm^{-1}.

The parameters $E_{A,D,app}$, $D_{0,app}$, k_{ads}, k_{pe} and a are obtained by nonlinear parameter fitting according to Eqs. 2.4.31 and 2.4.32 for the single component measurements and Eqs. 2.4.31 and 2.4.59 in co-adsorption experiments using a CMA evolutional strategy implemented in MATLAB [136].

2.4.4 Measurement of the uptake rates

Another common experiment for the determination of mesoscale transport rates is the determination of uptake rates. This can be performed either in batch adsorbers [93, 144] or under flow conditions [145]. Generally, the transport coefficients are extracted from the response curve to a step change in ambient concentration or partial pressure. The sorbate concentration within the sample can be monitored by gravimetric methods [93, 144] or infrared spectroscopy [145].

  In any case, the mathematical description is equal. As for ZLC the transport is described by Fick's second law (Eq. 2.3.5). The solution is given by Crank [118] under the following assumptions:

(1) The bed consists of uniformly shaped particles.
(2) The diffusion coefficient is not concentration dependent within the concentration range under investigation.
(3) The intracrystalline diffusion is the only limiting transport phenomenon.
(4) The adsorption isotherm is linear.
(5) Heat transfer is not influencing the transport.
(6) The bed behaves isothermal.

According to these assumptions the well-known expression for uptake curves is obtained [118]:

$$\frac{m(t)}{m_\infty} = 1 - \frac{6}{\pi^2} \sum_{n=1}^{\infty} \frac{1}{n^2} \exp\left(-\frac{n^2 \pi^2 D t}{R_p{}^2}\right) \tag{2.4.78}$$

Where $m(t)$ is the total amount of sorbate within the sample, m_∞ is the corresponding sorbate amount at the end of the experiment.

Experimental setup

Two separated setups, under static and under flow conditions are used. In here, the static system is a Seteram TG-DSC 111 microbalance (Figure 21) equipped with

quartz insertions and crucibles. The balance is connected to a UHV unit with a turbo-pump TMH 071-003 (Pfeiffer Vacuum), which is able to maintain 10^{-4} Pa. Additionally, an oil pump is connected to the system separately pumping the inlet system for the adsorbates. The pressure within the system is monitored via two MKS Baratron pressure transducers in the range from 10^{-2} Pa to atmospheric pressure.
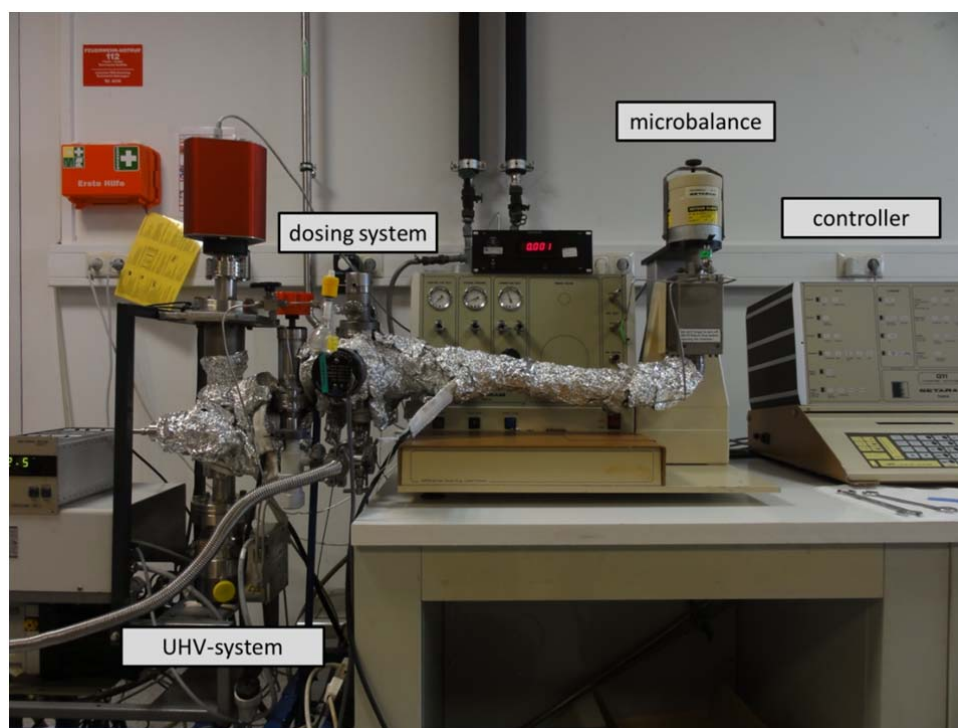
Figure 21: Microbalance connected to an UHV-system equipped with a dosing system, used for the determination of uptake rates and gravimetric adsorption isotherms.

The inlet system contains of a ¼ inch tube fitting where the sorbate flasks or gas bottles are connected to the system. The sorbate partial pressure is controlled via an all metal regulating valve UDV 040 (Pfeiffer Vacuum) connecting the inlet system to the vacuum unit.

The whole system is operated by a Seteram controller which is connected to a computer. A HP VEE based software is used to control the system and to track all relevant data, which is the mass, the pressure and the heat signal.

The flow system is an infrared flow cell built into a Nicolet 6700 IR spectrometer. An image of the setup is presented in Figure 22. The flow rates are controlled via 4 mass flow controllers (Bronkhorst EL-flow select). Saturation of the carrier gas with liquid sorbates is conducted via two custom build saturators (Figure 14) placed into a

cooling bath (15°C) to avoid sorbate condensation within the system. The temperature of the cell is controlled by an electronic PID controller (Eurotherm 2404).
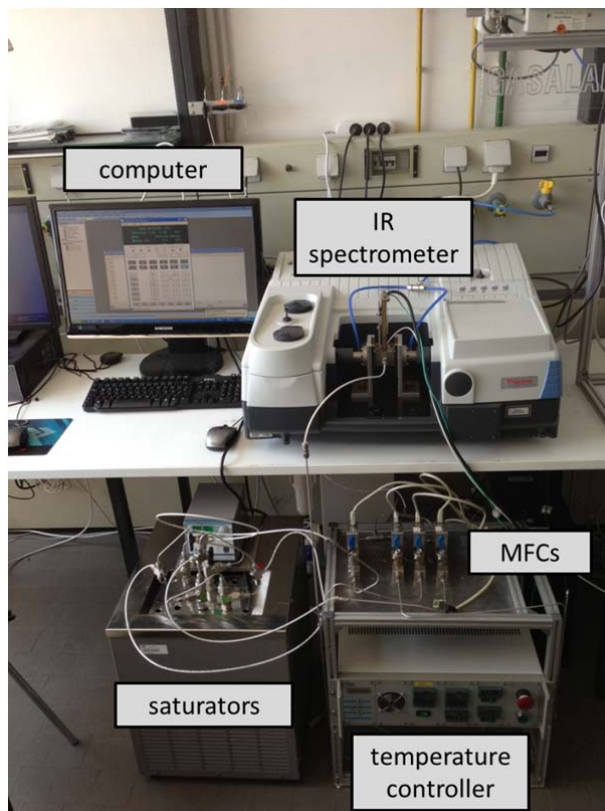
Figure 22: Nicolet 6700 infrared spectrometer equipped with a flow cell applied for uptake rate measurements. The temperature and the flow rates are controlled via a PID controller and four mass flow controllers, respectively. Saturation of the carrier gas with liquid sorbates is conducted via custom made saturators.

Sample preparation and experimental conditions

For gravimetric experiments 20-30 mg of the powdered sample is filled into the quartz crucible, subsequently inserted into the system and activated in vacuum (>10^{-2} Pa) at 723 K for 1 h and an incremental heating rate of 10 K/min. The adsorbate is added at 343, 373 and 403K stepwise with partial pressures of 10, 100, 200 and 1000 Pa, which are kept constant through over the whole experiment. In a typical IR uptake experiment the sample is prepared as a self-supporting wafer and the experiments are carried out in continuous flow mode with a volumetric flow rate of 125 ml/min. The sample is activated at 723 K for 1h and incremental heating rate of 10 K/min in helium flow. A second helium stream of 125 ml/min is saturated with the liquid sorbate. The sorbate concentration is kept low (around 30-70 Pa) to stay in the

Henry regime of the adsorption isotherm. The uptake rate measurement is initialized a step change in partial pressure of the diffusing substance.

The IR spectra are collected with a resolution of 4 cm^{-1} and a time resolution of 10-60 s. The spectra are normalized to the integral of the overtone lattice band between 2105 and 1740 cm^{-1} of the activated H-ZSM5 sample and processed by integrating the characteristic bands of the sorbate.

In both methods the obtained raw data is normalized to the steady state uptake obtained at the end of the experiment and analyzed according to the model presented in Eq. (2.4.78). A parameter fit using a CMA evolutional strategy implemented in MATLAB [136] is performed.

Chapter 3

Molecular understanding of sorption in mesoscale organized zeolites with MFI structure

Abstract

We report herein the adsorption of light hydrocarbons in small crystal ZSM-5 monitored by infrared spectroscopy including a direct monitoring of the individual concentrations (surface and intracrystalline). Accessing the individual rates reveals that the sorption enhancement upon surface modification with TEOS is selective towards molecules with a small steric demand and a high heat of adsorption within the silica overlayer.

3.1. *Introduction*

Medium pore zeolites, such as ZSM-5 (MFI structure) [146] are a key catalyst component in petroleum and petrochemical processes [1, 6, 26], including toluene alkylation [12, 13, 15, 16] and xylene isomerization [5-9]. In addition to high acid strength and thermal stability they act as shape selective catalysts, showing a clear preference for forming products that do not exceed a certain size, by exerting steric constraints on the formation and transport of molecules. This induced selectivity, however, comes with the price of a reduced utilization of the zeolite material through

diffusional constraints. Thus, understanding and controlling sorption and transport properties of reactants and products is essential to rationally develop and fully utilize the shape selective potential of zeolites.

Previously, we have had identified five key steps in the transport of molecules through a zeolite particle [75, 138], forming a complex network [147] of consecutive steps as presented in Figure 23. It involves the collision of a gas phase molecule (Figure 23a) with the external surface, in which the sorbate molecule has a certain probability to be adsorbed into a weakly bound physisorbed state (Figure 23b) with a high two-dimensional mobility [75]. This step is followed by the adsorption at terminal hydroxyl groups (Figure 23c) at the external surface or the adsorption on bridging hydroxyl groups inside the pores (Figure 23d). The latter two steps occur in parallel. The transport inside the micropores proceeds via hopping mechanism between adsorption sites [148, 149] and can be predicted with reasonable accuracy via MD simulations [85, 86, 148].
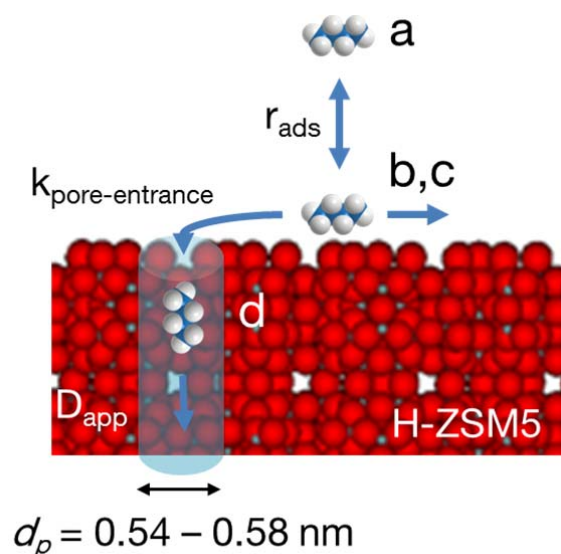
Figure 23: Proposed model describing the transport during the sorption of a light hydrocarbon molecule from the gas phase (a) to the adsorption site within the zeolite micropore including the equilibration of the sorbate with the external surface, the adsorption into a weakly bound pre-adsorbed state (b), at terminal hydroxyl groups (c) and transport to an internal site (d). Moreover, the decisive parameters for corresponding transport steps (r_{ads}, $k_{pore-entrance}$, D_{app}) are given.

A quantitative description of the transport rate, however, that includes the surface processes has not been accessible. Assessing individually the concentration of adsorbed molecules on the outer surface (in the weakly adsorbed mobile state) and

inside the microporous channels (on the bridging hydroxyl groups) is a key step towards a quantitative prediction of the complete transport network. By this means, a direct assessment of the transport processes allowing a selective sorption enhancement/retardation upon post-synthetic surface modification [75, 137, 138, 150, 151] would be feasible. Despite significant efforts, direct monitoring of the physisorbed molecules on the surface was hitherto not successful because of the very low concentration of these weakly adsorbed species and the resulting difficulty to differentiate the molecules from those adsorbed on bridging hydroxyl groups. Data presented herein now directly prove the existence of the previously postulated [75, 138, 139] physisorbed state and reveal that it is indeed an intermediate during the sorption of hydrocarbons into microporous solids.

Kinetic modeling applying the proposed model (Figure 23) provides the possibility to quantify the key parameters responsible for the increase in sorption rate after modifying the external surface with a mesoporous overlayer [75, 138]. It proves that especially for nano-sized zeolite particles the overall sorption rate is determined both by the sticking coefficient at the external surface and the pore entrance probability.

3.2. *Experimental*

3.2.1 Materials

Nano sized HZSM-5 was provided by Clariant AG with Si/Al = 45 (determined by AAS). According to SEM and TEM images shown in Figure 24 the material is best described as agglomerates of nano-sized primary particle (50-100 nm) forming secondary particles with a diameter of 0.5 μm. Concentrations of terminal and bridging hydroxyls determined by 1H MAS NMR spectroscopy were 0.27 and 0.21 mmol/g, respectively [75]. Post-synthetic surface modification by chemical liquid deposition of tetraethyl-orthosilicate was performed according to Zheng et al [150, 151], which creates a mesoporous silica overlayer with a pore size of 1.5 nm and an average thickness of approximately 3 nm according to TEM images (Figure 24). In the resulting zeolite, denoted modified, the concentration of terminal and bridging hydroxyl groups was 0.12 and 0.16 mmol g^{-1}, respectively.

Transmission electron microscopy was performed using a JEOL-2011 electron microscope operating at 200 kV. Nitrogen physisorption isotherms were measured using a PMI automated sorptometer at liquid nitrogen temperature (77 K) after

outgassing in vacuum for at least 6 h. BET [152] surface area was calculated between $p/p_0 = 0.03$-0.15. Micro-, meso-, and macropore volumes were evaluated using α_s [73] relative plot with nonporous hydroxylated silica [153] as reference material. A summary of the physisorption analysis for both samples is given in Table 2.

Table 2: Structural properties of the parent and the modified ZSM-5

Sample	S_{BET} [$m^2\ g^{-1}$]	V_{micro} [$cm^3\ g^{-1}$]	V_{meso} [$cm^3\ g^{-1}$]	V_{total} [$cm^3\ g^{-1}$]
Parent	423	0.121	0.017	0.364
Modified	383	0.113	0.031	0.322
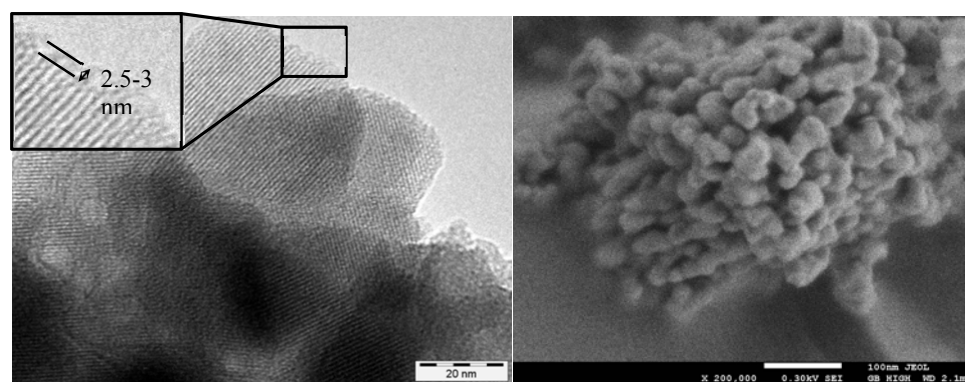
Figure 24: Typical SEM (right) image of the parent sample showing secondary, corny flower structured particles consisting of 50-100 nm large primary subunits with interstitial mesopores. According to TEM (left) a silica overlayer with an average thickness of 2.5-3 nm appears upon post-synthetic hydrolysis of tetraethyl-orthosilicate.

3.2.2 Fast-time resolved IR spectroscopy

Fast time resolved IR spectroscopy was performed on a Bruker IFS 66 v/s spectrometer in rapid scan mode. The powdered samples were pressed into self-supporting wafers (20 mg cm^{-2}) and inserted into the IR cell connected to an UHV system. The samples were activated under vacuum ($<10^{-7}$ mbar) at 823 K for 1h with an incremental heating rate of 10 K/min and subsequently equilibrated with the sorbate at 0.1 mbar. Square wave volume perturbation of ±5% using a magnetically driven plate was synchronized with the IR spectrometer. A more detailed description of the measurement setup and underlying principle can be found in section 2.4.3 information and also elsewhere [138, 147].

3.2.3 Determination of molar extinction coefficients

Molar extinction coefficients were determined for n-butane, n-pentane and n-hexane according to the procedure described by Emeis [154] in the range of the CH-stretching (3045-2745 cm^{-1}) and bending (1506-1406 cm^{-1}) vibration. Gravimetric adsorption isotherms were determined in a Seteram TGA-DSC 111 microbalance attached to a UHV system. 20 mg of sample were placed into a quartz sample holder and activated at 823 K for 1 h. The equilibration with the sorbate was performed in small pressure steps from 3x10^{-2} to 13 mbar in case of the zeolite and from 3x10^{-2} to 150 mbar for the silicon dioxide. Identical isotherm measurements between 3x10^{-3} and 1.2 mbar were performed in the described infrared spectrometer using identical preparation and activation procedure as described earlier. Molar extinction coefficients were obtained by plotting the gravimetric uptake against the integral of either the CH-stretching or bending vibrational band at constant pressure.

3.3. *Results and Discussion*

The transport process was followed by fast time resolved infrared spectroscopy during a stepwise pressure modulation. A typical example of resulting intensity profiles is presented in Figure 25. Please note that the intensity profiles are the sum of the sorbate concentration inside the pores and on the outer surface of the sample as shown in Eqs. (4.3.1) and (4.3.2). In contrast to previous studies with aromatic molecules and hexane isomers [75, 94, 138, 139, 147, 155], the intensity of the CH stretching vibrations reaches a higher value immediately after the pressure has been increased than under equilibrium conditions. Such a change has been shown to be very reproducible, but appears highly unlikely from the point of a first-principles analysis. Thus, a detailed analysis of the internal and external concentration profiles has been conducted, which is used to analyze the dynamics of the process

Parallel monitoring of the concentration inside the pores and on the surface requires the deconvolution of integrated intensity into concentration profiles characteristic for molecules present at the external surface and inside the zeolite micropores. The intensity profiles for the CH stretching and CH bending vibrations can be described by Eq. (3.3.1) and (4.3.2), respectively:

$$\Delta I_{CH-S}(t) = \left(\varepsilon_{SiO_2, CH-S} * \Delta c_{ext}(t) + \varepsilon_{ZSM-5, CH-S} * \Delta c_{int}(t) \right) \qquad (3.3.1)$$

$$\Delta I_{CH-B}(t) = \left(\varepsilon_{SiO_2, CH-B} * \Delta c_{ext}(t) + \varepsilon_{ZSM-5, CH-B} * \Delta c_{int}(t) \right) \qquad (3.3.2)$$

Here, $\Delta I_{CH-S}(t)$ and $\Delta I_{CH-B}(t)$ are denoting the intensity profiles of the CH-stretching and CH-bending vibrations, respectively, $\Delta c_{ext}(t)$ and $\Delta c_{int}(t)$ are the concentration profiles of the molecules at the external surface and inside the micropores, with $\varepsilon_{SiO_2, CH-S}$, $\varepsilon_{SiO_2, CH-B}$, $\varepsilon_{ZSM-5, CH-S}$, $\varepsilon_{ZSM-5, CH-B}$ being the molar extinction coefficients for the molecules adsorbed on SiO_2 and in ZSM-5. According to Eqs. (3.3.1) and (3.3.2), the deconvolution is only possible, if the ratio between the extinction coefficients for the bending and stretching vibrations of the molecules adsorbed on the external surface and inside the pores is sufficiently different, which is the case for the linear alkanes reported here, but -for example- not for aromatic molecules.

The extinction coefficients of the CH stretching and CH bending vibrations of n-butane, n-pentane and n-hexane were determined for ZSM-5 and fumed silica, the latter serving as model for the external surface of the zeolite and the siliceous overlayer (Table 3). The difference between the extinction coefficients in the CH-stretching and bending vibrations is larger for SiO_2 compared to ZSM-5, fulfilling the prerequisite to differentiate between the individual contributions.

The concentration profiles for n-butane adsorbed on the external surface and inside the pores in the parent sample from 343 to 403 K are shown in Figure 25. The change in concentration upon pressure modulation (0.1 ± 0.05 mbar) was at least two orders of magnitude higher for the molecules adsorbed inside the pores compared with the external surface, which is in line with the equilibrium constants observed [75]. The adsorption enthalpies and entropies from gravimetric adsorption isotherms at the external surface and at adsorption sites within the microporous channels are compared in Table 4. The variations in the concentration of the molecules inside the pores followed Fick's law, leading to an exponential increase in the coverage with time. In contrast, the concentration of the external surface showed a distinct maximum, which is attributed to the corresponding pressure gradient in the reactor system (Figure 25). The small volume perturbation induces a pressure increase, which leads to the increase in the sorbate uptake analyzed in this work. As the change in pressure is significantly faster than the uptake into the pores, the pressure will increase first to a value related to the compression of the volume and will decrease subsequently due to

the adsorption of molecules at the internal adsorption sites of the sample. As the equilibration of the external surface with the gas phase is faster than the rate of entering the pores, the surface concentration is in "quasi-equilibrium" with the gas phase and, thus, follows the pressure change. In turn, the rate of decrease in the surface concentration has to be equal to the rate of molecules entering the pores. Thus, all kinetic parameters of the proposed transport network (Figure 23) including the adsorption rate (r_{ads}) into a weakly bound surface state, the rate constant of the pore entrance ($k_{pore-entrance}$) and the apparent diffusion coefficient (D_{app}) can be obtained from the network of the rate equations given in the supplementary (results see Table 5).

The probability of pore entering, characterized by the rate constant of pore entrance ($k_{pore-entrance}$), decreases with chain length due to steric constraints [122]. On the other hand, the sticking probability, which is directly proportional to the adsorption rate (r_{Ads}) [139] increases in the order n-butane < n-pentane < n-hexane. Thus, the concentration of molecules in the pre-adsorbed state, determined by the difference between the rates of sorption and of pore entering increased with the chain length of the alkane.

Table 3: Molar extinction coefficients of n-butane, n-pentane and n-hexane in ZSM-5 and fumed silica at 343, 373 and 403 K

	T [K]	$\varepsilon_{ZSM-5, CH-S}$ [cm µmol^{-1}]	$\varepsilon_{ZSM-5, CH-B}$ [cm µmol^{-1}]	$\varepsilon_{SiO_2, CH-S}$ [cm µmol^{-1}]	$\varepsilon_{SiO_2, CH-B}$ [cm µmol^{-1}]
n-Butane	343	16.7	1.2	81.3	0.7
	373	22.9	1.8	102.9	0.7
	403	24.5	1.8	131.1	0.7
n-Pentane	343	15.0	1.1	35.0	0.5
	373	22.3	1.6	39.9	1.0
	403	39.9	2.8	48.5	1.1
n-Hexane	343	15.0	1.0	18.9	0.5
	373	10.3	0.7	24.9	0.3
	403	17.5	1.1	28.9	0.3

Table 4: Heats and entropies of adsorption at external and internal adsorption sites within ZSM-5 for n-Butane, n-Pentane and n-Hexane

	$\Delta H_{ads,external}$ [kJ mol^{-1}]	$\Delta S_{ads,external}$ [J mol^{-1} K^{-1}]	$\Delta H_{ads,internal}$ [kJ mol^{-1}]	$\Delta S_{ads,internal}$ [J mol^{-1} K^{-1}]
n-Butane	-13.5	-52	-51.0	-108
n-Pentane	-15.0	-44	-63.0	-126
n-Hexane	-19.5	-48	-72.0	-121

These findings enable the conclusive elucidation of the change in overall transport rates upon surface modification [75, 137, 138]. Figure 26 compares the adsorption and pore entrance rates of parent and the surface modified materials. It is observed that the adsorption rate increases (Figure 26) which can be accounted to an increased sticking probability at the external surface [75]. In parallel, the concentration change at the external surface increases due to stronger interaction of the sorbed molecules with the mesoporous overlayer. Thus, on the one hand the adsorption rate is increased due to an entropic and an enthalpic contribution, in which the rate constant is increased due to the entropy based funneling effect. On the other hand, the rate increases because of the higher concentration of molecules being adsorbed caused by a higher heat of adsorption in the mesopores than on the unmodified external surface [156].

Table 5: Change of external ($\Delta c_{eq.ext}$) concentration after the pressure increase, adsorption rate (r_{Ads}), rate and rate constant of pore entrance ($r_{pore\ entrance}$, $k_{pore\ entrance}$) and apparent diffusion coefficient (D_{app}) compiled for the parent and modified ZSM-5

		$\Delta c_{eq.ext}$ [$\mu mol\ g^{-1}$]	r_{Ads} [$\mu mol\ g^{-1}\ s^{-1}$]	$k_{pore\ entrance}$ [s^{-1}]	$r_{pore-entrance}$ [$\mu mol\ g^{-1}\ s^{-1}$]	D_{app} [$m^2 s^{-1}$]
parent	Butane	2.4×10^{-4}	2.7×10^{-4}	0.2	4.5×10^{-5}	3.8×10^{-14}
	Pentane	8.1×10^{-4}	5.1×10^{-4}	0.16	1.2×10^{-4}	1.4×10^{-14}
	Hexane	1.8×10^{-3}	1.0×10^{-3}	-	-	1.4×10^{-14}
modified	Butane	3.1×10^{-4}	3.7×10^{-4}	0.08	2.6×10^{-5}	2.5×10^{-14}
	Pentane	7.0×10^{-3}	5.3×10^{-3}	0.05	3.5×10^{-4}	1.2×10^{-14}
	Hexane	9.0×10^{-2}	5.6×10^{-2}	0.03	3.5×10^{-3}	1.7×10^{-14}
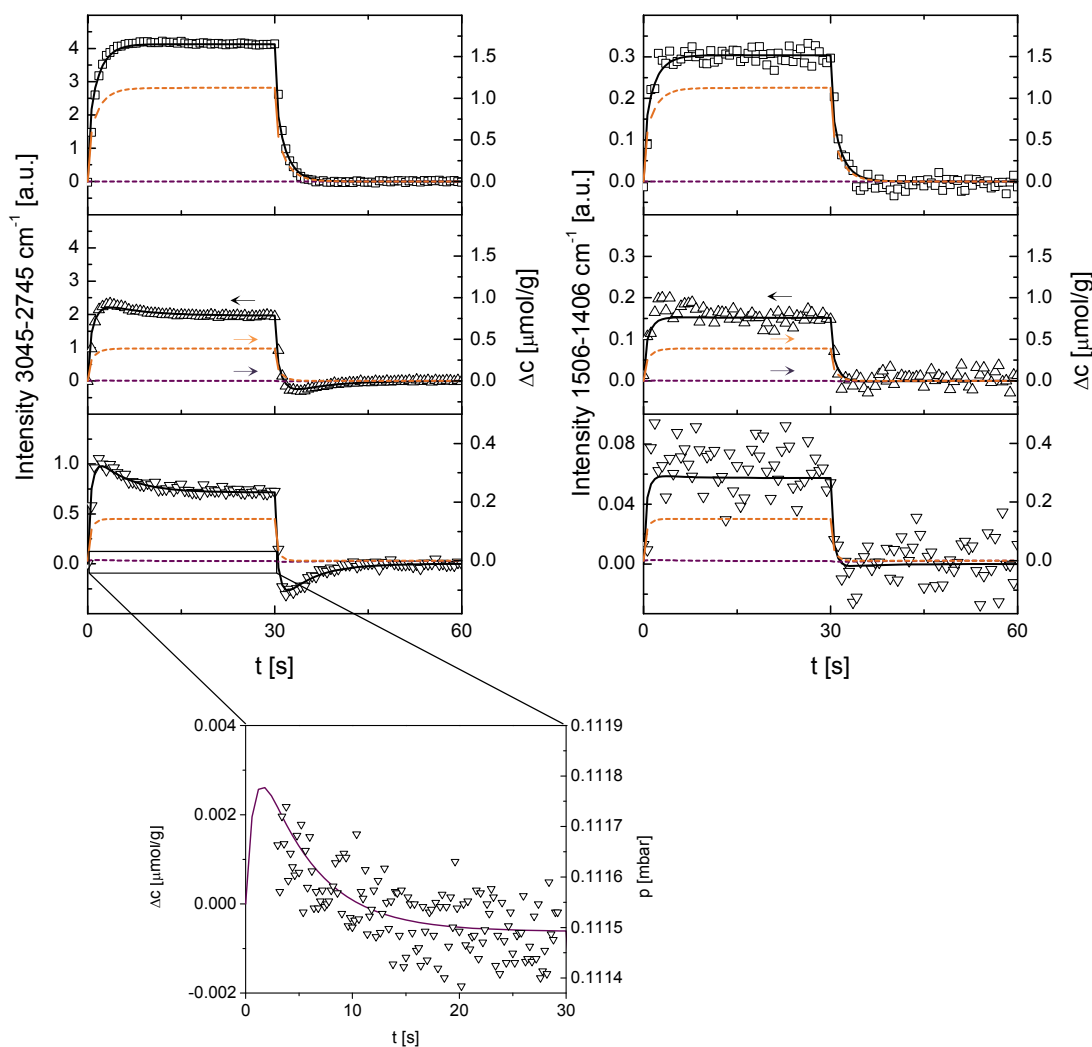
Figure 25: Intensity (left axis) for the CH-stretching (left) and bending (right) vibrations and the by deconvolution obtained internal (orange) and external (magenta) concentration profiles (right axis) of n-butane in H-ZSM5 at 343 (□), 373 (△) and 403 K (▽) during a periodic volume perturbation around 0.1 mbar.

However, the modification of the external surface also blocks a fraction of pore entrances or narrows them, statistically reducing the probability of pore entering. This blockage is overcompensated (Figure 26) for heavier compounds, i.e., hexane and benzene resulting in an increase in sorption rate [75, 137, 138]. On the other hand compensation is not possible for light (lower heat of adsorption) or sterically more demanding molecules (reduced pore entering probability) resulting in a reduction of the overall uptake rate (Table 5).
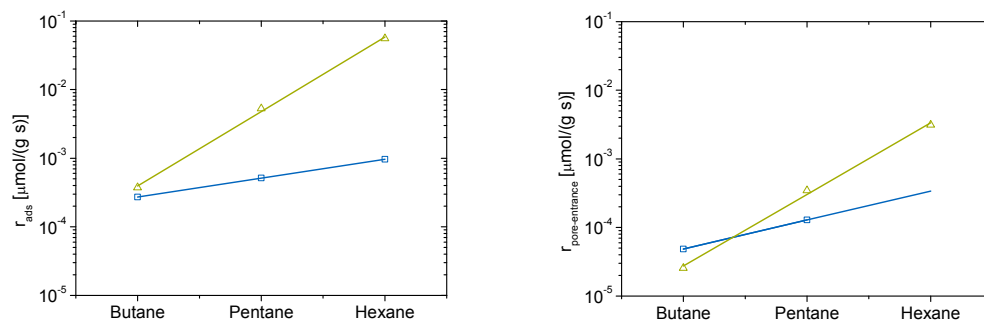
Figure 26: Trends of rate of adsorption (left) and pore entrance (right) at 403 K for n-butane, n-pentane and n-hexane in parent (△) and surface modified (○) ZSM-5.

As catalysis occurs exclusively in the micropores, let us discuss at this point the concentration profiles of molecules sorbed in the micropores. Figure 25 shows that it exhibits a pure exponential behavior, thus, fulfilling Fick's law. The effective diffusion coefficients in the parent material decrease in the order n-butane > n-pentane = n-hexane whereas the absolute numbers are two to four orders of magnitude smaller compared to previous studies [157-159], revealing the strong influence of the pore entrance on the overall transport network in such nano-crystals [90, 94]. SiO_2 deposition at the external surface influences the overall effective diffusion coefficients by modulating the pore entrance step significantly. It selectifies the rate of adsorption towards molecules with a high heat of adsorption on silica and low steric constraints.

In the current study the effective diffusivity of n-hexane is slightly increased, whereas it is decreased for n-butane. The effective diffusivities decrease in the order n-butane > n-hexane > n-pentane upon post-synthetic modification exemplifying the ability of selective tailoring of the transport of hydrocarbons. Despite the strong effects observed by modifying the molecular sieve, the activation energies of diffusion are identical to those obtained with large crystals [95]. As in such large crystals the pore transport is dominating [94], we conclude that a rate determining step of transport does not exist and that the intracrystalline diffusion is one of the kinetically relevant steps in the overall process.

3.4.   *Conclusions*

We show for the first time experimentally that the postulated surface intermediate exists during sorption into microporous materials such as ZSM-5. It is an important intermediate, whose steady state concentration determines the uptake into the zeolite.

Direct monitoring of the dynamic concentration changes of molecules on the zeolite surface was possible for crystal sizes where the pore entrance is a kinetically relevant step. This allows to determine the individual rates of the elementary transport steps and to identify the role of the initial collision of the molecules with the surface on the transport process.

The deconvolution was possible, because the accurate determination of molar extinction coefficients of molecules in environments experiencing different steric constraints allowed to quantitatively assess local concentrations. The physisorbed surface state is kinetically described as an intermediate step during the adsorption of light hydrocarbon molecule in ZSM-5 and the concentrations at the surface state matches excellently to the overall transport model postulated earlier for aromatic molecules (Figure 23).

The approach describes quantitatively the individual concentrations and rates during the sorbate uptake and was applied to understand the complex transport phenomena on hierarchical zeolite materials, especially after modifying the surface properties. It is shown conclusively that a mesoporous silica layer increases the steric demand by narrowing and blocking pores and increase the adsorption equilibrium constant due to higher heat of adsorption compared to the plain surface. Thus, the key parameters of the pore entrance step identified herein are the sticking coefficient and the heat of adsorption of the sorbate at the external surface and its statistical pore entering probability, which is proportional to its steric constraints. By this means molecules with a high heat of adsorption on silica and a low steric demand are adsorbed preferentially.

Chapter 4

Diffusion of mixtures of light alkanes and benzene in nano-sized H-ZSM5

This chapter was submitted for publication in the Journal of Physical Chemistry C as research article:

Diffusion of mixtures of light alkanes and benzene in nano-sized H-ZSM5

R. Kolvenbach, L. F. Gonzalez-Peña, A. Jentys, J. A. Lercher

Abstract

The joint transport of linear C4-C6 alkanes and benzene has been studied over nano-sized H-ZSM5 crystals by fast-time resolved infrared spectroscopy. The internal and external concentration profiles during the co-adsorption of alkanes and aromatics were directly monitored for a zeolite in which transport is controlled by the pore entrance step. The detailed kinetic analysis revealed a decrease in the adsorption and pore entrance rates of light hydrocarbon molecules upon addition of benzene by about 10-30%. This was caused by both a reduction in the rate constants and in the coverage at the external surface. On the other hand the apparent diffusion coefficient of benzene decreased up to 80% in comparison to the pure component. This decrease is attributed to a competitive adsorption at sites near the pore mouth. The extent increased with decreasing chain length of the co-sorbed alkane, which corresponds to a simultaneous decrease in occupation of pore mouth sites by light hydrocarbons.

4.1. *Introduction*

The understanding of transport phenomena of aromatic/alkane mixtures in zeolites has been an important research topic since several decades [99, 102, 104-108, 110].

Although all key parameters for the transport have been identified, the prediction of transport properties for new materials has not been possible so far, but would be of high importance for a rational design of shape-selective catalysts (e.g., for selective toluene alkylation) [12, 13, 15, 16].

It has been established that the adsorption of hydrocarbons on sites located in the pores of microporous materials proceeds via a network of three consecutive steps: (i) the collision and adsorption at the external surface, (ii) the subsequent pore entrance and (iii) finally the transport within the zeolitic micropores [75, 94, 137, 138]. However, only the total concentration of the molecules on the zeolite could be determined, while a differentiation between the concentrations at the external surface and inside the zeolite framework was experimentally not accessible, which did not allow the differentiation between the individual rates of the three transport steps [94].

The diffusion of mixtures containing benzene and aliphatic or aromatic co-sorbates in microporous materials has been studied extensively by numerous methods including permeation experiments [99, 101, 102], pulsed-field gradient nuclear magnetic resonance (PFG-NMR) [103-105], quasi-elastic neutron scattering (QENS) [83] and infrared spectroscopy [106] as well as by theoretical studies [64, 107-111]. Karge reported diffusivities of benzene as a single component, as well as during co-adsorption and counter diffusion of benzene with ethyl benzene in large-crystal H-ZSM5 examined via IR spectroscopy during uptake experiments in a flow system [106]. The study indicated a decrease of the benzene diffusivity of up to 60% in a mixture with ethyl benzene compared to the single component diffusion. These findings are supported by molecular dynamic simulations suggesting a blockage of the channel intersections by slowly diffusing substances, e.g., benzene, thus, reducing the transport rate of the second sorbate to almost zero [110]. This suggests that the intersections of ZSM-5 are the bottlenecks in the transport of linear C_1-C_6 alkanes in the presence of more strongly adsorbing molecules.

Surprisingly, the role of the crystal domains and their boundaries on the overall transport rate has only been phenomenologically explored [90]. All published work assumes a negligible effect of the surface barriers, although, it was suggested by several studies that the external surface affects the transport network [80]. The importance of such surface processes increases with decreasing particle size. Especially for nano sized zeolite crystals with extremely short diffusion path length the pore entrance step begins to dominate [90, 94].

We have recently reported a method based on differences in the molar extinction coefficients, which allows to differentiate between concentrations on the external surface and in the zeolite pores in small crystal H-ZSM5 using fast-time resolved IR spectroscopy [160]. It allows the direct monitoring of the concentration of the highly mobile pre-adsorbed surface states proposed for aromatic molecules [160] and the extraction of the transport parameters. The current study aims on investigating the multicomponent sorption/transport of aromatic and alkanes sketching a generic scenario for the understanding of (multicomponent) transport networks in microporous materials on the particle level.

4.2. *Theoretical Section*

In a typical fast time resolved IR experiment a small amount of one or more substances is equilibrated with the sorbent at a defined pressure prior to the measurement. Subsequently, the system is exposed to a near equilibrium pressure perturbation with a constant frequency (0.166 Hz) and amplitude (±5%). The change in pressure causes variations of the periodic adsorption and desorption rates of the sorbate, which are followed via the concentrations of adsorbed species by fast-time resolved infrared spectroscopy.

We have recently reported a method for the deconvolution of the resulting intensity profiles into concentration profiles on the internal and external surface of the crystals [160] utilizing the differences in the extinction coefficients of light hydrocarbons at the external surface and inside the channel system (Eqs. 3.3.1, 3.3.2) [160]

The corresponding extinction coefficients are presented in Table 3. Solving the system of equations given by Eqs. (3.3.1, 3.3.2) results in the concentration profiles of internally and externally sorbed molecules [160]:

$$\Delta c_{ext} = \frac{\left(\Delta I_{CH-bend} - \Delta I_{CH-stretch} * \frac{\varepsilon_{ZSM-5,CH-Bend}}{\varepsilon_{ZSM-5,CH-Stretch}}\right) * \frac{\pi r_w^2}{m_{wafer}}}{\varepsilon_{SiO_2,CH-Bend} - \frac{\varepsilon_{ZSM-5,CH-Bend} * \varepsilon_{SiO_2,CH-Stretch}}{\varepsilon_{ZSM-5,CH-Stretch}}} \tag{4.2.1}$$

$$\Delta c_{int} = \frac{\left(\Delta I_{CH-bend} * \frac{\pi r_w^2}{m_{wafer}} - \varepsilon_{SiO_2,CH-Bend} * \Delta c_{ext}\right)}{\varepsilon_{ZSM-5,CH-Bend}} \tag{4.2.2}$$
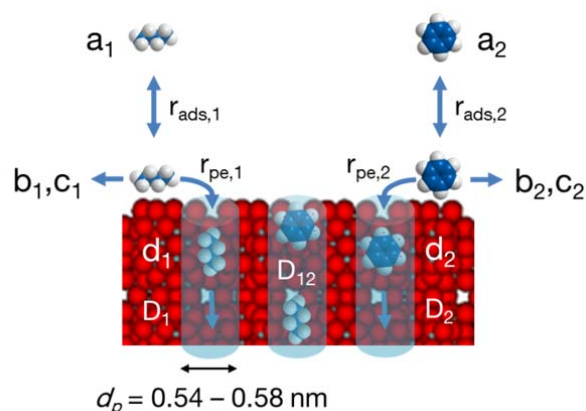
Figure 27: Proposed transport model for the sorption of an aliphatic (1) or aromatic (2) molecule from the gas phase (a_1, a_2) to an adsorption site within the zeolite channel system (d_1, d_2). It includes the adsorption into a weakly bound physisorbed state (b_1, b_2) and equilibration with the external surface site (c_1, c_2) with the rate r_{ads}, the rate of the pore entrance r_{pe} as well as the intracrystalline diffusion characterized by the corresponding diffusion coefficients D_1 and D_2. In the case of a co-adsorption of two components the intracrystalline transport is additionally determined by the counter-sorption diffusivity $D_{1,2}$.

The proposed transport network for the adsorption of hydrocarbons is schematically represented in Figure 27, where the transport is described by a complex, interconnected network. It involves the collision of the gas phase molecules (a_1, a_2) with external surface having a certain probability to be sorbed into a weakly bound, highly mobile pre-adsorbed state (b_1, b_2). From there, the molecule can either be transferred to a terminal hydroxyl group (c_1, c_2) at the external surface or to a bridging hydroxyl in the pore mouth, which is followed by intraparticle diffusion (d_1, d_2).

Table 6: Thermodynamic adsorption data used for the determination of the initial loading in a periodic volume perturbation experiment for n-butane, n-pentane and n-hexane [160] as well as for benzene [161]

	$\Delta H_{Ads,1}$ [kJmol^{-1}]	$\Delta H_{Ads,2}$ [kJmol^{-1}]	$\Delta S_{Ads,1}$ [Jmol^{-1}K^{-1}]	$\Delta S_{Ads,2}$ [Jmol^{-1}K^{-1}]	$\Phi_{max,1}$ [mmolg^{-1}]	$\Phi_{max,2}$ [mmolg^{-1}]
Butane	-64	-28	-144	-33	0.98	0.23
Pentane	-62	-63	-127	-109	0.87	0.39
Hexane	-79	-70	-174	-113	0.64	0.57
Benzene	-51	-	-60	-	0.67	-

Table 7: Adsorption equilibrium constants for n-butane, n-pentane, n-hexane and benzene determined from the adsorption equilibrium data [160], [161] used in the model to determine the initial concentration and the concentration change at internal sorption sites upon periodic volume perturbation.

	$K_{Ads,1,343K}$ [-]	$K_{Ads,1,373K}$ [-]	$K_{Ads,1,403K}$ [-]	$K_{Ads,2,343K}$ [-]	$K_{Ads,2,373K}$ [-]	$K_{Ads,2,403K}$ [-]
Butane	191	31	7	399	180	91
Pentane	552	97	22	7080	1210	268
Hexane	-	91	14	-	6660	1250
Benzene	42900	10200	2990	-	-	-

4.2.1 Single and dual component diffusion

The explicit algebraic expression for a binary mixture can be found in section 2.4.3 [107]. The initial coverages of the diffusing molecules are determined from a competitive dual site Langmuir formalism [64]. The necessary single component adsorption data were reported recently and are reviewed in Table 6, Table 7 [160, 161].

4.3. *Experimental*

4.3.1 Materials

Zeolite H-ZSM5 with a Si/Al ratio of 45 (determined by atomic absorption spectroscopy) was provided by Clariant AG. A concentration of 0.27 mmol g^{-1} terminal (SiOH) and 0.21 mmol g^{-1} bridging (SiOHAl) hydroxyl-groups were determined using ^{1}H-MAS NMR [138]. Benzene, n-pentane and n-hexane (Fluka, GC Standard, $\geq$ 99.8%) were used without further purification. n-Butane was obtained from Air Liquide (purity $\geq$ 99.0%).

4.3.2 Physicochemical Characterization

N_2 physisorption isotherms were recorded using a PMI automated sorptometer at 77 K after outgassing at 523 K for 2 h. The BET [152] surface area was determined in a relative pressures range of 0.03-0.15 mbar. Micro-, meso-, and macropore volumes were evaluated using a α_s relative plot [73] with nonporous hydroxylated SiO_2 [153] as reference material. The total pore volume was analyzed at $p/p_0 = 0.95$.

   Scanning electron micrographs were obtained from a REM JEOL 5900 LV microscope operated at 25 kV with resolution of 5.0 nm and magnification of 3×10^{-6}.

Transmission electron microscopy was performed using a JEOL-2011 electron microscope operating at 200 kV. Prior to the measurement the powdered sample was suspended in ethanol and dried on a copper-carbon grid.

A detailed description of the fast time resolved infrared spectroscopy set-up including the corresponding data treatment can be found in section 2.4.3

4.4. *Results*

4.4.1 Physicochemical Characterization

N_2 physisorption experiments resulted in a BET surface are of 423 m^2 g^{-1}, a micropore volume of 0.12 cm^3 g^{-1}, a mesopore volume of 0.017 cm^3 g^{-1}and a total pore volume of 0.36 cm^3 g^{-1} [75]. The large difference between the sum of the micro- and mesopore volume compared to the total pore volume indicates a large fraction of macroporosity within the sample presented in the SEM image (Figure 28a). It suggests that the zeolite particles were agglomerated generating larger moieties with meso- and macropores. The corresponding crystal size of the primary particles forming the agglomerates was 0.5 μm.
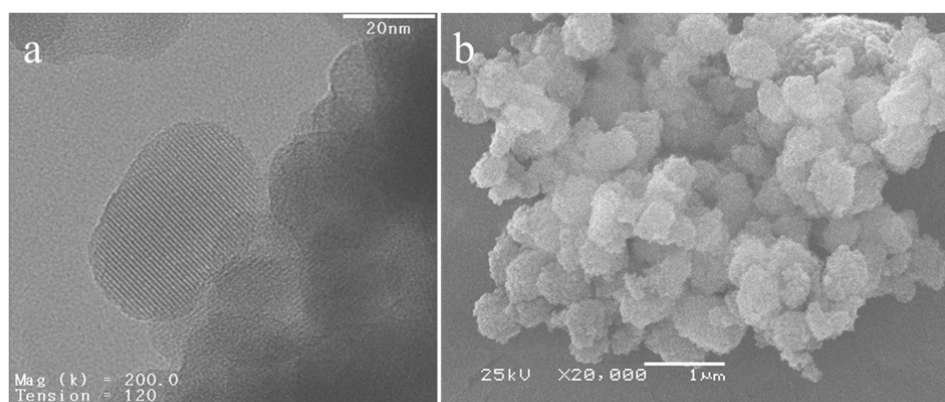
Figure 28 SEM (left) and TEM (right) images of the polycrystalline HZSM-5 sample.

Also the TEM image (Figure 28b) showed that the isolated particles observed by SEM were agglomerates of smaller subunits with a primary particle size of 50-100 nm. A more detailed description of the physiochemical characterization can be found in Ref. [139].

4.4.2 Fast time resolved IR spectroscopy

Single Component

The CH-stretching and deformation intensity profiles of n-butane during a volume perturbation experiment at 343, 373 and 403K are presented in Figure 29. The profile of the CH-stretching vibration exhibited an apparent overshooting immediately after the step wise pressure increase and re-equilibrated within 20 s, whereas the CH-deformation vibration followed the typical exponential increase. Moreover the apparent overshooting of the CH-stretching intensity profile increased from 343 to 403K significantly. In all cases, the second part of the intensity profile corresponding to a step down towards the initial pressure was a perfect mirror image of the previous uptake. The observed apparent overshooting appeared to be highly reproducible, but is in contrast to all previous studies with either BTX aromatics [75, 138, 139] or hexane isomers [137]. Thus, a more detailed analysis is necessary.
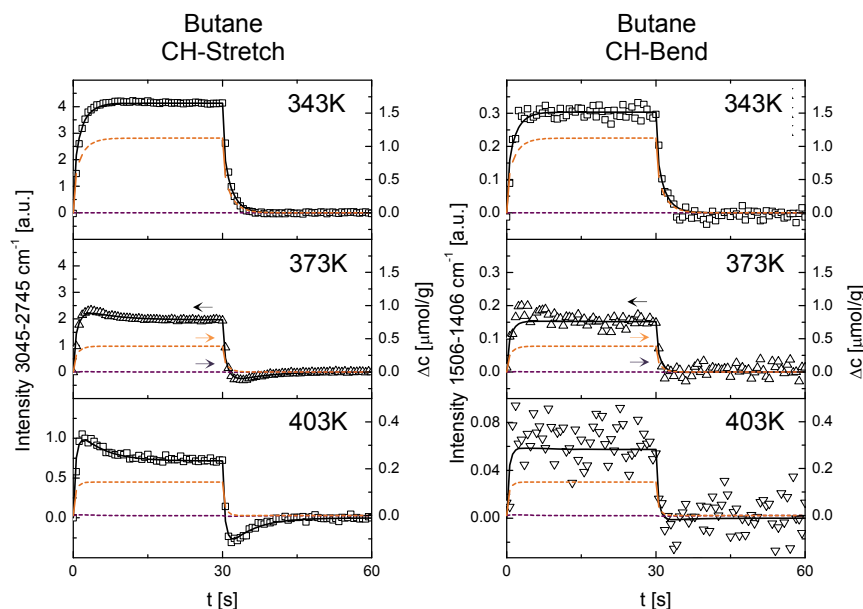
Figure 29 Intensity (black, left axis), internal (orange, right axis) and external concentration profiles (magenta, right axis) determined from the CH-stretching (left) and deformation (right) vibrational band of n-butane adsorbed on H-ZSM5 during a periodic volume perturbation around 0.1 mbar at 343, 373 and 403K.

Deconvolution according to Eqs. (4.2.1) and (4.2.2) revealed that the apparent overshooting was induced by the concentration at the external surface, which showed a steep increase caused by the fast equilibration with the gas phase followed by a

decrease parallel to the decreasing system pressure reflecting the uptake of molecules into the zeolite pores [160]. On the other hand, the internal concentration profile exhibited the typical exponential form [160].

The fact that the overall transport network with nanocrystalline ZSM5 is mainly controlled by the pore entrance step [94] opened up in the unique possibility of modeling the concentration profiles according to Eq. (2.4.31), which allowed to determine the rate for the adsorption at the external surface and for the pore entrance step (Table 8) as well as an apparent diffusion coefficient using Eq. (2.4.59). The latter can be understood as a measure for the overall (apparent) sorption rate. All results are summarized in Table 8.

It was found that the rate of adsorption (r_{ads}) at the external surface increased in the order n-butane<n-pentane<n-hexane. A similar trend was observed for the pore entrance where the rate (r_{pe}) increased in the order n-butane<n-pentane while it was not accessible for n-hexane due to the form of the concentration profile. Please note here that the corresponding rate constant of the pore entrance step (k_{pe}) decreased in the order n-butane>n-pentane.

Table 8: Rate constant of the adsorption at the external surface (kads), concentration change at the external surface upon periodic pressure perturbation ($\Delta c_{ext,eq}$), rate of adsorption at the external surface (r_{ads}), rate constant of the pore entrance (k_{pe}), rate of pore entrance (r_{pe}), apparent diffusion coefficient (D_{app}) as well as $D_{0,app}$ and activation energy of diffusion ($E_{A,D,app}$) of n-butane, n-pentane and n-hexane determined separately in H-ZSM5 at 343, 373 and 403K applying a periodic volume perturbation measurement.

	T [K]	$\Delta c_{ext,eq}$ x 10^4 [μmol g^{-1}]	k_{ads} [s^{-1}]	r_{ads} x10^4 [μmol g^{-1}s^{-1}]	k_{pe} [s^{-1}]	r_{pe} x10^5 [μmol g^{-1} s^{-1}]	D_{app} x10^{15} [m^{2}s^{-1}]	$D_{0,app}$ x10^{12} [m^{2}s^{-1}]	$E_{A,D,app}$ [kJmol^{-1}]
Butane	343	4.9	0.5	2.6	-	-	14.3		
	373	3.4	0.8	2.6	0.16	5.4	24.2	9.8	19
	403	2.4	1.1	2.7	0.2	4.8	37.9		
Pentane	343	17.6	0.4	6.9	-	-	4.9		
	373	11.7	0.5	5.6	-	-	8.8	7.7	21
	403	8.1	0.6	5.1	0.16	12.8	14.5		
Hexane	343	49.4	0.5	25.5	-	-	4.5		
	373	28.2	0.5	13.3	-	-	8.2	9.0	22
	403	17.9	0.5	9.7	-	-	13.9		

The apparent diffusion coefficients (D_{app}) obtained from the internal concentration profiles decreased in the order n-butane>n-pentane~n-hexane, which is in line with previous results while the absolute numbers were 2-4 orders of magnitude smaller than those obtained in large crystal material [157-159]. This was caused by the strong retardation of the transport at the crystal boundary on the overall apparent diffusion coefficients in nano-crystalline materials [90]. The corresponding activation energy of diffusion was 19 kJ/mol for n-butane, 21 kJ/mol n-pentane and 22 kJ/mol for n-hexane which is in perfect agreement to the literature [95].

The intensity and concentration profiles of benzene at temperatures between 343 and 403 K are compiled in Figure 30 and the results are summarized in Table 9. Both profiles followed an exponential uptake. In contrast to the light hydrocarbons, a deconvolution of the experimentally obtained intensity profile according to Eqs. (4.2.1) and (4.2.2) was impossible, as the difference in molar extinction coefficient was insufficient. Thus, the overall concentration profiles reflected the internal concentration as the corresponding internal site coverage exceeded the external surface coverage by 2-3 orders of magnitude (Table 7, Table 11). The obtained diffusion coefficients increased from 3×10^{-15} to 1.1×10^{-14} m^2 s^{-1} from 343 to 403K, which is in good agreement with previous studies [94]. The activation energy of diffusion was 27 kJ/mol being in line with earlier reported data [94, 95].

Table 9: Apparent diffusion coefficient (Dapp), $D_{0,app}$ and activation energy of diffusion ($E_{A,D,app}$) determined in H-ZSM5 using a periodic volume perturbation experiment at 343, 373 and 403 K.

	T [K]	$D_{app} \times 10^{15}$ [m^2 s^{-1}]	$D_{0,app} \times 10^{12}$ [m^2 s^{-1}]	$E_{A,D,app}$ [kJ mol^{-1}]
	343	2.8		
Benzene	373	5.9	36.9	27
	403	11.3		

Figure 30 Intensity (black, left axis) and overall concentration (orange, right axis) of benzene CC-stretching vibrational band adsorbed on H-ZSM5 obtained from a periodic volume perturbation experiments at 343, 373 and 403K.

Dual components mixtures

The intensity and concentration profiles of n-butane and benzene obtained in a 1/1 mixture at temperatures between 343 and 403 K are shown exemplary in Figure 31. The observed uptake curves were comparable to the corresponding single component measurements, however, the apparent overshooting effect for the light hydrocarbon intensity profiles increased significantly from single component to the experiments with mixtures. Moreover, the initial slopes in the concentration profiles of benzene were significantly reduced which points to a reduction of the corresponding apparent transport rates.

The rate of adsorption at the external surface (r_{ads}) and the rate of pore entrance (r_{pe}) of light alkanes in an equimolar mixture with benzene are compared to those obtained from single component measurements in Figure 32. It becomes apparent that both, the rate of adsorption and of pore entrance linearly increased with carbon number. Moreover a slight decrease in those rates was observed upon adding an equivalent concentration of benzene. The r_{Ads} was reduced by 10-30% and rate of pore entrance decreased by 7-20%. The differences in both parameters were getting less pronounced with increasing chain length. Unfortunately, the changes were too small to detect a significant change in the apparent diffusion coefficient, because the observed

differences were within the measurement inaccuracy (Figure 33). In contrast, the apparent diffusivity of benzene in such mixtures is reduced by about 75-80%, compared to the single component. The corresponding trend is presented in Figure 33. It is worth noting that the apparent activation energies of diffusion did not change from single components to mixtures.

In addition to the equimolar mixture, the transport parameters were also examined in a 3/1 mixture of n-butane with benzene. The results are presented in Table 10. A threefold higher adsorption rate and a more than fourfold higher pore entrance rate of n-butane were observed, whereas the differences in apparent diffusion were again within the measurement error. On the other hand the apparent diffusion coefficient of benzene decreased by more than 99%. The activation energies of both apparent diffusivities remained unchanged.
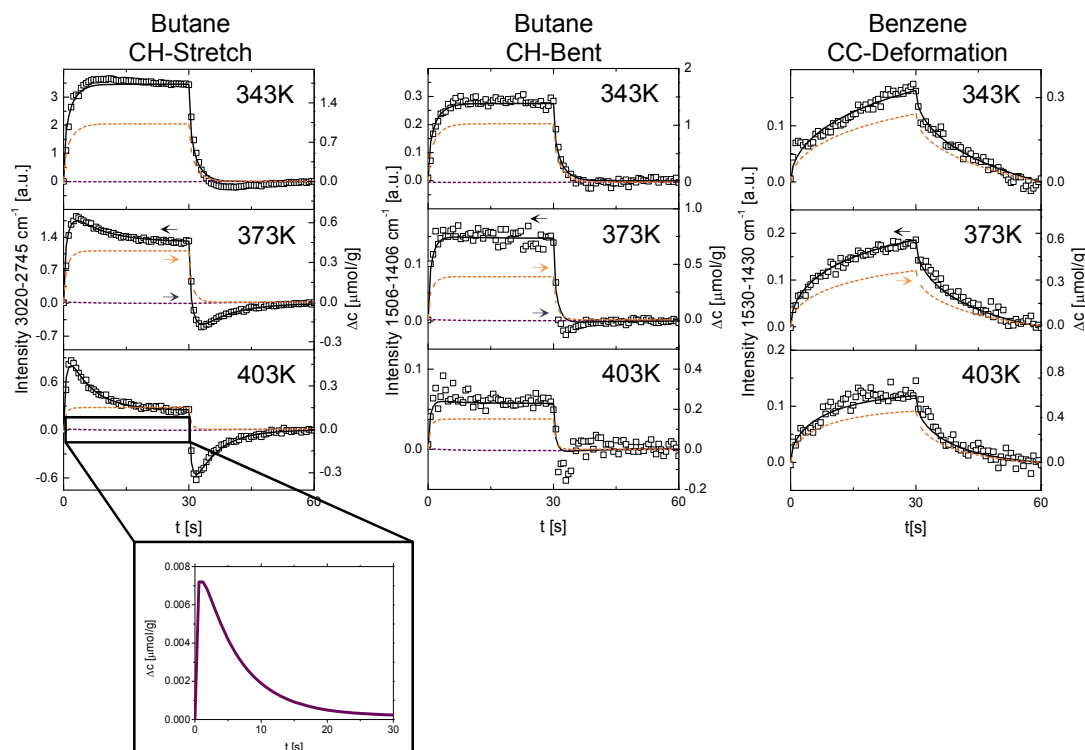
Figure 31 Intensity profile (black, left axis) for the CH-stretching (left) and deformation (middle) vibrational band and the by deconvolution obtained internal (orange, right axis) and external (magenta, right axis) concentration profiles of n-butane as well as the intensity profile (black, left axis) of the benzene CC-stretching vibrational band (right) and the corresponding concentration profile (orange, right axis) in an equimolar n-butane/benzene mixture adsorbed on H-ZSM5 at 343, 373 and 403 K during a periodic volume perturbation around 0.2 mbar.

Table 10: Rate constant of the adsorption at the external surface (k_{ads}), concentration change at the external surface upon periodic pressure perturbation ($\Delta c_{ext,eq}$), rate of adsorption at the external surface (r_{ads}), rate constant of the pore entrance (k_{pe}), rate of pore entrance (r_{pe}), apparent diffusion coefficient (D_{app}), $D_{0,app}$ and activation energy of diffusion ($E_{A,D,app}$) of n-butane, n-pentane and n-hexane as well as apparent diffusion coefficient (D_{app}), $D_{0,app}$ and activation energy of diffusion ($E_{A,D,app}$) of benzene. All parameters were determined in parallel using a volume perturbation experiments with bimolecular mixtures of benzene and either n-butane, n-pentane or n-hexane within H-ZSM5 at 343, 373 and 403K.

		Light hydrocarbon								Benzene		
	T [K]	$\Delta c_{ext,eq}$ x 10^4 [μmol g^{-1}]	k_{ads} [s^{-1}]	r_{ads} x10^4 [μmol g^{-1} s^{-1}]	k_{pe} [s^{-1}]	r_{pe} x10^5 [μmol g^{-1} s^{-1}]	D_{app} x10^{15} [m^2 s^{-1}]	$D_{0,app}$ x10^{12} [m^2 s^{-1}]	$E_{A,D,app}$ [kJ mol^{-1}]	D_{app} x10^{15} [m^2 s^{-1}]	$D_{0,app}$ x10^{12} [m^2 s^{-1}]	$E_{A,D,app}$ [kJ mol^{-1}]
Butane/	343	4.8	0.4	2.1	-	-	12.4			0.5		
Benzene	373	3.3	0.6	2.1	0.13	4.2	20.9	8.4	19	1.0	6.5	27
1/1	403	2.4	0.8	1.9	0.17	4.0	32.6			2.0		
Pentane/	343	17.6	0.4	7.5	-	-	6.1			0.7		
Benzene	373	11.5	0.5	6.3	0.08	9.6	10.9	9.5	21	1.5	9.2	27
1/1	403	8.1	0.7	5.8	0.15	11.8	18.1			2.8		
Hexane/	343			-	-	-	-	-	-	-	-	-
Benzene	373	27.8	0.4	11.6	-	-	6.0	6.6	22	1.4	8.9	27
1/1	403	17.4	0.4	7.8	-	-	10.1			2.7		
Butane/	343	14.3	0.4	6.4	-	-	9.3			9·10^{-3}		
Benzene	373	9.8	0.7	6.5	0.19	18.4	15.7	6.3	19	2·10^{-2}	0.1	27
3/1	403	7.1	0.8	5.7	0.26	18.6	24.5			4·10^{-2}		

Figure 32 Rate of adsorption at the external surface (r_{ads}, left) and rate of pore entrance (r_{pe}, right) as a function of the carbon number determined in H-ZSM5 at 403K. The data presented herein were determined by periodic volume perturbation experiments of both the single components (black) and the corresponding 1/1 mixtures (green) with benzene.
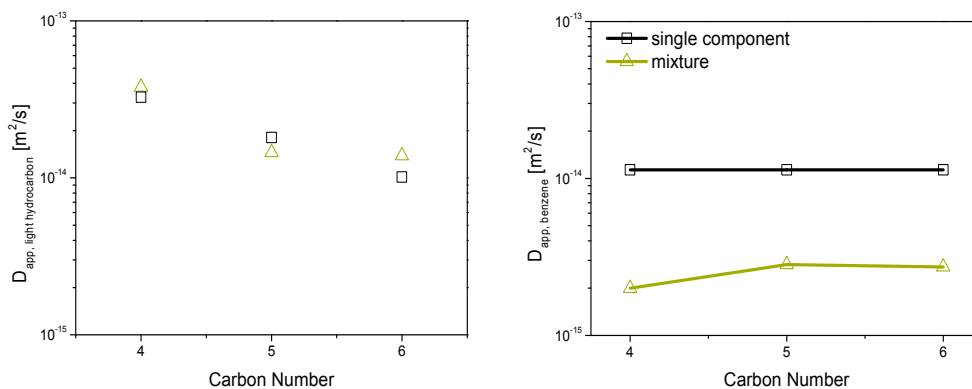
Figure 33 Comparison between the apparent diffusion coefficient obtained from periodic volume perturbation experiments of benzene applied as a single component (black) and within a 1/1 mixture (green) with either n-butane, n-pentane or n-hexane (right) as well as of the corresponding light hydrocarbon molecules as single components (black) and in the presence of benzene (green). The diffusivity is presented as a function of the carbon number of the corresponding light hydrocarbon molecule in the binary mixture.

4.5. *Discussion*

Based on the understanding gained in previous studies [160] a model (Figure 27, Eqs. (2.4.31) and (2.4.59)) was developed, which describes the adsorption at the external surface, the pore entrance step as well as the apparent transport diffusivity including interactions of sorbate molecules in binary mixtures. However, in a suitable system for the examination of external transport limitations the pore entrance step has to be rate determining. This is the case for sorption processes of small aliphatic and aromatic molecules adsorbed in zeolite ZSM-5 with primary particles smaller than approximately 15 μm [94]. Moreover, this system has the advantage of exhibiting

sufficiently large differences in molar extinction coefficients between external and internal sorption sites, allowing to track the external and internal concentrations of light hydrocarbons simultaneously (Eqs. (4.2.1) and (4.2.2)). Rates and rate constants of adsorption at the external surface and pore entrance are directly accessible enabling a quantitative understanding of the transport network, both as single components and within mixtures.

In order to understand the effect of benzene addition on the diffusivity of the light hydrocarbons and vice versa, the impact of each parameter on the overall transport rate needs to be understood. All rates and rate constants are summarized in Table 8, Table 9 and Table 10. The rate of adsorption at the external surface is determined by the corresponding rate constant and the change in external equilibrium coverage. Please note here, that the rate of adsorption at the external surface is directly proportional to the sticking probability.

According to Reitmeier et al. four properties influence the sticking probability: (1) the degrees of translational and rotational freedom loss after the sorption, (2) the initial entropy of the gas-phase molecule, (3) the compensation of the heat of sorption, and (4) the geometrical dimensions of the molecules that determine the space occupied on the surface [139]. For the present system the loss in degrees of translational and rotational degrees of freedom are equal for all tested molecules, whereas the gas phase (initial) entropy of the sorbates decrease from n-hexane (ΔS^o_{gas}=389 J mol^{-1} K^{-1}) to n-pentane (ΔS^o_{gas}=349 J mol^{-1} K^{-1}) and n-butane (ΔS^o_{gas}=310 J mol^{-1} K^{-1}). However, sorption experiments show that the loss in entropy upon sorption on a silica surface is equal for all three molecules (~48 J mol^{-1} K^{-1}) (Table 11) [160]. Thus, the adsorption rate and hence the directly proportional sticking coefficient are mainly determined by the heat of adsorption and size of the sorbates, which perfectly corresponds to the increasing adsorption rate with increasing chain length. Benzene addition decreased the rate of adsorption by about 10-30%, which is assigned to the decrease in the equilibrium coverage (1-2%) and the lower rate constant (10-25%) (Table 8, Table 10). The relative changes of the two parameters suggest that the decrease in the sorption rate constant is the dominating factor in the overall decrease rather than a statically reduction of the coverage at the external surface. This suggests that the sorption process of benzene requires a

proportionally larger area at the surface than the adsorption of the alkanes, i.e., it is sterically more demanding, leading to disfavoring of the benzene adsorption step.

Table 11: Thermodynamic adsorption data of n-butane, n-pentane, n-hexane and benzene determined on fumed silica as model material for the external surface of the zeolite [160].

	$\Delta H_{Ads,ext}$ [kJ mol^{-1}]	$\Delta S_{Ads,ext}$ [J mol^{-1} K^{-1}]	$\Phi_{max,ext}$ [mmol g^{-1}]	$K_{Ads,ext}$ 343K [-]	$K_{Ads,ext}$ 373K [-]	$K_{Ads,ext}$ 403K [-]
Butane	-14	-52	0.31	0.2	0.1	0.1
Pentane	-15	-44	0.27	0.9	0.6	0.4
Hexane	-20	-48	0.24	-	1.7	1.1
Benzene	-18	-38	0.35	6.8	4.0	2.6

The next consecutive step within the network is the pore entering, which again depends on two parameters, the rate constant and the coverage of the sorbates at the external surface. The rate constant is proportional to the pore entrance probability, which is mainly determined by the sorbate mobility on the external surface and their steric demands. Thus, it decreases with increasing chain length by about 20% from n-butane to n-pentane, whilst the coverage at the external concentration increases at the same time due to a higher heat of adsorption (Table 11). It is well seen that the change in surface coverage upon the periodic pressure modulation over-compensates the reduction in pore entrance probability resulting in an increase of pore entrance rate with chain length (Table 8). In conclusion, the pore entering rate is governed by mobility, the steric demand and the heat of adsorption at the external surface of the sorbate molecule.

It was found that the pore entrance rate is in the order of 10^{-4}-10^{-5} µmol g^{-1} s^{-1}, which is one order of magnitude smaller than the rate of adsorption at the external surface (Table 4). According to these experiments the pore entrance is the slowest step in the transport network and, thus, rate determining, which is in line with previous studies in small crystal zeolites [75, 94, 137, 138] The addition of benzene reduces the pore entrance rate by 7-20% and the rate constant by 6-19%, while the coverage at the external surface decreases insignificantly (1-2%) (Table 8, Table 10). Thus, the decrease of the rate constant and the related decrease of the probability for the pore entering determine the overall rate. On the other hand, the steric demand for the sorption of the light hydrocarbon does not change upon the addition of benzene.

Hence, two possible reasons can be found for the decrease in rate constant, which are either the hindrance of sorbate movement at the external surface by the presence of benzene or the competitive adsorption of both molecules at the pore mouth sites of the zeolite. Both effects are related to molecule-molecule interactions, but impossible to differentiate at present.

Please note, that the determination of the pore entrance rate is much more sensitive than the measurement of the apparent diffusion coefficient. This is related to the specific analysis procedure. The pore entrance rate is determined from the external concentration profile, while the apparent diffusion coefficient is extracted from the internal concentration profile. As the difference in ratios of molar extinction coefficients of the stretching and deformation vibrational band is about an order of magnitude larger for molecules at the external surface compared to those being adsorbed at internal sites (Table 6) [160], the external concentration can be determined much more accurately than the internal concentration according to Eqs. (4.2.1) and (4.2.2). Thus, the reduction in apparent diffusion coefficient of light hydrocarbon molecules upon benzene addition was too small to be determined quantitatively. However, the pore entrance rate of hexane was neither determinable as single component nor in a mixture with benzene, because the difference in molar extinction coefficient decreases with chain length, which makes the determination of the external concentration less accurate. In combination with a very slow pore entrance rate and, thus, a very flat concentration profile the extraction of r_{pe} is impossible for hexane.

Interestingly, the apparent diffusivity of benzene was about 70-80% smaller compared to the single components when benzene was mixed with light alkanes (Figure 33, Table 9, Table 10). This is in contrast to previous theoretical studies. Molecular dynamic simulations showed that the intersections of ZSM-5 pores act as a bottleneck for faster diffusing linear alkanes ranging from methane to hexane, because they are blocked by the slower diffusing benzene molecules and reduce the light hydrocarbon diffusivity to almost zero [110]. However, those studies were assuming that the intracrystalline diffusion is the rate limiting step and were neglecting all surface processes.

The reduction of benzene diffusivity upon addition of alkanes plus the diffusivity of the latter exhibiting a minor decrease show that intersection blocking is not rate determining in a system limited by rate of pore entering. Thus, the results are

attributed to be caused by the statistical occupation of the pore mouth sites by light hydrocarbons reducing the apparent benzene diffusivity. By this means, pore entrances are blocked for benzene sorption if covered by a light hydrocarbon molecule and vice versa. But the probability for a light hydrocarbon molecule to be present in the pore mouth is significantly higher than for benzene due to smaller difference in sorption probability at the pore mouth and the internal sorption sites expressed by the adsorption equilibrium constant K_{Ads} (Table 7, Table 11). Although it is impossible to measure K_{Ads} at pore mouth sites directly, a good approximation can be obtained by comparing K_{Ads} at the external and internal sites. The steric environment for sorbates at such sites near the pore entrance is in between internal and external sites and in consequence also the corresponding sorption equilibrium constant should also be between the values for internal and external sites. Hence, the difference between the internal and the pore mouth sites decreases with decreasing difference in K_{Ads} at internal and external sites (Table 7, Table 11). The resulting coverage is two to five times larger for the alkanes under investigation compared to benzene, which is in line with the obtained differences obtained in the transport measurements.

Although the heat of adsorption at internal sorption sites is higher for alkanes than for benzene, the adsorption probability represented by K_{Ads} shows the opposite trend (Table 7). The reason for this difference is caused by the 40-120 J mol^{-1} K^{-1} larger gas phase entropy compared to that of benzene (cf. $\Delta S^o_{gas,benzene}$=269.58 J mol^{-1} K^{-1}) [162]. Thus, the significantly smaller entropy loss of benzene compensates its smaller heat of adsorption and yields a higher probability for binding at internal sorption sites compared to light hydrocarbon molecules. As all sorbates investigated have comparable adsorption equilibrium constants at the external surface (Table 11) [160] the difference in sorption probability at pore mouth sites is inversely proportional to K_{Ads} at the internal sorption sites, which decreases in the order benzene>n-hexane>n-pentane>n-butane. Thus, the probability for blocked pore mouth sites increases with decreasing chain length of the alkane, which is in-line with the results of the co-adsorption experiments presented herein.

The diffusivity of benzene in mixture with a 3 times as high n-butane concentration reduced the benzene diffusivity by more than 99% (Table 8,Table 10), which strongly

indicates that the proposed blockage of pore entrances is the mechanism responsible for the decrease in benzene sorption rate.

4.6. *Conclusions*

Using a new approach for the determination of transport processes in multicomponent mixtures based on fast-time resolved infrared spectroscopy is presented. The measurement of transport properties of linear C4-C6 alkanes in an equimolar mixture with benzene in nano-sized H-ZSM5 was elucidated on a molecular level. By using a mathematical model describing the adsorption at the external surface, the pore entrance step and the intracrystalline diffusion it was shown that the pore entrance step is rate limiting in such systems. Both, the adsorption at the external surface as well as the pore entrance step of the aliphatic molecules were slightly slowed down in the presence of benzene (10-30%), which can be assigned to molecule-molecule interactions rather than to a decreased coverage at the external surface (1-2%). On the other hand, the apparent diffusion coefficients of benzene decreased by about 70-80% compared to the single component in the presence of light hydrocarbons. This effect is attributed to a statistical reduction of the available pore openings for the benzene molecules as the probability of light hydrocarbon molecules being sorbed in the pore mouth is significantly higher than for benzene due to a smaller difference in adsorption equilibrium constant between internal and pore mouth sites.

Chapter 5

Diffusion of benzene/p-xylene mixtures in MFI particles, pellets and grown membranes

Abstract

The transport and separation of mixtures between benzene and p-xylene in pellets prepared by pressing of ZSM-5 powder and a dense supported (crystalline) Silicalite-1 membrane were compared to isolated ZSM-5 crystallites. The kinetics of the transport in the pressed pellet and the grown membrane determined in a Wicke Kallenbach cell (313 - 403 K; partial pressure range 200 – 2300 Pa) differed significantly from those measured for isolated ZSM-5 particles with the pressure modulation frequency response technique (343-403 K; partial pressure 30 Pa). In a pressed pellet, the transport was of Knudsen type leading to high fluxes of 10^{-4} mol/m^{2}s and identical permeances for benzene and p-xylene. The diffusion coefficient in a pressed pellet exceeded that in particles, in which the transport was controlled by intracrystalline diffusion and the pore entrance step, by 8 orders of magnitude. The flux across a grown silicalite-1 membrane was two orders of magnitude lower and the permeability of p-xylene was 2.6 to 5 times higher than that of benzene. The change in diffusivity in the membrane compared to the particles results from the higher surface coverage of p-xylene.

5.1. *Introduction*

The energy and cost efficient separation of hydrocarbons such as xylene isomers is a challenging task on the academic as well as on the industrial scale. The similar vapor pressure of the three xylene isomers makes the separation by distillation economically unfeasible. Therefore, the separation is performed on an industrial scale by preferential adsorption (Parex Process, UOP) or by fractional crystallization [163]. Both approaches require high energy input and high investments in the process equipment.

The continuous separation of p-xylene from a mixture of xylenes and other (substituted) aromatic molecules based on membranes [101, 114-117, 164-166] as well as on hierarchical zeolites [35] is one of the promising alternative approaches, which has been addressed in a large number of studies during the last years. These studies have led, however, to controversial results. Keizer et al. suggested that the separation of a binary mixture of p-xylene/o-xylene (0.31/0.26 kPa) is possible using a MFI membrane of 3 μm thickness utilizing the different minimum kinetic diameters of the molecules [115]. The flux of p-xylene in a mixture with o-xylene increased, whereas the o-xylene permeability decreased markedly compared to the transport of single components. The temperature dependence of the p-xylene permeance in mixtures allowed increasing the separation factor from <2 to 25 by increasing the temperature from 293 to 473 K. This was attributed to size exclusion effects and the varying coverage on the external surface.

A much better separation was obtained by Sakai et al. employing MFI membranes of 60 to 130 μm thickness [117]. They reported a maximum in the separation factor for p-xylene of 250 at 473 K applying a ternary xylene mixture with similar partial pressures of 0.3, 0.27 and 0.27 kPa for p-, o- and m-xylene, respectively. In agreement with Keizer et al. [115], this maximum was attributed to competitive effects between the diffusion and the adsorption. Interestingly, it was reported that the membrane permeability increased linearly with increasing p-xylene concentration, but was independent of the temperature.

In contrast, Falconer and Noble [101, 114, 116] reported a separation factor for o-xylene and p-xylene in a binary mixture for ZSM-5 and silicalite-1 membranes close to one over the temperature range studied (380 - 480 K). Notably, the permeances in the mixtures were lower than those for the single components. This was attributed to a

single file transport mechanism, i.e., that the faster permeating substance is retarded relative to the rates of the slower molecule, as the molecules cannot pass each other inside the pores.

These latter data also indicate that the permeability of a molecule in a binary mixture through a zeolite-membrane may not be directly related to the diffusion coefficient in powder samples. Gobin et al. [135] reported recently the intracrystalline diffusion coefficients of 5.28 x 10^{-13} and 2.46 x 10^{-13} m^2/s for benzene and p-xylene in ZSM-5 at 373 K, respectively, while the permeation fluxes of the same molecules through the silicalite-1 membranes showed the opposite trend (10^8 and 3 x 10^8 mol/(s m^2 Pa) for benzene and p-xylene, respectively) [101].

Our aim is, therefore, to contribute towards understanding of the transport mechanism in MFI membranes and to address these discrepancies. Extension of this comparison to pressed MFI pellets aims at helping to understand the impact of compacting powder on the overall transport properties and can serve as model for understanding the elementary transport processes in hierarchically structured zeolites.

5.2. *Experimental*

5.2.1 Materials

H-ZSM-5 powder with a Si/Al ratio of 45 was provided by Süd-Chemie. SEM images (Figure 34A) show that the sample consists of agglomerates with an average size of 360 ± 170 nm as determined by dynamic light scattering. The transmission electron micrograph is shown in Figure 34B illustrating a primary particle size of 50-100 nm, which agrees well with the estimate from the half-width of the reflexes of the X-ray diffraction pattern. The N_2 sorption isotherm indicates a BET surface area of 423 m^2/g and a micro-, meso-, and macropore volume of 0.12, 0.04 and 0.22 cm^3/g, respectively. The external surface area was 65 m^2/g. A detailed analysis of the material properties including the analysis of the transport mechanisms of aromatics can be found elsewhere (see ref. [135]).
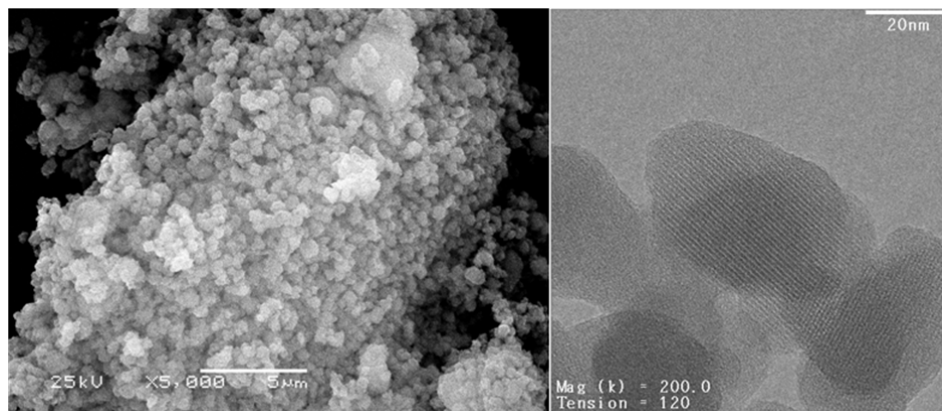
Figure 34: SEM (left, A) and TEM (right, B) image of the ZSM-5 powder

The Silicalite-1 membranes were produced by the Fraunhofer Institute for Ceramic Technologies and Systems IKTS, with an average thickness of 30 to 60 μm. The Silicalite-1 samples are supported on an asymmetric pellet made of titanium-dioxide and with a minimum pore size of 30 nm.

The adsorbates benzene and p-xylene (GC standard, > 99.96 %, Sigma Aldrich) were used without further purification.

5.2.2 Physicochemical Characterization

The N_2 physisorption isotherm and the SEM images were measured and analyzed according to Gobin et al. [135]. X-ray diffraction (XRD) patterns were recorded on a Rigaku Miniflix II XRD powder diffraction system using CuKα radiation ($\lambda_{K\alpha 1}$ = 1.54051Å, 30 kV and 15 mA). The XRD patterns were recorded in the scanning mode from 5-60° (2θ) at a detector angular speed of 2 °/min and step size of 0.02°.

The concentration and strength of acid sites were determined via the IR spectra of adsorbed pyridine described in detail ref. [167].

5.2.3 Calculation of the diffusion coefficient

A detailed description of experimental techniques including the theoretical background, the equations needed for data processing and information about the equipment can be found in section 2.4.1

5.3. *Results*

5.3.1 **Physical state of the membranes**
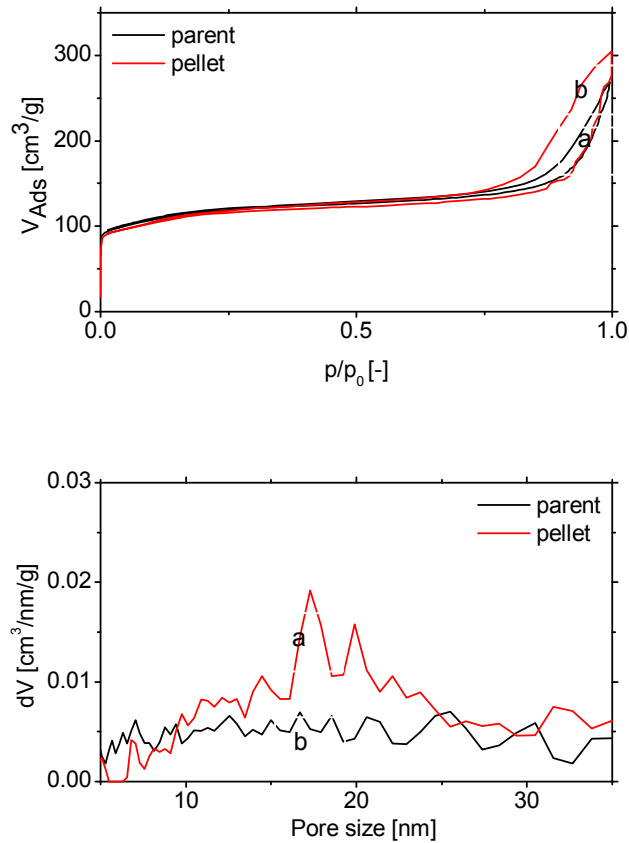
Figure 35: Nitrogen sorption isotherm (top) and the corresponding pore size determined by DFT analysis (bottom) of the parent ZSM-5 material before (black, a) and after (red, b) pressing it to a pellet for Wicke Kallenbach experiments

The pressed ZSM-5 pellet represents essentially an assembly of small particles with a size of 360 ± 170 nm and mesopores in between these particles. The pore size and volume of the pellet were determined from a nitrogen sorption isotherm (see Figure 35 for comparison with the powdered material). The pressure region from the adsorption branch up to $p/p_0 = 0.25$ was nearly identical for the powder and the pellet, which indicates that the micropore volume remained unmodified by the compacting procedure. BET analysis [69] of the N_2 adsorption isotherm of the pellet resulted in a specific surface area of 446 m^2/g which is identical to that of the isolated particles (420 m^2/g). The hysteresis in the sorption isotherm was observed at significantly lower p/p_0 values, i.e., 0.25 and 0.75 for the pressed powder and for the isolated

particles, respectively, and the total area of the hysteresis loop obtained was also much larger in the case of the pellet.
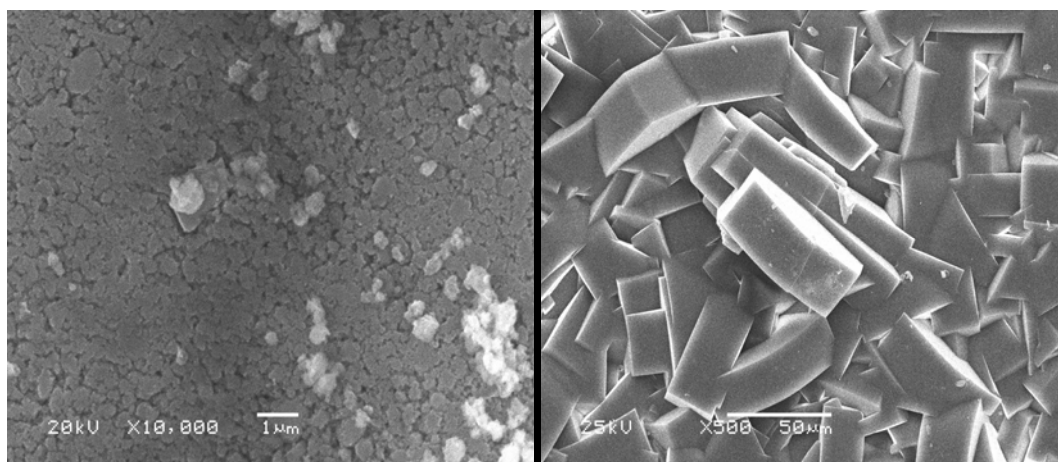
Figure 36: SEM images of a pellet used for Wicke Kallenbach experiments (left) and a grown Silicalite-1 membrane (right)

The total volume of the micro- and mesopores of the ZSM-5 powder and pellet was determined by using t-plot analysis according to the method of Halsey [168]. The results are summarized in Table 12. A total micropore volume of 0.147 cm^3/g was observed for both samples, while the mesopore volume increased from 0.132 cm^3/g to 0.232 cm^3/g in the pellet. The analysis of the pore size distribution of the pellet applying DFT analysis showed a maximum at 17 nm, whereas the minimum mesopore diameter is 6 nm (Figure 35).

Table 12: Porosity of ZSM-5 in the powdered and the pressed form

Material	S_{BET} [m^2/g]	V_{Micro} [cm^3/g]	V_{Meso} [cm^3/g]
parent	420	0.147	0.132
pellet	446	0.147	0.232

The SEM images of the pellet and the membrane are shown in Figure 36. On the surface of the pellet macropores exist between the isolated particles. In contrast, the grown membrane shows a texture composed of well-defined intergrown crystals of 50 μm diameter. The XRD pattern of the Silicalite-1 membrane was identical to that of ZSM-5 (Figure 37A). Reflections assigned to the TiO2 carrier of the membrane were

present in Figure 37B. The results of the acid site determination are summarized in Table 2.
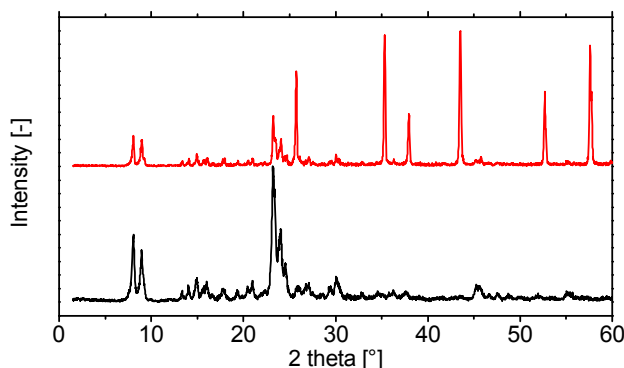
Figure 37: XRD patterns of ZSM-5 zeolite (A) and Silicalite-1 membrane (B)

Table 13: Acid site concentration of ZSM-5 and Silicalite-1 membrane determined by IR spectroscopy of adsorbed pyridine

Material	Brønsted acid sites [mmol/g]	Lewis acid sites [mmol/g]	Total acidity [mmol/g]
H-ZSM-5	0.360	0.091	0.451
Silicalite-1 Membr.	0.0	0.011	0.011

5.3.2   Transport Measurements

Zeolite Particles

The diffusivities of benzene and p-xylene were determined by the frequency response method at 343 K, 373 K and 403 K. The results from a previous publication by Gobin et al. [94] are compiled in Table 14. The resulting characteristic functions were analyzed under the assumption that intracrystalline diffusion control determines the apparent diffusivity and that a Gaussian type particle size distribution exists confirmed by DLS measurements [94, 135]. The out-of-phase functions of benzene and p-xylene at 403 K are compared in Figure 38. The shape of both curves is similar without any broadening of the p-xylene response, which indicates that the diffusion process in small ZSM-5 particles is isotropic. Note that the transport of p-xylene in larger ZSM-5 particles (3 μm particle size) is non-isotropic with a much faster diffusion in the straight channel system [94, 135, 169].

Table 14: Transport data and fitting parameters obtained for a theoretical model assuming one apparent diffusion process D_{app} with a Gaussian particle distribution as additional fitting parameter [94].

	T [°C]	L^2/D [s]	D_{app} x 10^{15} [m^2/s]	K [-]	NRMS-Error [-]	E_A [kJ/mol]
benzene	343	32.5	3.96	0.73	0.26	
L =3.59 x 10^{-07} m	373	17.6	7.34	0.46	0.19	23
σ =2.12 x 10^{-07} m	403	10.0	12.9	0.29	0.16	
p-xylene	343	132.9	0.97	0.77	0.30	
L =3.59 x 10^{-07} m	373	52.0	2.48	0.57	0.32	35
σ =2.32 x 10^{-07} m	403	21.4	6.02	0.39	0.19	

The apparent diffusion coefficients of benzene and p-xylene in the small particles are two orders of magnitude smaller compared to those in the large particles, whereas the time constants for diffusion (L^2/D) remain in the same order of magnitude. This has been attributed to the fact that the surface adsorption and the pore entrance step are controlling the rate of the overall transport due to the short length of diffusion in small particles [94]. This conclusion has been supported by the apparent activation energies (Figure 39). The results are also presented in Table 14. The obtained apparent activation energies in the small particles studied here are slightly higher than the ones observed in larger particles [94].
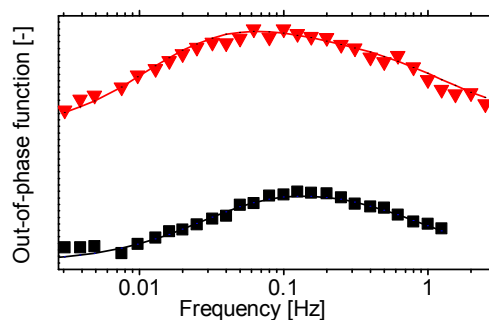
Figure 38: Out-of-phase frequency response of benzene (black) and p-xylene (red) at 403 K. The fits (lines) were obtained by using a single diffusion model including a Gaussian particle size distribution and considering a surface resistance. The p-xylene curve is shifted by 0.2. [94].
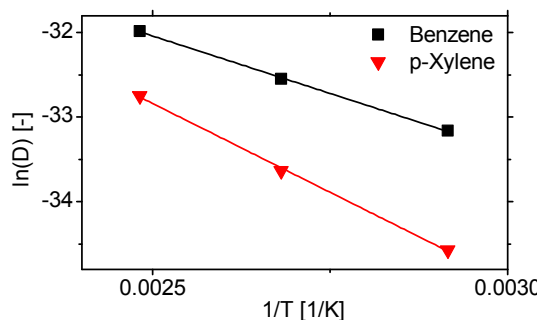
Figure 39: Arrhenius plots for benzene (black) and p-xylene (red) of apparent diffusion on ZSM-5 powder [94].

Pressed Pellets
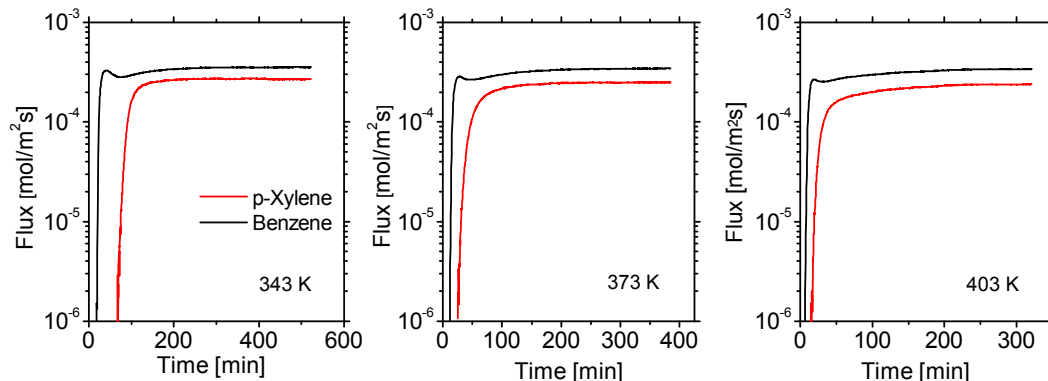
Figure 40: Flux of benzene/p-xylene mixtures (313 Pa/234 Pa) in the Wicke Kallenbach experiment on ZSM-5 at 343 K (left), 373 K (middle) and 403 K (right).
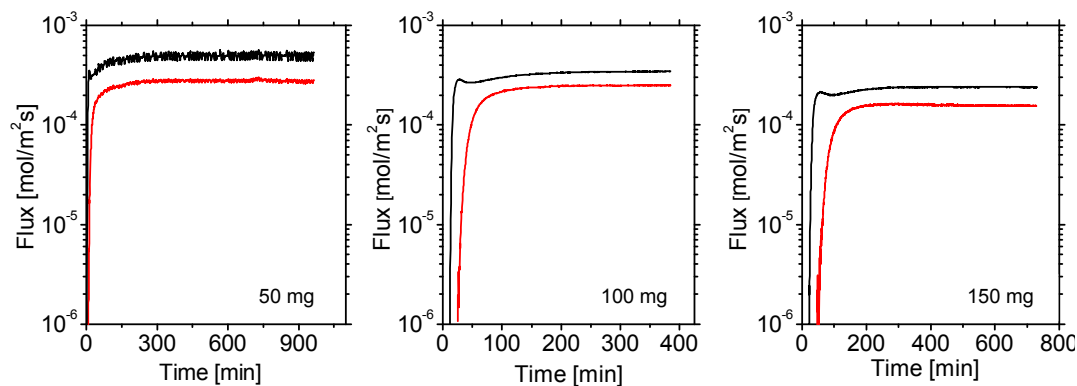
Figure 41: Flux of benzene/p-xylene mixtures (313 Pa/234 Pa) in the Wicke Kallenbach experiment on ZSM-5 as function of the pellet thickness at 373 K.

Figure 40 shows the transient fluxes of benzene and p-xylene mixtures in a pressed pellet (100 mg) at 343 K, 373 K and 403 K. The overall trends of the concentration traces are identical for all experiments. After an initial time period, a sharp increase of the flux was observed, followed by steady-state flux of both substances through the pellet. All of the experiments indicate an earlier breakthrough of benzene as the temperature increases. The benzene concentration at the eluate side exceeded the steady state concentrations shortly after the first appearance of benzene on the effluent side ("overshooting").

The steady state fluxes do not change between 343, 373 and 403 K (see Table 15) indicating that the permeabilities are identical for benzene and p-xylene and therefore, the separation does not occur.

Table 15: Steady state flux (F), breakthrough time (t_{transm}) and the permeance (P) of benzene and p-xylene as well as the separation factor (S) for a pressed ZSM-5 pellet at 343 K, 373 K and 403 K

T [K]	$F_{benz.}$ x10^4 [mol/(sm^2)]	$F_{p-xyl.}$ x10^4 [mol/(sm^2)]	$t_{transm., benz.}$ [min]	$t_{transm., p-xyl.}$ [min]	$P_{benz.}$x10^7 [mol/(s m^2 Pa)]	$P_{p-xyl.}$ x10^7 [mol/(s m^2Pa)]	S [-]
343	3.55	2.67	19	47	7.48	7.44	1.00
373	3.45	2.51	12	27	7.28	6.72	0.93
403	3.4	2.41	7	17	7.18	6.42	0.89

Table 16: Steady state flux (F), breakthrough time (t_{transm}) and the permeance (P) of benzene and p-xylene as well as the separation factor (S) for a pressed ZSM-5 pellet with weights of 50, 100 and 150 mg at 373 K

W [mg]	$F_{benz.}$ x10^4 [mol/(sm^2)]	$F_{p-xyl.}$ x10^4 [mol/(sm^2)]	$t_{transm., benz.}$ [min]	$t_{transm., p-xyl.}$ [min]	$P_{benz.}$x10^7 [mol/(s m^2 Pa)]	$P_{p-xyl.}$ x10^7 [mol/(s m^2 Pa)]	S [-]
50	5	2.75	3	9	10.9	7.98	0.73
100	3.45	2.51	12	27	7.28	6.72	0.93
150	2.39	1.55	23	47	5.08	4.31	0.85
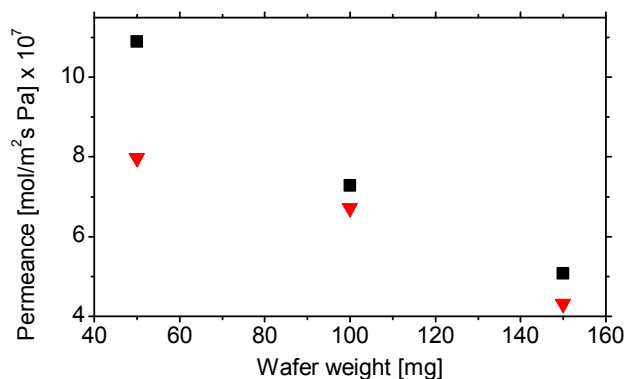
Figure 42: Permeance as function of the pellet thickness for benzene/p-xylene (313 Pa/234 Pa) on ZSM-5 at 373 K.

The influence of the pellet weight (which is proportional to its thickness) on the transient flux examined using pellets of 150 mg, 100 mg and 50 mg weight (equal to 1.5, 1 and 0.5 mm thickness) is shown in Figure 41. Two major trends can be observed. The fluxes decreased by 50%, when the pellet thickness is tripled and the "overshooting" of benzene is reduced with decreasing thickness and was fully eliminated on the thinnest (0.5 mm) pellet. The ratio of the steady state permeances of benzene and p-xylene were not affected by the pellet thickness (see Figure 42), while the overall fluxes decreased with the thickness. The time until breakthrough increased

with increasing thickness. The obtained results with pressed pellets are summarized in Table 15 and Table 16.
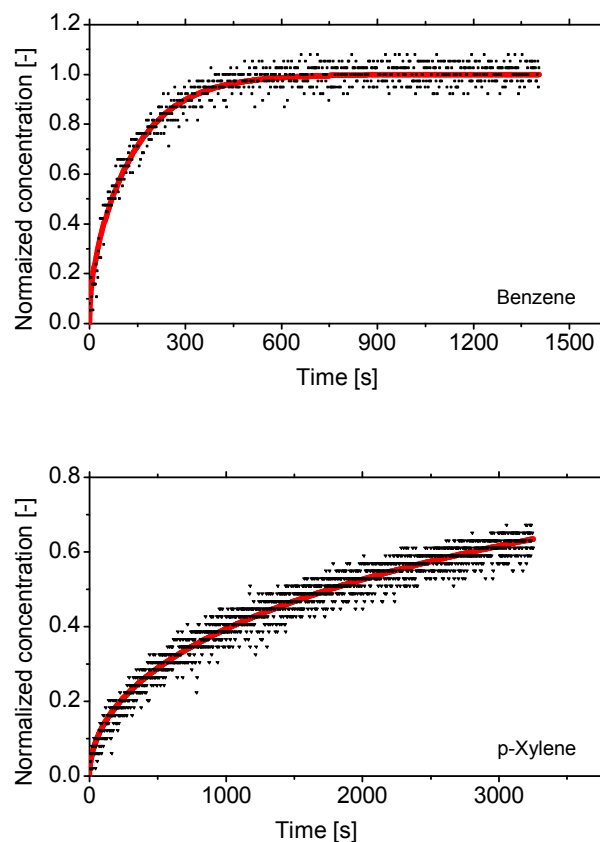
Figure 43: Gravimetric uptake rates of benzene (top) and p-xylene (bottom) with the pressed ZSM-5 at 373 K, applying a pressure step from 0.1 to 1 mbar.

The gravimetric uptake rates of benzene and p-xylene were determined in a separate experiment (see Figure 43). For benzene a diffusional time constant (L^2/D) of 1830 s was observed for a pressure step from 10 to 100 Pa corresponding to a diffusion coefficient of 1.36×10^{-10} m^2/s (assuming an infinite plain sheet model assumption [118] and a length of diffusion equal to the half of the wafer thickness). For p-xylene the time constant of diffusion was 57670 s resulting in a diffusion coefficient of 4.33×10^{-12} m^2/s. Note the model applied assumes a one dimensional diffusion process, which is a valid simplification for the case of the adsorption into a pellet.

Grown Membranes

The experimental results with the grown Silicalite-1 membranes differ significantly. The permeance and molar flux are two orders of magnitude lower than that observed with the pressed pellet. Although the overall shape of the curves is similar to the pressed pellets, the temperature dependence is much stronger. As shown in Figure 44, the "overshooting" effect of benzene decreased with increasing temperature turning into an exponential increase at 403 K. The p-xylene transient curves are exponential functions over the whole temperature range.
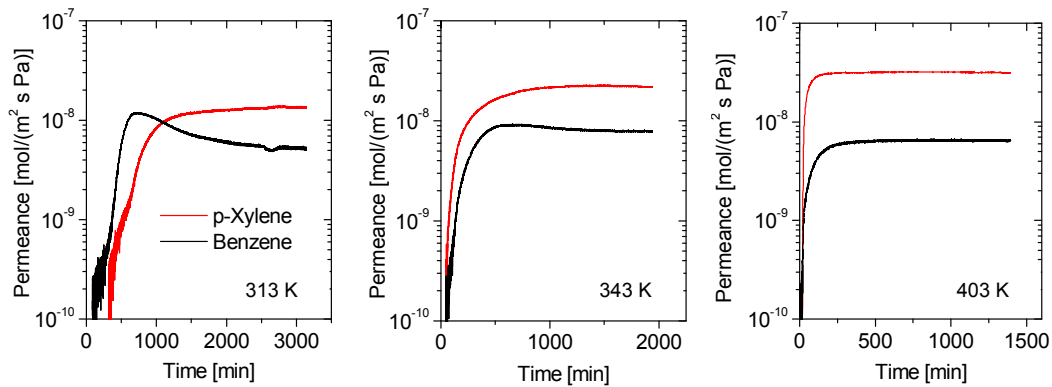
Figure 44: Permeance of benzene (a)/p-xylene (b) mixtures (578.7 Pa/322.9 Pa) in the Wicke Kallenbach experiment on the Silicalite-1 membranes at 313 K, 343 K and 403 K

Table 17: Single component fluxes (F) and permeances (P) of benzene (578.7 Pa) and p-xylene (322.9 Pa) obtained by Wicke Kallenbach experiments using a Silicalite 1 membrane of 30 to 60 µm at 313 K, 343 K and 403 K.

T [K]	$F_{benz.} \times 10^6$ [mol/(s m^2)]	$F_{p-xyl.} \times 10^6$ [mol/(s m^2)]	$P_{benz.} \times 10^9$ [mol/(s m^2 Pa)]	$P_{p-xyl.} \times 10^9$ [mol/(s m^2 Pa)]
313	3.5	3.91	6.05	12.1
343	2.85	8.65	4.92	26.8
403	2.52	12.82	4.35	39.7

Table 18: Steady state flux (F), breakthrough time (t_{transm}) and the permeance (P) of benzene and p-xylene as well as the separation factor (S) for a Silicalite 1 membrane at 343 K, 373 K and 403 K.

T [K]	$F_{benz.} \times 10^6$ [mol/(sm^2)]	$F_{p-xyl.} \times 10^6$ [mol/(sm^2)]	$t_{transm., benz.}$ [min]	$t_{transm., p-xyl.}$ [min]	$P_{benz.} \times 10^9$ [mol/(sm^{2}Pa)]	$P_{p-xyl.} \times 10^9$ [mol/(sm^{2}Pa)]	S [-]
313	2.98	4.34	350	500	5.2	13.55	2.63
343	4.56	7.24	60	60	7.9	22	2.78
403	3.72	10.13	17	18	6.5	31.5	4.76

As with the pressed pellets, the time required for the concentration front to pass through the pellet was shortened with increasing temperature. However, the time to establish equilibrium was much longer in comparison to the pressed pellets. Note that the lengths of the transmission times are identical for benzene and p-xylene at 343 K and 403 K, while at 313 K benzene passed faster through the membrane. The fluxes and permeabilities of benzene, p-xylene and mixtures of both components are compiled in Table 17 and Table 18, respectively.

Interestingly, the steady state concentrations indicate a higher permeability for p-xylene than for benzene in experiments with single components as well as with binary mixtures.

The p-xylene permeation increased stronger with the temperature compared to that of benzene, therefore, the separation factor is higher than one and increases markedly with the temperature. The highest ratio between the single component permeabilities of p-xylene and benzene (i.e., 8.6 shown in Table 17) was obtained at 403 K. This value decreased to 5 for the mixture of both components (578.7 Pa/322.9 Pa). The trend of the permeances of the single components compared to the binary mixtures as function of the temperature is shown in Figure 45. The single component permeability for both adsorbates at 313 K was identical to the mixture, while it clearly differed at higher temperatures. Notably, the single component flux of p-xylene increased more rapidly than that in a mixture, which led to a decrease of the p-xylene permeance by 21 % in a mixture with benzene at 403 K. In contrast, the permeability of benzene increased by 49 % at 403 K compared to the diffusivity as a single component.

The fluxes of the single components in the examined crystalline Silicalite-1 membrane agreed well with those reported in ref. [101]. Note however, that in contrast to the previous report, a separation of the benzene/p-xylene mixture can be achieved. In order to determine the influence of the partial pressure of benzene and p-xylene on the permeation flux, the partial pressure of benzene in the feed was varied between 579 and 2315 Pa, while the p-xylene concentration was kept constant (Figure 46). The result showed a linear increase of the benzene flux, whereas an exponential decay of the p-xylene permeation was observed.
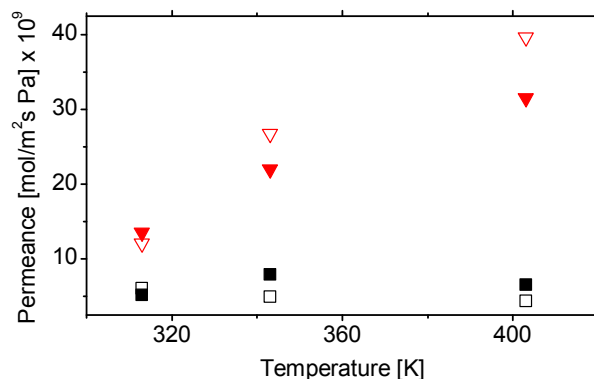
Figure 45: Permeance as a function of the temperature for benzene (∎)/p-xylene (▼)
(578.7 Pa/322.9 Pa) mixtures (filled symbols) compared to the single components (unfilled symbols)
with Silicalite-1 in Wicke Kallenbach experiments at 343, 373 and 403 K.
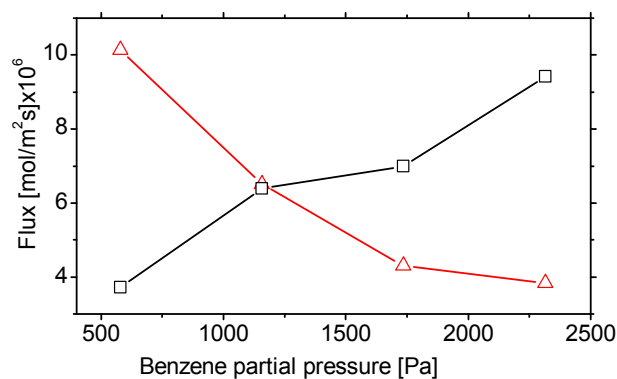
Figure 46: Permeation flux of benzene (∎) and p-xylene (▼) at varying benzene partial pressures using
Silicalite-1 membrane in a Wicke Kallenbach experiment at 403 K. The p-xylene concentration was
kept constant at 322.9 Pa.

5.4. *Discussion*

By comparing the transport characteristics in a single particles [75, 94, 135, 138] in
pellets and grown membranes (results presented in this publication) distinct
differences become apparent. Previous studies showed that in isolated particles the
diffusion of benzene is faster than that of p-xylene [94] and that the diffusion
coefficients for p-xylene are non-isotropic due to the reorientations required when
diffusing through the straight and the sinusoidal channel systems of MFI. In contrast,
the diffusion of benzene is isotropic because of the possibility to easily re-orientate in
the intersections in between the two channels. As mentioned before the diffusion
coefficients in the small particles ($\sim 10^{-15}$ m^2/s) are about two orders of magnitude

smaller than those obtained for larger particles [75, 94, 135, 138, 169]. For these (small) particles we have already shown by a detailed analysis of the transport network, that the overall process is determined by the surface adsorption (i.e., the sticking probability) and the pore entrance step and not by intracrystalline diffusion, as it is the case for larger particles (~3μm) [94]. In contrast to previously reported steady state diffusivities [170] the data presented in this paper for the isolated ZSM-5 particles are transport diffusivities. Note, that this results in a difference of four orders of magnitude as the steady diffusivities are corrected by the loading of the zeolite. Nevertheless, the diffusion coefficients of p-xylene presented here are in line with the steady state diffusion coefficients from Garcia et al. [170].

To ensure that the transport diffusivities are not influenced by capillary condensation of the sorbent the limits for the partial pressures for benzene (2700 Pa) and p-xylene (700 Pa) at 313 K were calculated according to the macroscopic Kelvin equation [171]. These values are increasing markedly with the temperature indicating that capillary condensation plays neither a role in the frequency response nor in the Wicke Kallenbach experiments.

The transport characteristic of a pellet with a thickness of 1 mm was significantly different to the isolated particles. The gravimetric uptake experiments clearly point to a shift in the rate determining step from processes on the surface (pore entrance) towards the diffusion inside the mesopores. This is supported by the fact that the time constants of diffusion measured by uptake experiments are two orders of magnitude larger than the time constants obtained in frequency response experiments on isolated particles [94]. The resulting diffusion coefficients of benzene and p-xylene in a pellet are 1.36×10^{-10} m^2/s and 4.33×10^{-12} m^2/s, respectively, which is three to five orders of magnitude larger compared to 7.34×10^{-15} m^2/s and 2.48×10^{-15} m^2/s observed for the isolated particles.

According to the Knudsen theory (Eq. 2.3.24), the diffusion coefficients of the transport of benzene and p-xylene inside the mesopores are 6.36×10^{-7} and 5.45×10^{-7} m^2/s, respectively, assuming that the diameter of the smallest mesopores in the pellet (6 nm) controls the diffusion.

$$D_{K,eff} = \frac{\varepsilon_P}{\tau_F} * \frac{d_p}{3} * \sqrt{\frac{8RT}{\pi M}} \qquad (5.4.1)$$

The comparison of the diffusion coefficients for diffusion in the micropores of isolated particles (10^{-15} m^2/s) [94] and in the mesopores (10^{-7} m^2/s) with that obtained

in the adsorption experiments (10^{-10} m^2/s) indicates that the rate of adsorption in a pressed pellet is controlled by both processes.

Considering the results of the experiments in the Wicke-Kallenbach cell a few experimental details have to be discussed first. These are (i) the time for the concentration front to pass through the pellet, (ii) the "overshooting" effect of the benzene concentration above the steady state concentration after the breakthrough and (iii) the molar fluxes under steady state conditions. All these effects can be explained by describing the pellet as a bed adsorber.

Note that the theoretical comparison of the uptake kinetics observed for benzene into particles to the transport inside the mesopores (controlled by Knudsen diffusion) supports the assumption of an adsorber. In order to calculate the transient diffusional flux and the adsorption kinetics, two models based on the Fickian law were used [118, 144]. According to Ruthven et al. the uptake into an isolated particle in the case of micropore diffusion control can be described under isothermal conditions by Eq. (5.4.2) [155]:

$$\overline{Q}(t) = \frac{c_A - c_0}{c_A - c_\infty} = 1 - \frac{6}{\pi^2} \sum_{n=1}^{\infty} \frac{1}{n^2} \exp(-n^2 \pi^2 D/L^2) \qquad (5.4.2)$$

In contrast, the solution of the Fickian law describing the diffusion through a membrane at initial conditions is given in Eq. (5.4.3) [118].

$$F(t) = -\left(\frac{D\delta c}{\delta x}\right)_{x=L} = 2c_F \sum_{n=1}^{\infty} \left(\frac{D}{\pi t}\right)^{1/2} \exp\left\{\frac{-(2n+1)^2 L^2}{(4Dt)}\right\} \qquad (5.4.3)$$

The simulated benzene uptake into a particle and the diffusional flux through a membrane are compared in Figure 47. If the particles are surrounded by mesopores, it can be assumed that the characteristic length of diffusion L is equal to the particle size. The diffusion coefficient D was determined previously by frequency response experiments [94] and the diffusional length in the mesopores is equal to the thickness of the pellet (1 mm for the standard pellet). The diffusion coefficient based on the Knudsen theory can be calculates using the pore size obtained by DFT analysis of the N$_2$ sorption isotherm. The results of the simulation are presented in Figure 47.
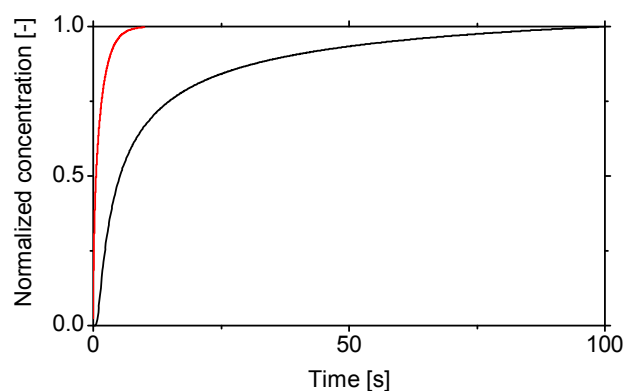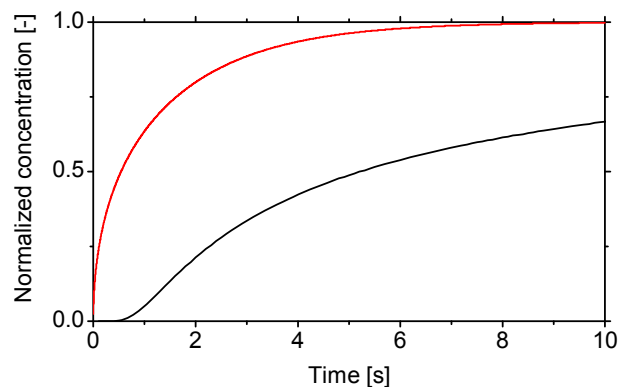
Figure 47: Simulated plots of the normalized gravimetric (a) and the normalized initial flux (b) through a mesoporous membrane.

Table 19: Comparison of the experimentally and theoretically obtained breakthrough times of benzene and p-xylene through a of ZSM-5 pellet at 343, 373 and 403 K as well as different weights of 50, 100 and 150 mg.

T [K]	Pellet-weight [mg]	$t_{Ex.,benz.}$ [min]	$t_{Ex.,p-xyl.}$ [min]	$t_{theo.,benz.}$ [min]	$t_{theo.,p-xyl.}$ [min]
343	100	19	47	23	54
373	100	12	27	15	29
403	100	7	17	7	15
373	50	3	9	5	13
373	150	23	47	33	71

The time constant of the uptake into the bulk of the pellet was found to be much smaller than the transport through the mesopores, which is in line with the changes in the adsorption kinetics observed on the isolated particles and the pressed pellets. As the difference between the two processes is about one order of magnitude both

processes influence the uptake kinetics. Furthermore, the simulation confirms the assumption that the pellet acts similar to a bed adsorber, as it shows that a molecule is faster adsorbed into the micropores of the particles surrounding the mesopores than diffusing through the mesopores in the pellet.

In this context it has to be noted that the time required to diffuse through the pellet depends on the sorption capacity of the material. The zeolite sample has a higher sorption capacity for p-xylene compared to benzene (i.e., about 1.5 to 1.7) [161], which leads to a longer breakthrough time of p-xylene. The time required for the concentration front to pass through the pellet was estimated by assuming that the flux into the pellet at the beginning of the experiment is identical with the steady state flux (described by Eq. 5.4.4). The time needed by the concentration front to pass through the pellet was calculated according to Eq. (5.4.4). The theoretical and experimental values are compared in Table 8.

$$t_{transm.} = \frac{N_{UC}*SO_{max}}{Q*A}$$
(5.4.4)

The divergence between the experimentally and theoretically obtained data is about 20 %. The theoretically calculated values are generally higher (except for one) than the experimental data, which is attributed to the competitive adsorption decreasing the maximum loading of benzene and p-xylene. The direct relation of the time required for the concentration front to pass through the pellet and the sorption capacity shows that the transport process is controlled by the sorption capacity (thermodynamics) rather than the transport rates in the mesopores (kinetic effect).

The adsorption enthalpies of 94 kJ/mol and 51 kJ/mol for p-xylene and benzene, respectively, can be used to explain the "overshooting" effect observed for benzene (Figure 40, Figure 41) according to the theory of an adsorber bed. The weaker adsorbing substance (i.e. benzene) passes first through the bed and shows a characteristic "overshooting", because it is replaced from the sorption sites by the stronger interacting, but slower diffusing second component (i.e. p-xylene), which shows an exponential time dependence for the transport through the pellet. Once the adsorption-desorption equilibrium is established, the concentrations of benzene and p-xylene passing through the pellet are independent of the time.

The most significant results of the Wicke-Kallenbach experiments are the flux and permeance ratios at steady state conditions. For the pressed pellets the permeabilities of benzene and p-xylene are equal and their ratio is independent of the temperature

and pellet thickness. The separation factor of one shows that a separation of these two aromatic components is not possible with a pressed pellet. Furthermore, the permeances are two orders of magnitude higher than in crystalline membranes. The diffusion coefficients for the benzene and p-xylene measured in the Wicke-Kallenbach cell were between 3.6 and 7.2 x 10^{-7} m^2/s, which can be related to an average pore diameter of 6.3 nm assuming Knudsen diffusion. This is consistent with the DFT analysis of the nitrogen sorption isotherm (Figure 35) and indicates that the steady state fluxes are controlled by the transport through interparticle mesopores. This allows describing the transport through the pressed pellet by two contributions. (i) The transient behavior, which results from the adsorption equilibrium and not from the intra- and interparticle diffusion. (ii) The steady state conditions, where the transport is solely controlled by Knudsen diffusion in the interparticle mesopores and consequently, the smallest pores determine the overall flux. Therefore, the separation inside the pellet is a process controlled by sorption equilibria (thermodynamics), while the permeability is determined by mesopore diffusion (kinetic effect).

Although the actual results confirm that it is impossible to separate aromatic molecules with pressed pellets of ZSM-5, it has a significant impact on the understanding of transport processes in extrudates because the ZSM-5 pellets can be seen as model systems for larger particles made by extrusion. The time constants of diffusion increased by two orders of magnitude from isolated particles to the compacted pellets of 1 mm thickness for benzene and p-xylene. This indicates the existence of an intra-particle diffusion limitation in the pressed particles, which allows establishing the sorption equilibrium over the individual particles. To avoid the limitation by intra particle diffusion the pore sizes in extrudates have to be enlarged. Rodrigues et al. indicated that effectiveness of chromatographic processes can be increased by using materials with larger pores as the effective diffusivity is augmented by convection [172]. Note that the selectivity of reactions will be influenced by re-adsorption. Certainly, reactions depending on the uptake characteristics of individual particles such as the shape selective toluene alkylation will face decreasing selectivity due to the enhanced adsorption rate of the product molecules during the retarded diffusion processes in the mesopores.

An entirely different transient and steady state transport regime was observed in crystalline Silicalite-1 membranes. Benzene showed a similar "overshooting" effect

under transient conditions at 313 K as in the pressed pellets, but this effect disappeared at 403 K. This indicates that the transport is controlled by a combination of adsorption and micropore diffusion, which can be described assuming a generalized Stefan-Maxwell diffusion formalism [173, 174]. At low temperatures the adsorption is decisive for the transient concentration curve because the surface coverages are generally high. Therefore, in binary mixtures the competitive adsorption leads to an "overshooting" of the concentration of the weaker adsorbing substance in the transient concentration profile [173]. As the surface coverage decreases with increasing temperature (by 75% from 313 K to 403 K) [161] and the diffusion coefficient increases at the same time, the impact of the competitive adsorption on the concentration profile decreases with increasing temperature (Figure 44).

To allow the prediction of the fluxes across membranes in binary systems by the Stefan-Maxwell theory, the density of the material, the surface coverage as well as its gradient through the pellet [174, 175] are required. According to the Stefan Maxwell theory the transport of a binary mixture through a membrane can be described by Eq. (5.4.5) [176]:

$$F_1 = -q_{sat}\rho \frac{\mathbb{D}_1}{(1-\theta_1-\theta_2)} [(1-\theta_2)\nabla\theta_1 + \theta_1\nabla\theta_2] \qquad (5.4.5)$$

This equation is valid for the special case of (binary) diffusion without interactions between the diffusing molecules. As the partial pressures of benzene and p-xylene were low, this boundary condition can be assumed as fulfilled and the equation can be used for describing the diffusion in the membrane.

In contrast to Fickian formalism, Stefan Maxwell diffusion describes a situation, where the surface occupation plays a decisive role for the transport. According to Bakker et al. [173], the adsorption strength is decisive for the separation selectivity. Due to competitive adsorption the surface occupancy of the weaker adsorbing substance is lowered, which in turn enhances the transport selectivity towards the stronger adsorbing substance. Although the saturation limit of benzene and p-xylene on ZSM-5 is 8 molecules per unit cell [161], the relative surface coverage of p-xylene is about 1.5 times higher in the pressure range of 10^2 to 5×10^3 Pa. As a consequence the p-xylene permeance exceeds that of benzene by a factor of 2.6 – 5 in accordance to the Stefan Maxwell theory, which relates the faster transport of p-xylene compared to benzene to the higher relative surface coverage at elevated temperatures [161].

This can be confirmed by the observation that the flux of benzene increases with increasing partial pressure in the feed, while at the same time the p-xylene flux decreased (Figure 46). This experiment indicates that the permeation flux in this system can be directly related to the surface coverage and the description in terms of the Stefan Maxwell formalism is valid (In contrast Fickian diffusion would predict that the permeation flux is independent of the surface coverage). Opposite trends for benzene and p-xylene were observed when comparing the membrane permeances of the single components to that of the mixtures (Figure 44). An increase of the permeability with increasing temperature was observed for benzene in comparison to the single component, whereas the permeability decreased for p-xylene. Krishna and van Baten showed in previous theoretical studies on C1 to C3 mixtures that the transport of the more mobile species in a mixture is slowed down, whereas the transport of the slower component is enhanced at the same time for zeolites with intersecting channel systems such as MFI, ISV and BEA [177, 178].

Another important result is that the single gas permeation of benzene is decreasing with increasing temperature, whereas it is increasing for p-xylene. This finding is interesting, because an opposite trend is observed with isolated ZSM-5 particles for benzene. The permeance of a membrane depends on the diffusivity and the surface coverage (Eq. 5.4.6). As the diffusivity increases with the temperature, while the surface coverage decreases, the latter must be responsible for the temperature dependency observed [179].

$$F_1 = -q_{sat}\rho \frac{\mathbb{D}_1}{(1-\theta_1)} \nabla \theta_1 \qquad (5.4.6)$$

Referring to previous publications, a maximum of the flux is found when the activation energy of diffusion is smaller than heat of adsorption [175]. Eq. (5.4.7) was developed from generalized Stefan Maxwell equations and it indicates that the maximum of the flux is obtained when the logarithmic mean of the free vacancies equals to the ratio of activation energy of diffusion and heat of adsorption [175]:

$$(1 - \theta_i)_{ln} = \frac{E_{A,D}}{\Delta H_{Ads}} \qquad (5.4.7)$$

Hence, the maximum of the permeability depends on the coverage, the thickness of the membrane as well as on the feed concentration of the diffusing substance. Consequently, the number of free vacancies increases with the membrane thickness because the molecular flux is decreasing and thus, the maximum of the flux is reached

at lower temperatures. It has been also observed that the maximum permeability temperature decreases with decreasing feed concentration due to lower surface coverage at decreased feed concentrations [175]. In the system examined, the maximum permeance of benzene is below 313 K whereas the maximum of p-xylene seems to be above 403 K. This is once more an effect of the higher surface coverage of p-xylene in comparison to benzene [175].

5.5. *Conclusions*

The transport characteristics of benzene and p-xylene in MFI change significantly between single particles, pressed pellets and grown membranes. In isolated particles, diffusion can be described by the Fickian law resulting in a faster diffusion of benzene compared to p-xylene. A different transport mechanism occurs in pressed pellets, where the uptake into the bulk is controlled by a combination of micro- and mesoporous diffusion. The transient transport behavior of benzene and p-xylene in a pellet depends on its adsorption capacity, while the steady state permeability is solely controlled by Knudsen diffusion in the mesopores leading to identical permeances for benzene and p-xylene (independent of the temperature or the pellet thickness). Under these conditions the pressed pellets behave like a (classical) bed adsorber and do not allow a separation of these molecules.

On the Silicalite-1 membrane, the permeabilities are in general two orders of magnitude lower compared to the pressed pellet. In contrast to the pressed pellets, the transport under transient and steady state conditions can be described by the Stefan Maxwell model. The transient behavior of mixtures of benzene and p-xylene showed a strong temperature dependency and is controlled by a combination of adsorption and micropore diffusion. The enhanced permeability of p-xylene compared to benzene at steady state conditions allows an enrichment of p-xylene in the effluent stream.

This work shows that in transport processes a pellet can be understood as an analogue of an extrudate. Consequently, the transport processes observed can be readily extended to the application of hierarchical materials for diffusion controlled separations and reactions. The steady state flux is only controlled by the diffusion in the mesopores, while the sorption equilibrium over the individual particles is established. Therefore, the sorption properties of the particles do not influence the

overall transport characteristics in the pellet. The transport through the micropores of a membrane, in contrast, is controlled by configurational diffusion at low partial pressure (or coverage), which allows the separation of the aromatic molecules. Unfortunately the transport in the mixture changes to single file diffusion at high loadings, where the permeability is controlled by the flux of the slower diffusing molecules. Therefore, the separation in the industrial relevant pressure range is limited, which narrows the applicability of membrane separation techniques.

Chapter 6

Conclusions

The mass transport in mesoscale organized zeolites is controlled by a highly complex, interconnected network of parallel and consecutive elementary steps. Its understanding on all length scales is very difficult as it is highly dynamic and influenced by a large amount of different parameters, which are sterical, e.g. pore diameter and particle size, but also of energetic nature, e.g. heat of adsorption. This thesis aims to elucidate the effect of each of the different parameters on the transport of aromatics and aliphatics and mixtures of both in nano-sized, mesoscale organized MFI on molecular, primary and secondary particle level by using a variety of experimental techniques. Under those, fast time resolved infrared spectroscopy and permeation measurements using the Wicke-Kallenbach method were most prominent.

A network was identified, which describes the transport from the gas phase to the sorption sites within the zeolite channel system via the collision and adsorption at the external surface, the pore entrance step and the intracrystalline diffusion. In small crystal materials the adsorption at the external surface and subsequent pore entering are rate limiting. Hence, alteration of the transport by epitaxial growth of a mesoporous silica overlayer becomes feasible, which selectifies the sorption rate towards molecules with a high heat of adsorption on silica and a low steric demand (see Chapter 3).

In industrial applications of MFI zeolites, e.g. in petrochemical processes, however, mixtures of aromatics and aliphatics are present. As a consequence, the presence of aromatics results in a competitive adsorption with the aliphatic molecules at the external surface slightly reducing the sorption rate of the latter. On the other hand, occupation of the sites near the pore mouth by light hydrocarbon molecules (window blockage)

significantly hinders the transport of benzene compared to the single component (see Chapter 4).

In addition, zeolitic catalysts are formed into secondary particles for the use in industrial scale reactors in order to design the fluid dynamics, limit the pressure drop and increase the mechanical stability. However, this may also alter the overall transport properties by shifting the rate determining step towards the newly formed pores. Hence, tailored sorption properties on the primary particle level are losing their impact on the macroscopic rates. In such cases, designing the shape of the formed particles is crucial to reduce the mass transport limitation in the secondary pore structure and, thus, maintain the intrinsic activity and selectivity of the catalyst (see Chapter 5).

Chapter 7

Zusammenfassung

Die vorliegende Arbeit beschäftigt sich mit der Analyse von Massentransportprozessen in mikro/ -mesoporösen Materialien am Beispiel von mesoskopisch geordneten MFI Zeolithen. Diese besitzen neben dem dreidimensionalen System aus sich kreuzenden, geraden und sinusidal verlaufenden Mikroporen der MFI Struktur ein damit verbundenes, sekundäres System aus größeren (Meso)Poren, welches entweder durch Agglomeration der Primärpartikel oder durch postsynthetische Modifikation der externen Oberfläche (Flüssigphasenabscheidung von Tetraethylorthosilikat) ausgebildet werden kann. Folglich wird der diffusive Stofftransport am besten durch ein Netzwerk von miteinander verbundenen, konsekutiv und parallel ablaufenden Elementarreaktionen beschrieben und weist eine entsprechend große Zahl von Modellparametern auf. Diese können sowohl sterischer (Porenradius, Partikelgröße) als auch energetischer (Adsorptionwärme) Natur sein. Im Rahmen dieser Arbeit sollen die Abhängigkeiten der Parameter zueinander, aber auch deren Einfluss auf den mikro-, meso- und makroskopischen Stofftransport untersucht werden. Der experimentelle Fokus der Arbeit liegt auf der Verwendung von moderner, zeitaufgelöster Infrarotspektroskopie (Primärpartikelebene) und Permeationsexperimenten entsprechend der Technik von Wicke und Kallenbach (Presslinge).

Auf Primärpartikelebene konnte ein Transportnetzwerk identifiziert werden, welches die Adsorption in einen präadsorbierten Zustand an der äußeren Oberfläche, den Poreneintrittsschritt und die intrakristalline Diffusion beinhaltet. Außerdem war eine Differenzierung der Sorbatkonzentrationen an der äußeren Oberfläche und im Poreninneren aufgrund von signifikant unterschiedlichen molaren

Extinktionskoeffizienten möglich. Hierdurch konnte die Anwesenheit des postulierten präadsorbierten Zustands spektroskopisch belegt werden. Weiterhin waren durch Anwendung des beschriebenen Modells auf die experimentell bestimmten Konzentrationsprofile alle Transportraten und Ratenkonstanten direkt zugänglich. Es sei angemerkt, dass die Bestimmung der Kinetik der Oberflächenprozesse nur dann möglich ist, wenn letztere ratenbestimmend sind. Dies ist in den verwendeten nanokristallinen MFI Zeolithen gegeben. Durch einen Vergleich der Ergebnisse an Proben mit und ohne postsynthetischer Oberflächenmodifizierung konnte bewiesen werden, dass die Adsorptionswärme des Sorbats an der äußeren Oberfläche und dessen sterischer Anspruch die determinierenden Parameter des externen Transportwiderstands sind. Außerdem konnte der Effekt des mesoporösen Siliziumdioxidüberzugs eindeutig geklärt werden. Es zeigte sich, dass dieser zwar durch blockieren von einem Teil der Porenöffnungen die Wahrscheinlichkeit eines Poreneintritts vermindert, auf der anderen Seite aber das Sorbat an der externen Oberfläche aufkonzentriert. Letzteres erklärt sich durch eine größere Anzahl an Adsorptionsplätzen und zusätzlich einer höheren Adsorptionswärme verglichen zur unmodifizierten Oberfläche. Folglich ist die Sorptionsgeschwindigkeit nach der Oberflächenmodifizierung selektiver für Moleküle mit einer hohen Adsorptionswärme und einem kleinen sterischen Anspruch

Da Reaktionsmischungen in der industriellen Katalyse stets aus mehr als einer Komponente bestehen, wurde die Kinetik der Koadsorption von Aliphaten in Anwesenheit von Benzol in MFI Zeolithen genauer untersucht. Es konnte gezeigt werden, dass Benzol die Sorptionsrate von leichten Kohlenwasserstoffen durch eine Konkurrenzadsorption an der externen Oberfläche herabsetzt. Auf der anderen Seite hatte die Anwesenheit der leichten Kohlenwasserstoffe eine dramatische Reduzierung der Benzoltransportrate zur Folge, welche mit abnehmender Kettenlänge und höherer Aliphatenkonzentration zunahm. Hierfür können primär zwei Effekte verantwortlich gemacht werden: zum einen ist die Wahrscheinlichkeit der Adsorption eines aliphatischen Moleküls an einem porennahen Zentrum aufgrund einer homogeneren Verteilung der Adsorptionswärme über den Partikelradius größer, zum anderen ist dessen Sorptionsrate höher und die relative intrakristalline Konzentration (im Vergleich zu Benzol) nimmt zu Beginn des Experiments zu. Entsprechend sinkt die

Wahrscheinlichkeit eines erfolgreichen Sorptionsvorgangs für Benzol, da mehr und mehr Zentren im Porenmund blockiert sind (Window Blockage).

Ein weiterer Punkt, den es bei der großtechnischen Verwendung von mikroporösen Katalysatoren zu beachten gilt, ist die mögliche Beeinflussung der Transporteigenschaften durch Verformung der Primärpartikel zu sekundären Einheiten (z.B. durch Extrudieren). Um deren Auswirkungen auf die makroskopischen Transporteigenschaften zu ermitteln, wurden Permeationsexperimente von Benzol/ p-Xylol Mischungen in gepressten MFI Wafer durchgeführt. Am Verlauf der Durchbruchskurven zeigte sich eindeutig, dass die Primärpartikel zu jedem Zeitpunkt des Experiments mit der Sorbatkonzentration in der angrenzenden Mesopore equilibriert waren. Hieraus kann geschlussfolgert werden, dass sich der ratenbestimmende Schritt des Gesamttransportnetzwerks hin zu einer Knudsen-artigen Diffusion in der Mesopore verschoben hat. Diese Schlussfolgerung wurde durch die Messung der Sorptionskinetik an einer gepressten Probe bestätigt. Da sich die Diffusionskoeffizienten innerhalb der Mesoporen nur anhand der Masse der Sorbats unterscheiden, ergeben sich bei vielen Reaktionen gleiche (Xylol Isomerisierung) oder sehr ähnliche (Toluol Methylierung) Transportraten. Die Konsequenz hieraus ist der Verlust der intrinsischen Formselektivität des mikroporösen Katalysators und eine Verminderung der Reaktionsrate. Dies macht einmal mehr die Notwendigkeit eines sorgfältigen Sekundärpartikeldesigns und der entsprechenden Porenstruktur deutlich.

References

1.	Corma, A., *Inorganic Solid Acids and Their Use in Acid-Catalyzed Hydrocarbon Reactions.* Chemical Reviews, 1995. **95**(3): p. 559-614.

2.	Meisel, S.L., et al., *Gasoline from Methanol in One-Step.* Chemtech, 1976. **6**(2): p. 86-89.

3.	Degnan, T.F., G.K. Chitnis, and P.H. Schipper, *History of ZSM-5 fluid catalytic cracking additive development at Mobil.* Microporous and Mesoporous Materials, 2000. **35-6**: p. 245-252.

4.	Young, L.B., S.A. Butter, and W.W. Kaeding, *Shape Selective Reactions with Zeolite Catalysts 3. Selectivity in Xylene Isomerization, Toluene Methanol Alkylation, and Toluene Disproportionation over ZSM-5 Zeolite Catalysts.* Journal of Catalysis, 1982. **76**(2): p. 418-432.

5.	Weitkamp, J., et al., *Direct conversion of aromatics into a synthetic steamcracker feed using bifunctional zeolite catalysts.* Chemical Communications, 2000(13): p. 1133-1134.

6.	Weisz, P.B., *Molecular Shape Selective Catalysis.* Pure and Applied Chemistry, 1980. **52**(9): p. 2091-2103.

7.	Klemm, E., J.G. Wang, and G. Emig, *A study of shape selectivity in ethylation/disproportionation of ethylbenzene on ZSM-5 zeolites using a continuum and a Monte Carlo method.* Chemical Engineering Science, 1997. **52**(18): p. 3173-3182.

8.	Klemm, E. and G. Emig, *A method for the determination of diffusion coefficients in product-shape-selective catalysis on zeolites under reaction conditions.* Chemical Engineering Science, 1997. **52**(23): p. 4329-4344.

9.	Csicsery, S.M., *Catalysis by Shape Selective Zeolites - Science and Technology.* Pure and Applied Chemistry, 1986. **58**(6): p. 841-856.

10.	Butler, A.C. and C.P. Nicolaides, *Catalytic Skeletal Isomerization of Linear Butenes to Isobutene.* Catalysis Today, 1993. **18**(4): p. 443-471.

11.	Yashima, T., et al., *Alkylation on Synthetic Zeolites 1. Alkylation of Toluene with Methanol.* Journal of Catalysis, 1970. **16**(3): p. 273-&.

12. Tsai, T.C., S.B. Liu, and I.K. Wang, *Disproportionation and transalkylation of alkylbenzenes over zeolite catalysts.* Applied Catalysis A-General, 1999. **181**(2): p. 355-398.

13. Sun, X.D., et al., *The role of acid strength of zeolites in liquid-phase alkylation of benzene with ethylene.* Catalysis Letters, 2004. **94**(1-2): p. 75-79.

14. Stocker, M., H. Mostad, and T. Rorvik, *Isobutane 2-Butene Alkylation on Faujasite-Type Zeolites (H-EMT and H-FAU).* Catalysis Letters, 1994. **28**(2-4): p. 203-209.

15. Mirth, G. and J.A. Lercher, *On the Role of Product Isomerization for Shape-Selective Toluene Methylation over HZSM5.* Journal of Catalysis, 1994. **147**(1): p. 199-206.

16. Ivanova, I.I. and A. Corma, *An in situ C-13 MAS NMR study of toluene alkylation with methanol over H-ZSM-11.* Zeolites: A Refined Tool for Designing Catalytic Sites, 1995. **97**: p. 27-34.

17. Caeiro, G., et al., *Activation of C-2-C-4 alkanes over acid and bifunctional zeolite catalysts.* Journal of Molecular Catalysis A-Chemical, 2006. **255**(1-2): p. 131-158.

18. Long, R.Q. and R.T. Yang, *Superior Fe-ZSM-5 catalyst for selective catalytic reduction of nitric oxide by ammonia.* Journal of the American Chemical Society, 1999. **121**(23): p. 5595-5596.

19. Caro, J., et al., *Zeolite membranes - state of their development and perspective.* Microporous and Mesoporous Materials, 2000. **38**(1): p. 3-24.

20. Cronstedt, A.F., *Ron och beskrifning om en oberkant bärg art, som kallas zeolites.* Kongl. Vetenskaps Acad. Handl. 1756, Stockholm.

21. *Database of Zeolite Structures*.

22. *IUPAC Compendium of Chemical Terminology*. Research Triangle Park, NC: International Union of Pure and Applied Chemistry.

23. Baerlocher, C., W.M. Meier, and D.H. Olson, *Atlas of Zeolite Framework Types*. 5 ed. 2001: Elsevier.

24. Meier, W.M. and C. Baerlocher, *Zeolite Type Frameworks: Connectivities, Configurations and Conformations*, in *Structures and Structure Determination*, C. Baerlocher, et al., Editors. 1999, Springer Berlin Heidelberg. p. 141-161.

25. 2013; Available from: http://www.iza-online.org.

26. Weitkamp, J., *Zeolites and catalysis.* Solid State Ionics, 2000. **131**(1-2): p. 175-188.

27. Davis, M.E. and R.F. Lobo, *Zeolite and Molecular-Sieve Synthesis.* Chemistry of Materials, 1992. **4**(4): p. 756-768.

28. Lowenstein, W., American Mineralogist, 1954. **39**: p. 92.

29. Weisz, P.B. and V.J. Frilette, *Intracrystalline and Molecular-Shape-Selective Catalysis by Zeolite Salts.* Journal of Physical Chemistry, 1960. **64**(3): p. 382-382.

30. Smit, B. and T.L.M. Maesen, *Towards a molecular understanding of shape selectivity.* Nature, 2008. **451**(7179): p. 671-678.

31. Keil, F.J., R. Krishna, and M.O. Coppens, *Modeling of diffusion in zeolites.* Reviews in Chemical Engineering, 2000. **16**(2): p. 71-197.

32. Menoufy, M.F., A.E. Nadia, and H.S. Ahmed, *Catalytic Dewaxing for Lube Oil Production.* Petroleum Science and Technology, 2009. **27**(6): p. 568-574.

33. Beck, J.S., et al., *A New Family of Mesoporous Molecular-Sieves Prepared with Liquid-Crystal Templates.* Journal of the American Chemical Society, 1992. **114**(27): p. 10834-10843.

34. Zhao, D.Y., et al., *Triblock copolymer syntheses of mesoporous silica with periodic 50 to 300 angstrom pores.* Science, 1998. **279**(5350): p. 548-552.

35. Perez-Ramirez, J., et al., *Hierarchical zeolites: enhanced utilisation of microporous crystals in catalysis by advances in materials design.* Chemical Society Reviews, 2008. **37**(11): p. 2530-2542.

36. Mitchell, S., et al., *Visualization of hierarchically structured zeolite bodies from macro to nano length scales.* Nature Chemistry, 2012. **4**(10): p. 825-831.

37. Neimark, A.V., et al., *Pore size analysis of MCM-41 type adsorbents by means of nitrogen and argon adsorption.* Journal of Colloid and Interface Science, 1998. **207**(1): p. 159-169.

38. Sayari, A., *Catalysis by crystalline mesoporous molecular sieves.* Chemistry of Materials, 1996. **8**(8): p. 1840-1852.

39. Moller, K. and T. Bein, *Inclusion chemistry in periodic mesoporous hosts.* Chemistry of Materials, 1998. **10**(10): p. 2950-2963.

40. Maschmeyer, T., et al., *Heterogeneous Catalysts Obtained by Grafting Metallocene Complexes onto Mesoporous Silica.* Nature, 1995. **378**(6553): p. 159-162.

41. Lim, M.H. and A. Stein, *Comparative studies of grafting and direct syntheses of inorganic-organic hybrid mesoporous materials.* Chemistry of Materials, 1999. **11**(11): p. 3285-3295.

42. Ciesla, U. and F. Schuth, *Ordered mesoporous materials.* Microporous and Mesoporous Materials, 1999. **27**(2-3): p. 131-149.

43. Zhao, X.S., et al., *Synthesis and characterization of highly ordered MCM-41 in an alkali-free system and its catalytic activity.* Catalysis Letters, 1996. **38**(1-2): p. 33-37.

44. Zhao, X.S., G.Q.M. Lu, and G.J. Millar, *Advances in mesoporous molecular sieve MCM-41.* Industrial & Engineering Chemistry Research, 1996. **35**(7): p. 2075-2090.

45. Kim, J.M., et al., *Ion-Exchange and Thermal-Stability of MCM-41.* Journal of Physical Chemistry, 1995. **99**(45): p. 16742-16747.

46. Ryoo, R. and S. Jun, *Improvement of hydrothermal stability of MCM-41 using salt effects during the crystallization process.* Journal of Physical Chemistry B, 1997. **101**(3): p. 317-320.

47. Melero, J.A., R. van Grieken, and G. Morales, *Advances in the synthesis and catalytic applications of organosulfonic-functionalized mesostructured materials.* Chemical Reviews, 2006. **106**(9): p. 3790-3812.

48. Lakes, R., *Materials with Structural Hierarchy.* Nature, 1993. **361**(6412): p. 511-515.

49. Egeblad, K., et al., *Templating mesoporous zeolites.* Chemistry of Materials, 2008. **20**(3): p. 946-960.

50. Groen, J.C., et al., *Mechanism of hierarchical porosity development in MFI zeolites by desilication: The role of aluminium as a pore-directing agent.* Chemistry-A European Journal, 2005. **11**(17): p. 4983-4994.

51. Shetti, V.N., et al., *Assessment of the mesopore wall catalytic activities of MFI zeolite with mesoporous/microporous hierarchical structures.* Journal of Catalysis, 2008. **254**(2): p. 296-303.

52. van Donk, S., et al., *Generation, characterization, and impact of mesopores in zeolite catalysts.* Catalysis Reviews-Science and Engineering, 2003. **45**(2): p. 297-319.

53. Perez-Ramirez, J., *Zeolite Nanosystems Imagination has no limits.* Nature Chemistry, 2012. **4**(4): p. 250-251.

54. Christensen, C.H., et al., *Mesoporous zeolite single crystal catalysts: Diffusion and catalysis in hierarchical zeolites.* Catalysis Today, 2007. **128**(3-4): p. 117-122.

55. Groen, J.C., et al., *Direct demonstration of enhanced diffusion in mesoporous ZSM-5 zeolite obtained via controlled desilication.* Journal of the American Chemical Society, 2007. **129**(2): p. 355-360.

56. Christensen, C.H., et al., *Catalytic benzene alkylation over mesoporous zeolite single crystals: Improving activity and selectivity with a new family of porous materials.* Journal of the American Chemical Society, 2003. **125**(44): p. 13370-13371.

57. Christensen, C.H., et al., *Crystals in crystals-nanocrystals within mesoporous zeolite single crystals.* Journal of the American Chemical Society, 2005. **127**(22): p. 8098-8102.

58. Kustov, A.L., et al., *Selective catalytic reduction of NO by ammonia using mesoporous Fe-containing HZSM-5 and HZSM-12 zeolite catalysts: An option for automotive applications.* Applied Catalysis B-Environmental, 2007. **76**(3-4): p. 311-319.

59. Kustova, M.Y., P. Hasselriis, and C.H. Christensen, *Mesoporous MEL-type zeolite single crystal catalysts.* Catalysis Letters, 2004. **96**(3-4): p. 205-211.

60.   Kustova, M.Y., et al., *Direct NO decomposition over conventional and mesoporous Cu-ZSM-5 and Cu-ZSM-11 catalysts: Improved performance with hierarchical zeolites.* Applied Catalysis B-Environmental, 2006. **67**(1-2): p. 60-67.

61.   Schmidt, I., et al., *Catalytic epoxidation of alkenes with hydrogen peroxide over first mesoporous titanium-containing zeolite.* Chemical Communications, 2000(21): p. 2157-2158.

62.   Langmuir, I., *The Constitution and Fundamental Properties of Solids and Liquids. Part I. Solids.* Journal of the American Chemical Society, 1916. **38**(11): p. 2221-2295.

63.   Logan, S.R., *Fundamentals of Chemical Kinetics.* 1996, Essex, England: Longman Group Limited.

64.   Krishna, R., T.J.H. Vlugt, and B. Smit, *Influence of isotherm inflection on diffusion in silicalite.* Chemical Engineering Science, 1999. **54**(12): p. 1751-1757.

65.   Micke, A., et al., *Sorbate immobilization in molecular-sieves - rate-limiting step for n-hexane uptake by silicalite-1.* Journal of Physical Chemistry, 1994. **98**(47): p. 12337-12344.

66.   Song, L.J. and L.V.C. Rees, *Adsorption and transport of n-hexane in silicalite-1 by the frequency response technique.* Journal of the Chemical Society-Faraday Transactions, 1997. **93**(4): p. 649-657.

67.   Vlugt, T.J.H., R. Krishna, and B. Smit, *Molecular simulations of adsorption isotherms for linear and branched alkanes and their mixtures in silicalite.* Journal of Physical Chemistry B, 1999. **103**(7): p. 1102-1118.

68.   Atkins, P.W., *Physical Chemistry.* Fifth ed. 1994: Oxford University Press.

69.   Brunauer, S., P.H. Emmett, and E. Teller, *Adsorption of Gases in Multimolecular Layers.* Journal of the American Chemical Society, 1938. **60**(2): p. 309-319.

70.   Sing, K.S.W., et al., *Reporting Physisorption Data for Gas Solid Systems with Special Reference to the Determination of Surface-Area and Porosity (Recommendations 1984).* Pure and Applied Chemistry, 1985. **57**(4): p. 603-619.

71.   Rouquerol, F., J. Rouquerol, and K.S.W. Sing, *Adsorption by powder and porous solids.* 1998: Academic Press.

72. Lippens, B.C. and J.H. Deboer, *Studies on Pore Systems in Catalysts .V. T Method.* Journal of Catalysis, 1965. **4**(3): p. 319-&.

73. Sing, K.S.W., *Surface Area Determination.* 1970, London: Butterworths.

74. Jaroniec, M., M. Kruk, and J.P. Olivier, *Standard nitrogen adsorption data for characterization of nanoporous silicas.* Langmuir, 1999. **15**(16): p. 5410-5413.

75. Reitmeier, S.J., et al., *Enhancement of Sorption Processes in the Zeolite H-ZSM5 by Postsynthetic Surface Modification.* Angewandte Chemie-International Edition, 2009. **48**(3): p. 533-538.

76. Barrett, E.P., L.G. Joyner, and P.P. Halenda, *The Determination of Pore Volume and Area Distributions in Porous Substances 1. Computations from Nitrogen Isotherms.* Journal of the American Chemical Society, 1951. **73**(1): p. 373-380.

77. Neimark, A.V., et al., *Quenched solid density functional theory and pore size analysis of micro-mesoporous carbons.* Carbon, 2009. **47**(7): p. 1617-1628.

78. Thommes, M., et al., *Adsorption hysteresis of nitrogen and argon in pore networks and characterization of novel micro- and mesoporous silicas.* Langmuir, 2006. **22**(2): p. 756-764.

79. Ruthven, D.M., *Chapter 21 Diffusion in zeolite molecular sieves*, in *Studies in Surface Science and Catalysis*, H.v.B.A.C. J. Čejka and F. Schüth, Editors. 2007, Elsevier. p. 737-785.

80. Chmelik, C. and J. Karger, *In situ study on molecular diffusion phenomena in nanoporous catalytic solids.* Chemical Society Reviews, 2010. **39**(12): p. 4864-4884.

81. Karger, J., *NMR Self-Diffusion Studies in Heterogeneous Systems.* Advances in Colloid and Interface Science, 1985. **23**(1-4): p. 129-148.

82. Karger, J., *Random-Walk through 2-Channel Networks - A Simple Means to Correlate the Coefficients of Anisotropic Diffusion in ZSM-5 Type Zeolites.* Journal of Physical Chemistry, 1991. **95**(14): p. 5558-5560.

83. Jobic, H. and D.N. Theodorou, *Quasi-elastic neutron scattering and molecular dynamics simulation as complementary techniques for studying diffusion in zeolites.* Microporous and Mesoporous Materials, 2007. **102**(1-3): p. 21-50.

84.   Brandani, S., J. Hufton, and D. Ruthven, S*elf-diffusion of propane and propylene in 5A and 13X zeolite crystals studied by the tracer ZLC method.* Zeolites, 1995. **15**(7): p. 624-631.

85.   Combariza, A.F., G. Sastre, and A. Corma, *Molecular Dynamics Simulations of the Diffusion of Small Chain Hydrocarbons in 8-Ring Zeolites.* Journal of Physical Chemistry C, 2011. **115**(4): p. 875-884.

86.   Sastre, G., et al., *Selective diffusion of C8 aromatics in a 10 and 12 MR zeolite. A molecular dynamics study.* Journal of Physical Chemistry B, 1998. **102**(17): p. 3198-3209.

87.   Hibbe, F., et al., *The Nature of Surface Barriers on Nanoporous Solids Explored by Microimaging of Transient Guest Distributions.* Journal of the American Chemical Society, 2011. **133**(9): p. 2804-2807.

88.   Chmelik, C., et al., *Adsorption and diffusion of alkanes in CuBTC crystals investigated using infra-red microscopy and molecular simulations.* Microporous and Mesoporous Materials, 2009. **117**(1-2): p. 22-32.

89.   Geier, O., et al., *Interference microscopy investigation of the influence of regular intergrowth effects in MFI-type zeolites on molecular uptake.* Journal of Physical Chemistry B, 2001. **105**(42): p. 10217-10222.

90.   Muller, G., et al., *Infrared Microscopic Study of Sorption and Diffusion of Toluene in ZSM-5.* Journal of Physical Chemistry, 1994. **98**(31): p. 7436-7439.

91.   Schemmert, U., J. Karger, and J. Weitkamp, *Interference microscopy as a technique for directly measuring intracrystalline transport diffusion in zeolites.* Microporous and Mesoporous Materials, 1999. **32**(1-2): p. 101-110.

92.   Zheng, S.R., A. Jentys, and J.A. Lercher, *Xylene isomerization with surface-modified HZSM-5 zeolite catalysts: An in situ IR study.* Journal of Catalysis, 2006. **241**(2): p. 304-311.

93.   Ruthven, D.M., M. Eic, and E. Richard, *Diffusion of C-8 Aromatic-Hydrocarbons in Silicalite.* Zeolites, 1991. **11**(7): p. 647-653.

94.   Gobin, O.C., et al., *Comparison of the Transport of Aromatic Compounds in Small and Large MFI Particles.* Journal of Physical Chemistry C, 2009. **113**(47): p. 20435-20444.

95. Rees, L.V.C. and L. Song, *Recent Advances in Gas Separation by Microporous Ceramic Membranes*. Frequency Response Method for the Characterisation of Microporous Solids. 2000: Elsevier Science B.V.

96. Shen, D.M. and L.V.C. Rees, *Diffusivities of Benzene in HZSM-5, Silicalite-1, and NaX Determined by Frequency-Response Techniques*. Zeolites, 1991. **11**(7): p. 666-671.

97. Yasuda, Y., *Frequency-Response Method for Investigation of Gas-Surface Dynamic Phenomena*. Heterogeneous Chemistry Reviews, 1994. **1**(2): p. 103-124.

98. Petkovska, M., *Nonlinear FR-ZLC method for investigation of adsorption equilibrium and kinetics*. Adsorption-Journal of the International Adsorption Society, 2008. **14**(2-3): p. 223-239.

99. Kolvenbach, R., et al., *A comparative study of diffusion of benzene/p-xylene mixtures in MFI particles, pellets and grown membranes*. Catalysis Today, 2011. **168**(1): p. 147-157.

100. Wicke, E. and R. Kallenbach, *Die Oberflächendiffusion von Kohlendioxyd in aktiven Kohlen*. Kolloid-Zeitschrift, 1941. **97**(2): p. 135-151.

101. Baertsch, C.D., et al., *Permeation of aromatic hydrocarbon vapors through silicalite-zeolite membranes*. Journal of Physical Chemistry, 1996. **100**(18): p. 7676-7679.

102. Jeong, B.H., et al., *Permeation of binary mixtures of benzene and saturated C-4-C-7 hydrocarbons through an FAU-type zeolite membrane*. Journal of Membrane Science, 2003. **213**(1-2): p. 115-124.

103. Forste, C., et al., *Comparison of nuclear-magnetic-resonance tracer exchange and molecular uptake of benzene on Pentasils*. Journal of the Chemical Society-Faraday Transactions, 1990. **86**(5): p. 881-885.

104. Gratz, M., et al., *Mixture diffusion of adsorbed organic compounds in metal-organic frameworks as studied by magic-angle spinning pulsed-field gradient nuclear magnetic resonance*. New Journal of Physics, 2011. **13**.

105. Karger, J., M. Bulow, and P. Lorenz, *NMR self-diffusion measurements in normal-heptane-benzene mixtures adsorbed on NaX-zeolites*. Journal of Colloid and Interface Science, 1978. **65**(1): p. 181-185.

106. Karge, H.G., *Infrared spectroscopic investigation of diffusion, co-diffusion and counter-diffusion of hydrocarbon molecules in zeolites.* Comptes Rendus Chimie, 2005. **8**(3–4): p. 303-319.

107. Krishna, R., *Multicomponent surface-diffusion of adsorbed species - a description based on the generalized Maxwell-Stefan equations.* Chemical Engineering Science, 1990. **45**(7): p. 1779-1791.

108. Krishna, R. and D. Paschek, *Separation of hydrocarbon mixtures using zeolite membranes: a modelling approach combining molecular simulations with the Maxwell-Stefan theory.* Separation and Purification Technology, 2000. **21**(1-2): p. 111-136.

109. Krishna, R. and G.L. Standart, *Mass and energy-transfer in multicomponent systems.* Chemical Engineering Communications, 1979. **3**(4-5): p. 201-275.

110. Krishna, R. and J.M. van Baten, *Diffusion of hydrocarbon mixtures in MFI zeolite: Influence of intersection blocking.* Chemical Engineering Journal, 2008. **140**(1-3): p. 614-620.

111. Sastre, G., C.R.A. Catlow, and A. Corma, *Diffusion of benzene and propylene in MCM-22 zeolite. A molecular dynamics study.* Journal of Physical Chemistry B, 1999. **103**(25): p. 5187-5196.

112. Daramola, M.O., et al., *Nanocomposite MFI-ceramic hollow fibre membranes via pore-plugging synthesis: Prospects for xylene isomer separation.* Journal of Membrane Science, 2009. **337**(1-2): p. 106-112.

113. Deng, Z., et al., *Nanocomposite MFI-alumina hollow fibre membranes prepared via pore-plugging synthesis: Influence of the porous structure of hollow fibres on the gas/vapour separation performance.* Journal of Membrane Science, 2010. **364**(1-2): p. 1-8.

114. Gump, C.J., R.D. Noble, and J.L. Falconer, *Separation of hexane isomers through nonzeolite pores in ZSM-5 zeolite membranes.* Industrial & Engineering Chemistry Research, 1999. **38**(7): p. 2775-2781.

115. Keizer, K., et al., *Two component permeation through thin zeolite MFI membranes.* Journal of Membrane Science, 1998. **147**(2): p. 159-172.

116. Lee, J.B., et al., *Adsorption-induced expansion of defects in MFI membranes.* Journal of Membrane Science, 2009. **341**(1-2): p. 238-245.

117. Sakai, H., T. Tomita, and T. Takahashi, *P-xylene separation with MFI-type zeolite membrane.* Separation and Purification Technology, 2001. **25**(1-3): p. 297-306.

118. Crank, J., *The Mathematics of Diffusion.* 2 ed. 1975, Oxford: Oxford University Press.

119. Krishna, R. and J.A. Wesselingh, *Review article number 50 - The Maxwell-Stefan approach to mass transfer.* Chemical Engineering Science, 1997. **52**(6): p. 861-911.

120. Rehfeldt, S. and J. Stichlmair, *Measurement and calculation of multicomponent diffusion coefficients in liquids.* Fluid Phase Equilibria, 2007. **256**(1-2): p. 99-104.

121. Taylor, R. and R. Krishna, *Multicomponent Mass Transfer.* Wiley Series in Chemical Engineering. 1993, New York: John Wiley&Sons Inc.

122. Skoulidas, A.I. and D.S. Sholl, *Kinetics of hard sphere and chain adsorption into circular and elliptical pores.* Journal of Chemical Physics, 2000. **113**(10): p. 4379-4387.

123. Baerns, M., et al., *Technische Chemie.* 2006, Weinheim: Wiley-VCH Verlag GmbH&Co KGaA.

124. Welty, J.R., et al., *Fundamentals of Momentum, Heat, and Mass Transfer.* 5 ed. 2008, Hoboken: John Wiley&Sons Inc.

125. Deboer, J.H., *The Dynamical Character of Adsorption.* 2 ed. 1969, London: Oxford University Press.

126. Gillilan, E.R., et al., *Diffusion on Surfaces. 1. Effect of Concentration on Diffusivity of Physically Adsorbed Gases.* Industrial & Engineering Chemistry Fundamentals, 1974. **13**(2): p. 95-100.

127. Skoulidas, A.I. and D.S. Sholl, *Self-diffusion and transport diffusion of light gases in metal-organic framework materials assessed using molecular dynamics simulations.* Journal of Physical Chemistry B, 2005. **109**(33): p. 15760-15768.

128. Hahn, K., J. Karger, and V. Kukla, *Single-file diffusion observation.* Physical Review Letters, 1996. **76**(15): p. 2762-2765.

129. Karger, J., et al., *Single-File Diffusion and Reaction in Zeolites.* Journal of Catalysis, 1992. **136**(2): p. 283-299.

130. Kukla, V., et al., *NMR studies of single-file diffusion in unidimensional channel zeolites.* Science, 1996. **272**(5262): p. 702-704.

131. Kärger, J. and D.M. Ruthven, *Diffusion in zeolites and other microporous solids.* 1992, New York: John Wiley & Sons, Inc.

132. Kärger, J., *Handbook of heterogeneous catalysis.* Determination of diffusion coefficients in porous media, ed. G. Ertl, H. Knözinger, and J. Weitkamp. 1997, Weinheim: VCH.

133. Kärger, J., S. Vasenkov, and S.M. Auerbach, *Handbook of zeolite catalysts and microporous materials.* Diffusion in zeolites, ed. S.M. Auerbach, K.A. Carrado, and P.K. Dutta. 2002, New York: Marcel Dekker.

134. Evnochid.Sk and E.J. Henley, *Simultaneous Measurement of Vapor Diffusion and Solubility Coefficients in Polymers by Frequency Response Techniques.* Journal of Polymer Science Part A-2-Polymer Physics, 1970. **8**(11): p. 1987-&.

135. Gobin, O.C., et al., *Diffusion pathways of benzene, toluene and p-xylene in MFI.* Microporous and Mesoporous Materials, 2009. **125**(1-2): p. 3-10.

136. Hansen, N., *The CMA evolution strategy: a comparing review*, in *Towards a New Evolutionary Computation. Advances on Estimation of Distribution Algorithms*, J.A. Lozano, et al., Editors. 2006, Springer: New York. p. 75.

137. Gobin, O.C., et al., *Role of the Surface Modification on the Transport of Hexane Isomers in ZSM-5.* Journal of Physical Chemistry C, 2011. **115**(4): p. 1171-1179.

138. Reitmeier, S.J., et al., *Influence of Postsynthetic Surface Modification on Shape Selective Transport of Aromatic Molecules in HZSM-5.* Journal of Physical Chemistry C, 2009. **113**(34): p. 15355-15363.

139. Reitmeier, S.J., et al., *Surface transport processes and sticking probability of aromatic molecules in HZSM-5.* Journal of Physical Chemistry C, 2008. **112**(7): p. 2538-2544.

140. Chen, Y.D. and R.T. Yang, *Predicting binary Fickian diffusivities from pure-component Fickian diffusivities for surface-diffusion.* Chemical Engineering Science, 1992. **47**(15-16): p. 3895-3905.

141.   Chen, Y.D., R.T. Yang, and L.M. Sun, *Further work on predicting multicomponent diffusivities from pure-component diffusivities for surface-diffusion and diffusion in zeolites.* Chemical Engineering Science, 1993. **48**(15): p. 2815-2816.

142.   Sikavitsas, V.I. and R.T. Yang, *Predicting multicomponent diffusivities for diffusion on surfaces and in molecular-sieves with energy heterogeneity.* Chemical Engineering Science, 1995. **50**(19): p. 3057-3065.

143.   Vignes, A., *Diffusion in binary solutions - variation of diffusion coefficient with composition.* Industrial & Engineering Chemistry Fundamentals, 1966. **5**(2): p. 189-&.

144.   Ruthven, D.M., L.K. Lee, and H. Yucel, *Kinetics of Non-Isothermal Sorption in Molecular-Sieve Crystals.* AIChE Journal, 1980. **26**(1): p. 16-23.

145.   Mirth, G., F. Eder, and J.A. Lercher, *Design and Application of a New Reactor for in-Situ Infrared Spectroscopic Investigations of Heterogeneously Catalyzed-Reactions.* Applied Spectroscopy, 1994. **48**(2): p. 194-197.

146.   Kokotailo, G.T., et al., *Structure of Synthetic Zeolite ZSM-5.* Nature, 1978. **272**(5652): p. 437-438.

147.   Jentys, A., H. Tanaka, and J.A. Lercher, *Surface processes during sorption of aromatic molecules on medium pore Zeolites.* Journal of Physical Chemistry B, 2005. **109**(6): p. 2254-2261.

148.   Auerbach, S.M., et al., *Transport-Theory for Cationic Zeolites - Diffusion of Benzene in Na-Y.* Journal of Physical Chemistry, 1995. **99**(26): p. 10600-10608.

149.   Clark, L.A., et al., *Diffusion mechanisms of normal alkanes in faujasite zeolites.* Journal of Chemical Physics, 1999. **111**(3): p. 1209-1222.

150.   Zheng, S., et al., *On the enhanced selectivity of HZSM-5 modified by chemical liquid deposition.* Topics in Catalysis, 2003. **22**(1-2): p. 101-106.

151.   Zheng, S.R., et al., *Novel model explaining toluene diffusion in HZSM-5 after surface modification.* Journal of Physical Chemistry B, 2004. **108**(4): p. 1337-1343.

152.   Brunauer, S., P. Emmett, and E. Teller, *Adsorption of Gases in Multimolecular Layers.* Journal of the American Chemical Society, 1938. **60**(2): p. 309-319.

153. Gregg, S.J., *Adsorption Surface Area and Porosity*. 2nd ed. 1982, New York: Academic Press.

154. Emeis, C.A., *Determination of Integrated Molar Extinction Coefficients for Infrared-Absorption Bands of Pyridine Adsorbed on Solid Acid Catalysts*. Journal of Catalysis, 1993. **141**(2): p. 347-354.

155. Jentys, A., H. Tanaka, and J.A. Lercher, *Mass transfer processes during sorption and diffusion of aromatic molecules on medium pore zeolites*. Studies of Surface Science and Catalysis, 2004. **154**: p. 2041-2048.

156. Trens, P., et al., *Study of n-hexane adsorption in MCM-41 mesoporous materials: a scaling effect approach of capillary condensation processes*. New Journal of Chemistry, 2004. **28**(7): p. 874-879.

157. Heink, W., et al., *Self-Diffusion Measurements of Normal-Alkanes in Zeolite NaCaA by Pulsed-Field Gradient Nuclear-Magnetic-Resonance*. Journal of the Chemical Society-Faraday Transactions, 1992. **88**(3): p. 515-519.

158. Jobic, H., *Diffusion of linear and branched alkanes in ZSM-5. A quasi-elastic neutron scattering study*. Journal of Molecular Catalysis A-Chemical, 2000. **158**(1): p. 135-142.

159. Moller, A., et al., *Uptake-curves for the determination of diffusion coefficients and sorption equilibria for n-alkanes on zeolites*. Microporous and Mesoporous Materials, 2009. **125**(1-2): p. 23-29.

160. Kolvenbach, R., et al., *Molecular understanding of sorption in hierarchical MFI*. Catalysis Letters, 2013. **143**: p. 1116-1122.

161. Mukti, R.R., A. Jentys, and J.A. Lercher, *Orientation of alkyl-substituted aromatic molecules during sorption in the pores of HZSM-5 zeolites*. Journal of Physical Chemistry C, 2007. **111**(10): p. 3973-3980.

162. Pitzer, K.S. and D.W. Scott, *The Thermodynamics and Molecular Structure of Benzene and Its Methyl Derivatives1*. Journal of the American Chemical Society, 1943. **65**(5): p. 803-829.

163. Yan, T.Y., *Separation of p-xylene and ethylbenzene from C8 aromatics using medium-pore zeolites*. Industrial & Engineering Chemistry Research, 1989. **28**(5): p. 572-576.

164.   Xomeritakis, G., Z.P. Lai, and M. Tsapatsis, *Separation of xylene isomer vapors with oriented MFI membranes made by seeded growth.* Industrial & Engineering Chemistry Research, 2001. **40**(2): p. 544-552.

165.   Xomeritakis, G., S. Nair, and M. Tsapatsis, *Transport properties of alumina-supported MFI membranes made by secondary (seeded) growth.* Microporous and Mesoporous Materials, 2000. **38**(1): p. 61-73.

166.   Xomeritakis, G. and M. Tsapatsis, *Permeation of aromatic isomer vapors through oriented MFI-type membranes made by secondary growth.* Chemistry of Materials, 1999. **11**(4): p. 875-+.

167.   Zheng, S.R., et al., *Influence of surface modification on the acid site distribution of HZSM-5.* Journal of Physical Chemistry B, 2002. **106**(37): p. 9552-9558.

168.   Kruk, M., M. Jaroniec, and J. Choma, *Comparative analysis of simple and advanced sorption methods for assessment of microporosity in activated carbons.* Carbon, 1998. **36**(10): p. 1447-1458.

169.   Song, L.J. and L.V.C. Rees, *Diffusion of propane in theta-1 and silicalite-1 zeolites.* Microporous and Mesoporous Materials, 2000. **41**(1-3): p. 193-200.

170.   Garcia, S.F. and P.B. Weisz, *Effective diffusivities in zeolites 1. Aromatics in ZSM-5 crystals.* Journal of Catalysis, 1990. **121**(2): p. 294-311.

171.   Weisz, P.B., *Molecular-diffusion in microporous materials - formalisms and mechanisms.* Industrial & Engineering Chemistry Research, 1995. **34**(8): p. 2692-2699.

172.   Rodrigues, A.E., et al., *Importance of intraparticle convection in the performance of chromatographic processes.* Journal of Chromatography, 1992. **590**(1): p. 93-100.

173.   Bakker, W.J.W., et al., *Permeation characteristics of a metal-supported silicalite-1 zeolite membrane.* Journal of Membrane Science, 1996. **117**(1-2): p. 57-78.

174.   van de Graaf, J.M., F. Kapteijn, and J.A. Moulijn, *Modeling permeation of binary mixtures through zeolite membranes.* AIChE Journal, 1999. **45**(3): p. 497-511.

175.   Kapteijn, F., J.M. van de Graaf, and J.A. Moulijn, *One-component permeation maximum: Diagnostic tool for silicalite-1 membranes?* AlChE Journal, 2000. **46**(5): p. 1096-1100.

176. Krishna, R., *A unified approach to the modelling of intraparticle diffusion in adsorption processes.* Gas Separation & Purification, 1993. **7**(2): p. 91-104.

177. Krishna, R. and J.M. van Baten, *Diffusion of alkane mixtures in zeolites: Validating the Maxwell-Stefan formulation using MD simulations.* Journal of Physical Chemistry B, 2005. **109**(13): p. 6386-6396.

178. Krishna, R. and J.M. van Baten, *Diffusion of alkane mixtures in MFI zeolite.* Microporous and Mesoporous Materials, 2008. **107**(3): p. 296-298.

179. Kapteijn, F., et al., *Temperature- and occupancy-dependent diffusion of n-butane through a silicalite-1 membrane.* Microporous Materials, 1994. **3**(3): p. 227-234.

List of Figures

List of Tables

Curriculum vitae

Date of birth: 27.10.1985
Place of birth   Bergisch-Gladbach, Germany

Professional Experience

Since 01/2014	**Alantum Europe GmbH** **Chemical Process Technology** Senior Research Scientist
05/2010 – 12/2013	**Chair of Chemical Engineering** **Technische Universität München** Ph.D. student Dissertation advisor: Prof. Dr. Johannes A. Lercher Topic of the Ph.D. thesis: "Transport in nano-sized, mesoscopically structured ZSM-5 zeolites"
03/2007 – 10/2009	**Chair of Chemical Engineering** **Technische Universität München** Student research assistant (20 h/week) Development and administration of an oracle based database

Education

10/2008 – 04/2010	**Technische Universität München** **Master of Science (Chemistry)** Major subject: chemical engineering Minor subject: catalysis and reaction technology Master thesis: "Diffusion and separation characteristics of binary hydrocarbon mixture in MFI", grade: 1.0 Overall grade: "Passed with high distinction" (1.1)
10/2005 – 09/2008	**Technische Universität München** **Bachelor of Science (Chemistry)** Bachelor thesis: "Synthesis of Rb_3PtF_7", grade: 1.3 Overall grade: "Passed with merit" (1.9)
10/2002 – 09/2003	**Ruhr-Universität Bochum** SchülerUni Bochum, inorganic chemistry, grade: 1.7
07/1996 – 07/2005	**Gymnasium am Ostring, Bochum** Abitur (equivalent to A level), overall grade: 1.2

Internships

03/2009 – 04/2009	**Shell Global Solutions, Amsterdam**

List of Publications

Journals

Kolvenbach, R., Al-Yassir, N., Al-Khattaf, S.S., Gobin, O.C., Ahn, J.H., Jentys, A., Lercher, J.A., *A comparative study of diffusion of benzene/p-xylene mixtures in MFI particles, pellets and grown membranes*, Catalysis Today 2011. **168**: p. 147-157

Kolvenbach, R., Gonzalez-Pena, L.F., Jentys, A., Lercher, J.A., *Molecular understanding of sorption in hierarchical zeolites with MFI structure,* Catalysis Letters 2013. **143**: p. 1116-1122

Kolvenbach, R., Gonzalez-Pena, L.F., Jentys, A., Lercher, J.A., *Diffusion of mixtures of light alkanes and benzene in nano-sized H-ZSM5,* Journal of Physical Chemistry C (submitted)

Kolvenbach, R., Kanervo, J., Ahn, J.H., Al-Khattaf, S.S., Neudeck, C., Jentys, A., Lercher, J.A., *Detailed evaluation of mesoscopic transport rates in hierarchical ZSM-5 by zero length column technique,* (in preparation)

Schüßler, F., Pidko, E.A., Kolvenbach, R., Sievers, C., Hensen, E.J.M., van Santen, R.A., Lercher, J.A., *Nature and Location of Cationic Lanthanum Species in High Alumina Containing Faujasite Type Zeolites*, Journal of Physical Chemistry C, 2011. **115**: p. 21763-21776

Ahn, J.H., Kolvenbach, R., Al-Khattaf, S.S., Jentys, A., Lercher, J.A., *Methanol usage in toluene methylation with medium and large pore zeolites,* ACS Catalysis, 2013. **3**: p. 817-825

Gutiérrez, O.Y., Yu, Y., Kolvenbach, R., Haller, G.L., Lercher, J.A., *Hydrogenation of tetralin over Pt catalysts supported on sulfated zirconia and amorphous silica alumina*, Catalyst Science & Technology, 2013. **3**: p. 2365-2372

Ahn, J.H., Kolvenbach, R., Al-Khattaf, S.S., Jentys, A., Lercher, J.A., *Enhancing shape selectivity without loss of activity – novel mesostructured ZSM5 catalysts for methylation of toluene to p-xylene*, ChemComm 2013. **49**: p. 10584-10586

Ahn, J.H., Kolvenbach, R., Neudeck, C., Al-Khattaf, S.S., Jentys, A. Lercher, J.A., *Tailoring mesoscopically structured H-ZSM5 zeolites for toluene methylation*, J. Catal., 2013. **311**: p. 271-280

Schallmoser, S., Ikuno, T., Wagenhofer, M.F., Kolvenbach, R., Sanchez-Sanchez, M., Lercher, J.A., *Impact of the local environment of BAS in ZSM-5 on the catalytic activity in n-pentane cracking*, (in preparation)

Orals

Kolvenbach, R., Al-Yassir, N., Al-Khattaf, S.S., Gobin, O.C., Ahn, J.H., Jentys, A., Lercher, J.A., *Transport and separation properties of binary aromatic hydrocarbon mixtures in MFI powder, pellets and membrane*, 5th FEZA Conference, Valencia, Spanien, 2011

Kolvenbach, R. Ahn, J.H., Jentys, A., Al-Khattaf, S.S., Neudeck, C., Lercher, J.A., *Diffusion in nano-sized, hierarchical ZSM5 zeolites*, 24. Deutsche Zeolithtagung, Magdeburg, 2012

Kolvenbach, R. Ahn, J.H., Jentys, A., Al-Khattaf, S.S., Neudeck, C., Lercher, J.A., *Toluene methylation in nano-sized, hierarchically structured ZSM5 zeolites*, 45. Jahrestagung Deutscher Katalytiker, Weimar, 2012

Kolvenbach, R. Ahn, J.H., Jentys, A., Al-Khattaf, S.S., Neudeck, C., Lercher, J.A., *Toluene methylation in hierarchical ZSM-5*, International Conference on Catalysis, München, 2012

Kolvenbach, R. Ahn, J.H., Jentys, A., Al-Khattaf, S.S., Neudeck, C., Lercher, J.A., *Acidic and diffusional properties of hierarchical H-ZSM5 and the application in toluene methylation*, 17th International Zeolite Conference, Moskau, Russland, 2013

Jentys, A., Kolvenbach, R, Gonzalez-Peňa, L.F., Lercher, J.A., *Monitoring surface concentrations during sorption of aromatic/aliphatic mixtures in mesoscale organized MFI*, 26. Deutsche Zeolithtagung, Magdeburg, 2014

Poster

Kolvenbach, R., Gobin, O.C., Reitmeier, S.J., Jentys, A., Lercher, J.A., *A new setup for ZLC and FR ZLC experiments*, 43. Jahrestagung Deutscher Katalytiker, Weimar, 2010

Kolvenbach, R., Al-Yassir, N., Al-Khattaf, S.S., Gobin, O.C., Ahn, J.H., Jentys, A., Lercher, J.A., *Diffusion of aromatic hydrocarbons in MFI samples of powdered, pellet and membrane form*, 23. Deutsche Zeolithtagung, Erlangen, 2011

Kolvenbach, R., Gobin, O.C., Ahn, J.H., Jentys, A., Lercher, J.A., *Diffusion and Adsorption Properties of Aromatics in MFI Extrudates*, 44. Jahrestagung Deutscher Katalytiker, Weimar, 2011

Kolvenbach, R., Gobin, O.C., Ahn, J.H., Jentys, A., Lercher, J.A., *Diffusion of benzene/p-xylene mixtures in MFI membranes*, 9th Symposium on the Characterization of Porous Solids, Dresden, 2011

Kolvenbach, R., Al-Nassir, N., Al-Khattaf, S.S., Gobin, O.C., Ahn, J.H., Jentys, A., Lercher, J.A., *Shape selective alkylation of toluene using novel hierarchically structured zeolites*, CRC/NU Workshop, München, 2011

Ahn, J.H., Kolvenbach, R., Al-Khattaf, S.S., Jentys, A., Lercher, J.A., *Kinetic consequences of hierarchical HZSM-5 in toluene methylation*, 45. Jahrestagung Deutscher Katalytiker, Weimar, 2012

Kolvenbach, R., J.H. Ahn, Gonzalez Pena, L.F., Reitmeier, S.J., Jentys, A., Lercher, J.A., *Diffusion of binary hydrocarbon mixtures in MFI monitored by time resolved in-situ IR spectroscopy*, 25. Deutsche Zeolithtagung, Hamburg, 2013

Ahn, J.H., Kolvenbach, R., Al-Khattaf, S.S., Jentys, A., Lercher, J.A., *Utilization of methanol in toluene methylation over acidic zeolites*, 25. Deutsche Zeolithtagung, Hamburg, 2013

Kolvenbach, R., Ahn, J.H., Gonzalez Pena, L.F., Jentys, A., Lercher, J.A., *Monitoring binary diffusion for the design of novel shape selective zeolites by fast time resolved IR spectroscopy*, 46. Jahrestagung Deutscher Katalytiker, Weimar, 2013

Jentys, A., Kolvenbach, R., Ahn, J.H., Gonzalez Pena, L.F., Lercher, J.A., *Sorption kinetics of aromatic/ aliphatic mixtures in mesoscale organized HZSM5 catalysts*, 47. Jahrestagung Deutscher Katalytiker, Weimar, 2014